Imaging crustal structures of orogenic belts using ambient noise tomography: implications for mountain building processes

By

Chengxin Jiang

A thesis submitted to Macquarie University
for the degree of Doctor of Philosophy
Department of Earth and Planetary Sciences

Australian Research Council Centre of Excellence for
Core to Crust Fluid Systems (CCFS) and GEMOC

June 2016

Typeset in LaTeX 2_ε.

Dedication

To my fiancé Song Lu, for her love and support. Also to my parents and Song's parents, to whom I am deeply indebted.

Acknowledgements

This thesis would not be possible without the help and advice of many people. Foremost, I want to thank my supervisor Yingjie Yang for his personal and professional guidance and supports along the way. I am really grateful to him for taking me, who was a structural geologist and had no background in geophysics, as his student. He guides me into the field of seismology by teaching me from scratch, and encourage me to combine my background with seismology to solve geological problems, which serves as the main motivation of this thesis. His criticism and persistence in science will inspire me in my future scientific career. I also thank Juan Carlos Afonso to be my co-supervisor. His keen scientific insight has been indispensable to me. Thanks also go to my co-authors Yong Zheng and Nick Rawlinson, and the three examiners of this thesis, Anya Reading, Huajian Yao and Fiona Darbyshire, for their contributions that have significantly improved the quality of this work. Special thanks to Christopher Grose, who sacrificed amounts of holiday time to help polish some of the chapters of this thesis. Thanks also go to Beñat Oliveira and Jun Xie for their help on the construction and formatting of this thesis.

I am grateful to Bill Griffin, for both of very helpful discussions on the geology of Tibetan Plateau and Newer Volcanics Province and detailed comments and reviews on the initial draft of some of the manuscripts and chapters of this thesis. I would also like to thank Sue O'Reilly and Steve Foley, who gave me great support and advices during my PhD within the Australian Research Council centre of GEMOC and CCFS. The other members in the geophysics group, Jun Xie, Zhen Guo, Mehdi Tork Qashqai, Kai Wang and Farshad Salajegheh, helped me significantly on the knowledge of geophysics. I have benefited from

discussions with Qing Xiong, Sandra Piazolo, Jianggu Lu, Siqi Zhang, Takako Satsukawa, Richard Flood, Nathan Daczko and many other PhD students and postdocs from the department.

I would also like to thank Mark Lackie, who provided me with valuable chances to work as tutors both for practises and field trips. I also thank Fenglin Niu, for his great help and guidance during my visit at Rice University. The encouragement and mentorship of Shaofeng Liu during my undergraduate and master studies will never be forgotten.

The valuable seismic data provides the basis for the studies of this thesis. I deeply thank the PIs and team members of the NETS and ASCENT experiments for collecting exceptionally valuable data in the NE Tibetan Plateau. I also thank the Data Management Centre of the China National Seismic Network at the Institute of geophysics, China Earthquake Administration for providing the data from the Chinese provincial networks. The facilities of the IRIS Data Management System are used to access parts of the data used in this study. The WOMBAT dataset has been taken from the seismic archive maintained at the Research School of Earth Sciences, Australian National University. We would like to extend our thanks to Greg Houseman and Stewart Greenhalgh from Monash and Flinders University respectively (at the time) for deploying the LF98 and make the data freely available, and also the members of RSES, ANU who have joined and helped the deployment of the extensive set of portable seismic recorders across the Australian continent. This work has been supported by an Australian Research Council Discovery Grant (DP120103673) and Future Fellowship (FT130101220) and also by a grant (SKLGED2015-4-2-EZ) from the State Key Laboratory of Geodesy and Earth's Dynamics, Institute of Geodesy and Geophysics, Chinese Academy of Sciences, and a Macquarie University doctoral scholarship.

List of Publications

- **Chapter 2.** Jiang, C. X., Yang, Y. J., & Zheng, Y. *Penetration of mid-crustal low velocity zone across the Kunlun Fault in the NE Tibetan Plateau revealed by ambient noise tomography.* Earth and Planetary Science Letters, 406, 81-92 (2014).

- **Chapter 3.** Jiang, C. X., Yang, Y. J., & Zheng, Y. *Crustal structure at the conjunction of Qinling Orogen, Yangtze Craton and Tibetan Plateau: implications for the formation of Dabashan Orocline and the growth of Tibetan Plateau.* Geophysical Journal International, 205, 1670-1681 (2016).

- **Chapter 4.** Jiang, C. X., Yang, Y. J., & Zheng, Y. *Complex layered deep-crustal deformation in the NE Tibetan Plateau and surrounding orogenic belts inferred from ambient noise.* (to be submitted)

- **Chapter 5.** Jiang, C. X., Yang, Y. J., & Rawlinson, N. *Crustal structure of the Newer Volcanics Province, SE Australia from ambient noise tomography.* (submitted)

Abstract

Orogenic belts are often characterized by strong crustal heterogeneity, which mainly results from complex tectonic evolutions. Conventional geological methods only sample the volumes near the surface, while seismic tomography enables a comprehensive and three-dimensional sampling of the physical properties of the Earth. The recent emergence of ambient noise tomography, in particular, allows us to study crustal heterogeneity with unprecedented resolution. In this thesis, I have adopted ambient noise tomography and Monte-Carlo inversion methods to construct models of crustal velocity in three orogenic belts, including the northeast Tibetan Plateau, the Qinling orogenic belt in central China, and the Delamerain orogen and its associated Newer Volcanics Province (NVP) in southeast Australia. The major deformation in these three orogenic belts occurred in Cenozoic, Mesozoic and early Paleozoic time respectively, and the relict orogenic structure is well preserved. The ambient noise tomography is subject to minor effects of off-great circle propagation and wavefront healing, and is therefore able to capture reliable velocity features in regional scales. Based on the highly resolved crustal-velocity models, some hotly-debated scientific questions are discussed, which include 1) how low-velocity zones in the mid/lower crust of the northeast Tibetan Plateau are distributed, and how they are related to the growth of the Tibetan Plateau; 2) whether there is seismic evidence for the indentation model on the formation of the Dabashan Orocline, and how the extrusion of the Tibetan Plateau affects deformation in the west Qinling Orogen; 3) what is the crustal tectonic setting of the NVP, and how the magmas of the NVP were stored and migrated through the crust. In addition, I also investigate the azimuthal anisotropy in the Qinling and its neighboring area to complement

my derived isotropic velocity model in the region.

We integrate velocity models with interpretations from other geological, geochemical and geophysical studies in order to solve the above geological questions, and their answers contribute to a better understanding of the mountain building processes in these orogenic belts.

Declaration

I certify that the work in this thesis entitled "**Imaging crustal structures of orogenic belts using ambient noise tomography: implications for mountain building processes**"has not previously been submitted for a degree, nor has it been submitted as partial requirement for a degree to any other university or institution other than Macquarie University.

I also verify that this thesis is an original piece of research and has been written by me. Any help and assistance that I have received in my research work and the preparation of the thesis itself have been properly acknowledged.

In addition, I certify that all data, information sources and literature used are indicated in the thesis.

Chengxin Jiang

Student ID: 42942217

June 20, 2016

Contents

List of Figures

1

Introduction

1.1 Motivation

Although the continental crust accounts for less than 1% of the Earth by weight, it contains considerable information about the Earth's tectonic evolution. In particular, an orogenic belt is one type of geological features formed in the course of active tectonic processes, typically involving a variety of mantle dynamics and geological processes, such as plate subduction, continent-continent collision and sequences of metamorphism and magmatism. These processes cause significant modifications of the crust, creating extensive heterogeneity in terms of both structure and composition. Comprehensive knowledge of the crustal heterogeneity strongly constrains our understanding of mountain building processes, and hence the tectonic evolution of the crust.

Seismic method is the main technique employed to image the subsurface structure of the

Earth. In particular, the advent of ambient noise tomography (ANT) in the past decade has enabled seismologists to image crustal structures with unprecedented resolutions. This mainly results from the fact that short-period surface wave signals (< 25 s) can be successfully extracted from cross-correlations of seismic ambient noise, and these short-period surface waves are mainly sensitive to crustal structures. Meanwhile, the recent emergence of continental-scale seismic arrays has significantly improved the path coverage of seismic rays for tomography; thereby significantly increasing the lateral resolution of ANT. Prominent examples of such seismic arrays include the USArray in the U.S.A, the CEArray in China and the WOMBAT array in southeast Australia.

With the combination of both theoretical advancements and data availability, ANT is able to image very fine structures in the crust. Compared to the spatially limited samples from conventional geological methods, a three-dimensional crustal velocity model from ANT provides comprehensive constraints on the current physical and chemical properties of the crust, and these properties hold important clues to the past tectonics. When combined with geological and geochemical signatures, such as the time of deformation, structural patterns and petrological character, a velocity model can serve as a principal source of information from which regional tectonic evolution can be unraveled. This serves as the fundamental motivation of this thesis.

In this thesis, by undertaking four case studies in three orogenic belts of tectonic significance, which include the northeastern part of the Tibetan Plateau, the Qinling Orogen and its adjacent regions, and the Delamerian orogen and the associated Newer Volcanics Province, I will demonstrate that detailed crustal structures imaged by ANT greatly contribute to our understanding of the specific tectonic processes responsible for shaping the geological features in our chosen study regions, where the formation ages range from the Cenozoic to the early Paleozoic.

1.2 Ambient noise surface wave tomography

Prior to the advent of ANT, the most widely used surface wave tomography method was based on surface waves emitted by earthquakes. However, due to the strong scattering and

attenuation effects of surface waves in relatively heterogeneous media, it is difficult to obtain short-period surface waves (< 25 s, periods most sensitive to crustal structures) from distant earthquakes. Consequently, it is extremely difficult to image fine-scale crustal structures using traditional earthquake-based surface wave tomography. In contrast to earthquake-based tomography methods, ANT uses diffuse background noise, which is generated from the interactions between ocean waves and the shorelines [Traer & Gerstoft (2014); Traer *et al.* (2012)]. Empirical Green's functions of surface waves between a pair of stations can be extracted by cross-correlating continuous time series of such ambient noise. Within a regional seismic array, all inter-station measurements of surface wave dispersion including the part sensitive to the crust can be made. Using the obtained inter-station dispersion measurements, tomography can be performed to image the underlying structures.

Reliance on diffuse background noise provides ANT distinct advantages over the traditional surface wave tomography: 1) surface wave extracted from ambient noise cross-correlations have known source term if the distribution of ambient noise is homogenous [Snieder (2004);Lin *et al.* (2008)]. 2) Ray path densities in ANT are controlled by the configuration of a seismic array. Thus, by deploying a dense seismic array, high density ray path coverage can be achieved. In contrast, most earthquakes occur at plate boundaries, leading to an uneven distribution of ray paths in earthquake-based surface wave tomography. 3) The dominant sources of ambient noise originate from oceans, making the method much more economical (and thus "greener") than traditional seismic imaging techniques based on active sources. Moreover, the successful application of this method on industry-interested scales [Gouedard *et al.* (2012); Lin *et al.* (2013); Young *et al.* (2013b)] has demonstrated that ANT may serve as a promising tool for exploration seismology in the future.

The development of ANT is built upon a solid theoretical foundation. Though the initial idea behind this technique has its roots back to 1905 [Einstein (1905)], the pioneer work about ANT in seismology may go to Aki's work in 1957 about the SPAC method [(Aki, 1957)]. And the recent developments of ANT are mostly based on the work in acoustics [Lobkis & Weaver (2001)] and ultrasonics [Weaver & Lobkis (2001)]. Early theoretical studies demonstrated that the cross-correlation of wavefields recorded at two receivers can recover the full Green's functions under the condition that either the noise sources are homogenously distributed or

if wavefields can be considered diffusive [Lobkis & Weaver (2001); Roux *et al.* (2005); Sabra *et al.* (2005a); Snieder (2004)]. Because the distribution of seismic noise sources in the real world is known to often be inhomogeneous, consequent biases in the recovery of the Green's functions has been a cause for worry in its application to the Earth [Harmon *et al.* (2010); Sabra *et al.* (2005b)].

However, subsequent studies have demonstrated that the Green's functions from ambient noise are in fact different from the full Green's functions [Ritzwoller (2008)]. The cross-correlations from ambient noise are thus referred to as Empirical Green's functions (EGFs). A series of following studies confirmed that the inferred EGFs from seismic noise can generate accurate dispersion measurements [Harmon *et al.* (2008); Shapiro & Campillo (2004)], and surface wave dispersion maps generated by ANT with slightly inhomogeneous noise sources are very similar to those from earthquake tomography [Yang & Ritzwoller (2008); Yang *et al.* (2007); Yao *et al.* (2006)]. Therefore, ANT has been verified to be valid and reliable for tomography, even though the sources of ambient noise may be not perfectly homogenously distributed. Since then, this technique has been extensively employed to image the structures of the crust and the uppermost mantle at regions all over the world, both on regional scales [e.g., Chen *et al.* (2014); Ekstrom *et al.* (2009); Fang *et al.* (2015); Gao *et al.* (2011); Huang *et al.* (2015); Jaxybulatov *et al.* (2014); Karplus *et al.* (2013); Liang & Langston (2008); Lin *et al.* (2007); Ma & Clayton (2015); Moschetti *et al.* (2010); Nishida *et al.* (2008); Pawlak *et al.* (2012); Ren *et al.* (2013); Stehly *et al.* (2009); Villasenor *et al.* (2007); Ward (2015); Ward *et al.* (2013); Yang *et al.* (2011); Yang *et al.* (2008); Yao *et al.* (2006); Yao *et al.* (2008)] and continental scales [e.g., Bensen *et al.* (2008); Kao *et al.* (2013); Saygin & Kennett (2010); Saygin & Kennett (2012); Yang *et al.* (2007); Zheng *et al.* (2008)]. Currently, ANT has become a routine method for the imaging of crustal and uppermost mantle structures.

In particular, numerous applications of ANT have been carried out in China and Australia. In China, the deployment of a new digital seismic observing system [Zheng *et al.* (2009)], termed CEArray, has sparked a significant number of studies attempting to shed light on the nature of the crust and upper mantle beneath southeast Asia [Bao *et al.* (2015); Bao *et al.* (2013); Chen *et al.* (2014); Chen *et al.* (2015); Deng *et al.* (2015); Guo *et al.*

(2015); Guo *et al.* (2016); Guo *et al.* (2009); Huang *et al.* (2010); Li *et al.* (2014); Li *et al.* (2009); Luo *et al.* (2012); Liu *et al.* (2014); Tang *et al.* (2013); Jiang *et al.* (2014); Xie *et al.* (2013); Yang *et al.* (2012); Yang *et al.* (2010); Yao *et al.* (2010); Zheng *et al.* (2011); Zhou *et al.* (2012)]. In Australia, the deployment of the largest transportable array in the southern hemisphere, the WOMBAT array [Rawlinson & Kennett (2008); Rawlinson *et al.* (2006a); Rawlinson *et al.* (2006b); Rawlinson *et al.* (2014b)] has also led to a number of ambient noise tomography studies in the southeast part of the continent [Arroucau *et al.* (2010); Pilia *et al.* (2015a); Rawlinson *et al.* (2014a); Young *et al.* (2013b); Young *et al.* (2011); Young *et al.* (2013b)].

1.3 Automated frequency-time analysis method

Before performing tomography inversion, one important procedure of the ambient noise data pre-processing is the measurement of inter-station phase velocities. Throughout this thesis, we obtain the phase velocity dispersion curves using an automated frequency-time analysis (FTAN) method, which is briefly described as below. More details about this method can be found in Bensen et al. (2007) and Lin et al. (2008).

Firstly, a series of Gaussian bandpass filters are applied to the cross-correlation waveforms. The filtered waveforms $f(t)$ and its Hilbert transform $F_H(t)$ are combined to construct an analytic signal $f(t) + iF_H(t)$, from which the envelope function $A(t)$ and phase function $\phi(t)$ are obtained. The group arrival time t_{max} is directly measured from the peak of the envelope function, so that the group velocity can be easily derived from the ratio of Δ/t_{max}, where Δ is the inter-station distance. Note that the instantaneous frequency at t_{max} is determined from $\omega = [\frac{\partial\phi(t)}{\partial t}]_{t=t_{max}}$, which may deviate from the centre frequency of the Gaussian filter. This correction of replacing centre frequency of the Gaussian filter with the instantaneous frequency is suggested to be of great importance when the spectrum of the waveform is not flat [Bensen *et al.* (2007)].

For an instantaneous frequency ω, the phase of the estimated Green's function observed

at time t can be calculated from the following expression:

$$\phi(t) = k\Delta - \omega t + \frac{\pi}{2} - \frac{\pi}{4} + N * 2\pi + \lambda \qquad N \in Integer \tag{1.1}$$

where k is the wavenumber, Δ is the inter-station distance, $\frac{\pi}{2}$ represents the phase shift caused by the negative time-derivative, $-\frac{\pi}{4}$ the is the phase shift assuming ambient noise sources are homogeneously distributed, and $N * 2\pi$ is the intrinsic phase ambiguity of phase measurements. Theoretical studies predict that the term of "initial phase" λ should equal to zero when the distribution of the ambient noise source is relatively homogeneous [Roux *et al.* (2005); Snieder (2004)]. Lin *et al.* (2008) used a three-station method to calculate the "initial phase" of λ and found that the term approximately equals to zero even under the condition of an inhomogeneous source distribution. Finally, by substituting the expression of $c = \omega/k$ into equation 1.1, the phase velocity c can be written:

$$c = \frac{\Delta\omega}{\phi(t_{max}) + \omega t_{max} - \frac{\pi}{4} - N * 2\pi} \tag{1.2}$$

In this equation, N is still unknown, and is therefore required in order to obtain an unambiguous measurement of the phase velocity. In the case studies of this thesis, I use predicted inter-station dispersion curves from available 3D models in the study region as references to solve N, which is well determined at most of the occasions.

1.4 Estimates of tomography uncertainties

Tomography uncertainties not only provide criteria to evaluate model reliabilities, but also are used to determine which model is accepted or rejected during the probabilistic 3D model inversions. Therefore, they are of particular importance for tomographic studies.

Some tomography methods, such as the eikonal tomography of Lin *et al.* (2009) and the trans-dimensional tomography method of Bodin *et al.* (2012), can produce model uncertainties. However, these methods have special requirements on seismic data. For example, eikonal tomography [Lin *et al.* (2009)] requires nearly regular and homogenous seismic arrays, such as the USArray, for optimal estimates of both phase velocities and their associated uncertainties. In addition, one usually needs to include many more stations located outside

of the study region in order to achieve measurements for the entire study region, especially around the edges. For example, I incorporate a total of 736 stations in Chapter 4 to image the anisotropic distributions in the NE Tibetan Plateau and the adjacent areas. This number is nearly as twice as that of the total stations located in the research area.

Compared to eikonal tomography [Lin *et al.* (2009)], other tomography methods, such as the ray-theory based tomography method of Barmin *et al.* (2001) that are employed in the case studies of Chapter 2 and 3, do not require homogenous distribution of seismic array in order to achieve optimal estimates. However, these methods do not provide estimations of model uncertainties. To overcome this shortcoming, I run eikonal tomography in the area of dense and regular station coverage. Then, I calculate the average of these phase velocity uncertainties obtained from eikonal tomography and use the average as the typical phase velocity uncertainties for the whole study region. I applied this strategy for the case studies in Chapter 2 and 3.

Another approach to deal with the unavailability of tomography uncertainties is to extract uncertainty information from tomography models with such estimates. For example, a previous study [Pilia *et al.* (2015a)] has applied trans-dimensional tomography method [Bodin *et al.* (2012)] to the entire WOMBAT data set to estimate both phase velocities and their associated uncertainties in the SE Australia. The data I used in Chapter 5 is one component of the WOMBAT data set that only covers the Newer Volcanics Province, so I used the model uncertainties estimated by Pilia *et al.* (2015a) to approximate our tomography uncertainties in order to construct the 3D velocity model in the region.

1.5 Monte-Carlo inversion method

Throughout this thesis, we employ the Bayesian Monte Carlo inversion method developed by Shen *et al.* (2013) to invert local dispersion measurements from ambient noise tomography for depth-dependent shear-wave velocity models. The fundamentals of the Monte-Carlo inversion approach are based on the Bayesian theorem [Mosegaard & Sambridge (2002); Mosegaard & Tarantola (1995); Tarantola (2004)], which has been widely applied to the inversion of seismic observations, such as receiver functions [Agostinetti & Malinverno (2010);

Bannister *et al.* (2003); Clitheroe *et al.* (2000); Levin & Park (1997); Lucente *et al.* (2005); Nicholson *et al.* (2005); Sambridge (1999); Vinnik *et al.* (2004)], surface wave dispersion curves [Khan *et al.* (2011); Maraschini & Foti (2010); Shapiro & Ritzwoller (2002); Socco & Boiero (2008); Yao *et al.* (2008); Yoshizawa & Kennett (2002)] and the joint inversion of these two data sets [An & Assumpcao (2004); Bodin *et al.* (2012); Moorkamp *et al.* (2010); Liu *et al.* (2014); Shen *et al.* (2013); Tokam *et al.* (2010)]. In the context of statistics, the solution to the inverse problem is generally approximated by an *a posteriori* probability density of an ensemble of models. In the Bayesian theorem, *a posteriori* probability density can be quantified by combining prior information on the model m with the likelihood function of the observed data d on this model m according to the following expression (for the full version of Bayes theory, the reader is referred to the book of Sivia (1996)):

$$p(m|d_{obs}) \propto p(m) \times p(d_{obs}|m) \tag{1.3}$$

In the above expression, $p(m|d_{obs})$ is the *a posteriori* probability density of the unknown model parameter m based on the observed data d_{obs}. *p(m)* represents the *a priori* probability density of the model m based on our knowledge of it, provided it can be defined as a probability distribution. The likelihood function, denoted by $p(d_{obs}|m)$, is the reproducing probability of d_{obs} given a particular model m. In this thesis, the likelihood function is further related to the observed data through the misfit function *S(m)* as follows:

$$L(m) = exp(-\frac{1}{2} * S(m)) \tag{1.4}$$

where

$$S(m) = (g(m) - d_{obs})^T C_e^{-1}[g(m) - d_{obs}] \tag{1.5}$$

In expression 1.5, d_{obs} is a vector of empirical measurements (data), *g(m)* is the vector of predictions from model m, C_e^{-1} is the data covariance matrix, and T represents the transpose of a vector.

A key fact from the expression 1.3 is that, apart from a dependence on the observed data, any scientific inferences based on the posterior distribution also depends on the included prior information, which in our case corresponds to what we presume to already know about the

velocity structures of the sampled area. During the inversion of each case study in this thesis, we attempt to impose large uncertainties on prior information, both in the processes of model parameterisation and model selections, in order to reduce its influence on the inverted results. The prior information, however, is dependent on our particular interests, hence it may vary in different case studies. For the acceptance of a model inversion, we follow the Metropolis algorithm, which is executed as follows. Suppose there are two models of m_i and m_j, which are subsequently constructed and both fit the prior information, their likelihood functions are computed and represented as L_i and L_j respectively. The Metropolis algorithm rejects or accepts the model m_i based on the value of L_i/L_j. If this ratio is larger than 1 ($L_i/L_j > 1$), the model of m_i will be accepted. Otherwise, a random number is generated to compare with this ratio. If this random number is smaller than the ratio of L_i/L_j, model m_i will still be accepted. Otherwise model m_i is rejected. This probabilistic acceptance of a slightly poorer fitting model ensures that final posterior solutions are not trapped by local minima.

Compared with the traditional method of linearised least-squares inversion, the technique of non-linear Monte-Carlo inversion provides 1) the ability to reliably recover detailed information about the target region [Shen (2014)], and 2) a quantitative analysis of the uncertainties in the resulting models [Afonso *et al.* (2013a); Afonso *et al.* (2013b); Shen (2014); Bodin *et al.* (2012)]. The first advantage reflects the fact that the Earth is a highly non-linear system as many of the physical properties of the Earth do not have linear relations with their geophysical measurements. For example, as demonstrated in the study of Shen (2014), traditional linear inversions can result in unreliable models due to a) the thin-layer model parameterisation, b) the smoothing constraint that is usually *ad-hoc* and c) the attempt to fit every wiggle in the receiver functions. Meanwhile, the uncertainties of Earth models resulting from Monte-Carlo inversion provide criteria from which to evaluate the reliability of models for model-builders as well as for model-users. Such a feature is well illustrated in our case study imaging the crust of the NE Tibetan Plateau (Chapter 2), in which the existence and distribution of the regions having low velocity zones (LVZs) are statistically analysed based on the probability density.

In this thesis, the ANT method and the emergence of high-density seismic arrays both in China and Australia provide us an exceptional opportunity to construct high-resolution

crustal velocity models in the three selected orogenic belts.

1.6 Thesis objectives

The main objective of this thesis is to apply the method of ambient noise tomography and the Monte-Carlo inversion method to construct crustal models at three orogenic belts in order to understand their associated orogenic processes. We also investigate azimuthal anisotropic features at the same region as that in Chapter 3, as a complement to the isotropic velocity model. Specifically, the objectives of this thesis include:

1. Construction of a 3-D crustal isotropic Vs model in the NE Tibetan Plateau region in order to explore the detailed distribution of the crustal low velocity zones (LVZs), which improves the understanding of the deformation mechanism in the NE Tibetan Plateau.

2. Construction of a 3-D crustal isotropic Vs model in the conjunction of the NE Tibetan Plateau, Qinling Orogen and the Yangtze Craton in order to investigate the structural, compositional and possible rheological differences between different blocks. Such delineations help to a) verify the indentation model for the formation of the Dabashan Orocline and b) understand the impacts of the Tibetan Plateau's growth for the deformation of the west Qinling Orogen.

3. Investigation of azimuthal anisotropic features in the crust beneath the conjunction of the NE Tibetan Plateau, the Qinling Orogen and the Yangtze Craton in order to better understand a) the formation mechanism of the Qinling and Longmenshan orogens and b) the deformation mechanisms active in the NE Tibetan Plateau.

4. Construction of a 3-D crustal isotropic Vs model in the Newer Volcanics Province of southeast Australia in order to investigate the crustal magmatic plumbing system beneath this intra-plate volcanic setting and the crustal reflection of the distinct lithospheric units of the Delamerian and Lachlan orogens.

1.7 Thesis structure

This thesis is composed of six chapters, including a comprehensive introduction chapter (this chapter), four main chapters that are corresponding to the four case studies, and a final concluding chapter.

In Chapter 1 (this chapter), we present the motivations, the background of the several methods used in this thesis, including ambient noise tomography, automated frequency-time analysis (FTAN) method, and Monte-Carlo inversion, as well as the objectives of the thesis. A short summary for each of the four main chapters is given as follows.

In Chapter 2 (published in Earth and Planetary Science Letters as Jiang et al., 2014), we conduct surface wave tomography in the northeast Tibetan Plateau using seismic ambient noise records from several seismic arrays, including the Northeast Tibet Seismic Experiment (NETS), a Seismic Collaborative Experiment in Northeastern Tibet (ASCENT) and Chinese provincial networks (CEArray). Rayleigh wave phase velocity maps are generated at 10-60 s periods, based on which a 3-D isotropic Vsv model is constructed via a non-linear Monte-Carlo approach. We examine the statistical probabilities of the existences and distributions of mid/lower crustal low velocity zones (LVZs) in the NE Tibetan Plateau, and discuss their possible origins and implications for the growth mechanism of the Tibetan Plateau.

In Chapter 3 (published in Geophysical Journal International as Jiang et al., 2016), we conduct surface wave tomography in the conjunction area between the northeast Tibetan Plateau, the Qinling Orogen and the north Yangtze Craton, as a further extension of the study in Chapter 2. We use seismic ambient noise data from the same networks as that used in Chapter 2, but cover the regions more to the east. Based on the velocity model, we first investigate the correlations of the velocity anomalies with the local geology. Then, we assemble the available receiver functions in the research area, which are then combined with our velocity model and other geological and geochemical evidence to infer the compositional and possible rheological differences in the region. Finally, we discuss the effects of the extrusion of the Tibetan Plateau on the deformation of the west Qinling Orogen, and the mechanisms for the formation of the Dabashan Orocline based on the interpreted compositional and rheological properties in the region.

In Chapter 4 (in preparation for journal submission), we investigate the azimuthal anisotropy in the same region as in Chapter 3. We incorporate a total of 736 stations in and around the region in order to provide both good coverage of path densities and azimuthal distributions. The eikonal tomography of Lin *et al.* (2009) is adopted to derive the azimuthal anisotropic features at the period range of 10-40 s. Based on our derived azimuthal anisotropy and the geological evidence from previous studies in the region, we discuss the deformation mechanisms for the Qinling and Longmenshan orogens and the NE Tibetan Plateau.

In Chapter 5 (submitted), we employ the eikonal tomography of Rawlinson & Sambridge (2003), and ambient noise from the WOMBAT data set to image the crustal structures in the regions of the NVP and the orogenic belt between the Delamerian and Lachlan orogens in the western Victoria, southeast Australia. We adopt an improved stacking procedure during the ambient noise processing to increase the signal-to-noise ratio (SNR) of the cross-correlations in order to extract high quality dispersion curves for 2-18 s periods. Phase velocity maps are then constructed based on the inter-station dispersion curves, and are inverted for an isotropic 3D Vs model from the surface down to the depth of 30 km. By integrating the velocity model with inverted magnetotelluric model, geochemical signatures and lithospheric structures from previous studies, we discuss the crustal magmatic plumbing systems and possible fluid pathways beneath the intra-plate NVP, and examine a tectonic scenario characterizing the early Paleozoic Delamerian orogeny.

Chapter 6 is the conclusion chapter, in which we summarise the main implications of our models on the regional tectonic evolutions of our three study regions, and stress the capability of the crustal velocity model from ambient noise tomography in studying regional-scale geological problems. Future research directions based on the limitations of the current study are also addressed.

2

Penetration of mid-crustal low velocity zone across the Kunlun Fault in the NE Tibetan Plateau revealed by ambient noise tomography

2.1 Abstract

The NE Tibetan Plateau, composed of the Mesozoic accretions of Lhasa, Qiangtang and Songpan-Ganze Terranes, are bounded by the east Kunlun-Qaidam Block in the north with the boundary delineated by the Kunlun Fault. The NE Tibetan Plateau is at a nascent stage of plateau growth resulting from the collision between the Indian and Eurasian plates starting ∼50 million years ago, and is one of the best areas to study the growth mechanism of the Tibetan Plateau. In this study, we process continuous ambient noise data collected

from ∼280 stations between 2007 and 2010 and generate Rayleigh wave phase velocity maps at 10-60 s periods with a lateral resolution of ∼30-50 km for most of the study region. By adopting a Bayesian Monte Carlo method, we then construct a 3-D Vsv model of the crust using the Rayleigh wave dispersion maps. Our 3-D model reveals that strong LVZs exist in the middle crust across the NE Tibetan Plateau; and the lateral distribution of LVZs exhibits significant west-east variations along the Kunlun Fault. In the west of $98\,^{\circ}E$, LVZs are confined to regions of the Kunlun Fault and the eastern Kunlun Ranges, but absent beneath the Qaidam Basin; while in the east of $98\,^{\circ}E$, LVZs extend and penetrate northward into the east Kunlun and Qinling Orogens over ∼100 km across the Kunlun Fault. The strong contrast of the LVZ distribution along the Kunlun Fault may be related to the distinct neighboring tectonic units in the north: a strong crust of the Qaidam Basin in the west blocking the penetration of LVZs, but a weak crust in the Qinling Orogen facilitating the extrusion of LVZs. The distribution of LVZs in the NE Tibetan Plateau is consistent with the crustal channel flow model, which predicts a branch of north-eastward mid-crustal channel flow. Our 3D model clearly delineates the north extent of the mid-crustal LVZs, probably reflecting the status of channel flow in the NE Tibetan Plateau.

2.2 Introduction

The Tibetan Plateau is the highest and largest plateau in the world with an average elevation of ∼4-5 km and a double thickness continental crust. It stretches approximately 1000 km from north to south and 2500 km from east to west. In the first order, the growth of the Tibetan Plateau is caused by the Indian-Eurasian continental collision, which is generally believed to initiate ∼50 Ma ago when the Indian continental lithosphere encountered southern Tibet [Yin & Harrison (2000)]. However, how such a broad and highly elevated plateau formed and persisted is still not completely understood. Various hypotheses and models have been proposed to explain the growth and uplift of the Tibetan Plateau, such as the underplating/under-thrusting of the Indian plate beneath the Eurasian crust [Owens & Zandt (1997)], uniform crustal shortening and thickening [England & Houseman (1986)], eastward mass extrusion [Avouac & Tapponnier (1993); Tapponnier *et al.* (2001)] and mid/lower

crustal channel flow [Beaumont *et al.* (2006); Clark & Royden (2000); England & Molnar (1997); Royden *et al.* (1997)].

In the past few decades, numerous research efforts have been devoted to studying the nature of deformation and growth of the plateau, and especially, a large number of geophysical explorations have been carried out. However, due to the complexity of deformation history, the limitation of resolution in geophysical imagery and the lack of complete data sets, geoscientists still have not reached a consensus about the deformation and growth model of the Tibetan Plateau. More recently, a growing number of lines of evidence suggest that the mid/lower crust of the Tibetan Plateau is warm, ductile, and probably partially melted. These include: low velocity zones (LVZs) in the middle/lower crust from seismic tomography [Li *et al.* (2009); Yang *et al.* (2012); Yang *et al.* (2010); Yao *et al.* (2008); Yao *et al.* (2010)], high conductivity in the crust from magnetotelluric sounding [Bai *et al.* (2010); Le Pape *et al.* (2012); Unsworth *et al.* (2004); Wei *et al.* (2001)], warm crust from thermal and density modelling [Jimenez-Munt *et al.* (2008)] and shallow Curie isotherms [Alsdorf & Nelson (1999)], mid/lower crust originated volcanic rocks [Wang *et al.* (2012)] and extensive volcanism since the Cenozoic [Chung *et al.* (2005); Ding *et al.* (2007)]. These findings appear to meet the requirements of a crustal flow model which postulates a ductile and low-viscosity mid/lower crust is present in the Tibetan Plateau. According to the numerical modelling of the crustal flow model [Clark & Royden (2000)], a crustal weak layer tends to flow outward from the plateau interior following two branches: one branch flows south-eastward to the Yunnan region and the other flows north-eastward to the Qinling and Qilian Orogens, under the northward pushing by the Indian plate and the blocking by the Sichuan Basin in the east and the Qaidam Basin in the north. However, the mode and status of flow are still not fully understood; especially, to what extent the flows reach beyond the boundaries of the plateau is still not well delineated.

In the southeast margin of the Tibetan Plateau, a number of seismic studies observe widespread low seismic velocity layers in the mid/lower crust [Xu *et al.* (2007); Yao *et al.* (2008); Yao *et al.* (2010)], and magnetotelluric studies reveal mid-crustal highly-conductive layers [Bai *et al.* (2010)]. The observed low velocity and highly-conductive layers in the mid/lower crust are commonly interpreted as the presence of fluid or partial melt, which in

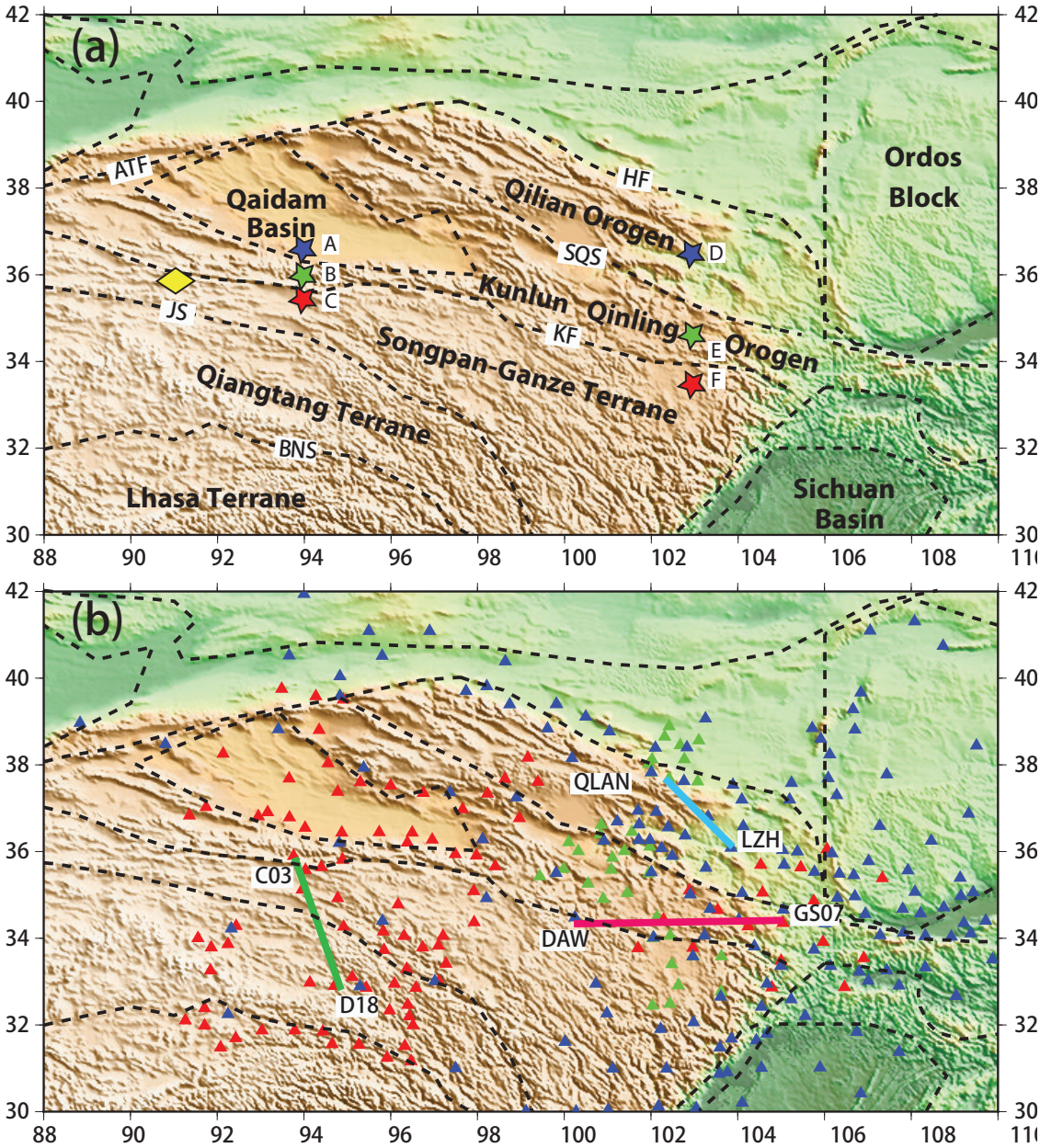

Figure 2.1: (a) Tectonic and geological units in the NE Tibetan Plateau and surrounding regions. The six stars denote the locations referred to in Figs. 2.6 and 2.8. The diamond denotes the location of rhyolitic samples generated by dehydration melting of crustal metasedimentary rocks [Wang *et al.* (2012)]. HF-Haiyuan Fault; ATF-Altyn Tagh Fault; SQS-South Qilian Suture; KF-Kunlun Fault; JS-Jingsha Suture; BNS-Bangong-Nujiang Suture. (b) Seismic stations of three different networks used in this study. Green: Northeast Tibet Seismic Experiment (NETS); Red: A Seismic Collaborative Experiment in Northeastern Tibet (ASCENT); Blue: Chinese provincial networks. The three coloured lines represent the station pairs referred to in Fig. 2.2.

turn makes the mid/lower crust weak and ductile, consistent with the crustal channel flow model even though the details of flow pattern could be complicated [Yao *et al.* (2008)].

In this study, we are focusing on the NE margin of the Tibetan Plateau (Figure 2.1a) where another branch of crustal channel flow is predicted by the crustal channel flow model [Clark & Royden (2000); Searle *et al.* (2011)], and broad low velocity zones in the mid crust are revealed by large-scale ambient noise tomography [Yang *et al.* (2012)] and a highly-conductive mid-crustal layer is also observed along a magnetotelluric profile [Le Pape *et al.* (2012)]. However, due to the resolution limitations of previous tomography studies, the detailed distribution of LVZs in the NE Tibetan Plateau is not completely constrained and discussed. Especially, if LVZs are confined to the Songpan-Ganze Terrane or have penetrated through the Kunlun Fault is still not completely addressed. By collecting the seismic noise data from ∼280 stations in the NE Tibetan Plateau and its surrounding regions and using the ambient noise tomography method, we construct a high-resolution 3D crustal Vsv model with a lateral resolution of ∼30-50 km.

2.3 Data and methods

Data used in this study are vertical components of continuous seismic data recorded at ∼280 stations from several seismic arrays (Figure 2.1b), including the Northeast Tibet Seismic Experiment (NETS), a Seismic Collaborative Experiment in North-eastern Tibet (ASCENT) and Chinese provincial networks [Zheng *et al.* (2009)] operating between 2007 and 2010. Using only vertical component data means surface waves extracted from noise are Rayleigh waves. Previous studies [Li *et al.* (2014); Yang *et al.* (2012); Yang *et al.* (2010)] have described these datasets in detail, so we do not elaborate here.

The procedures of data processing are the same as those adopted in our previous studies [Yang *et al.* (2012); Yang *et al.* (2010)] following Bensen *et al.* (2007). After symmetric components are formed by stacking positive and negative components of stacked cross-correlations, the method of automated frequency-time analysis (FTAN) [Dziewonski *et al.* (1969); Levshin & Ritzwoller (2001)] is adopted to measure Rayleigh wave phase velocity dispersion curves at 10-60 s periods. Three examples of inter-station cross-correlations and

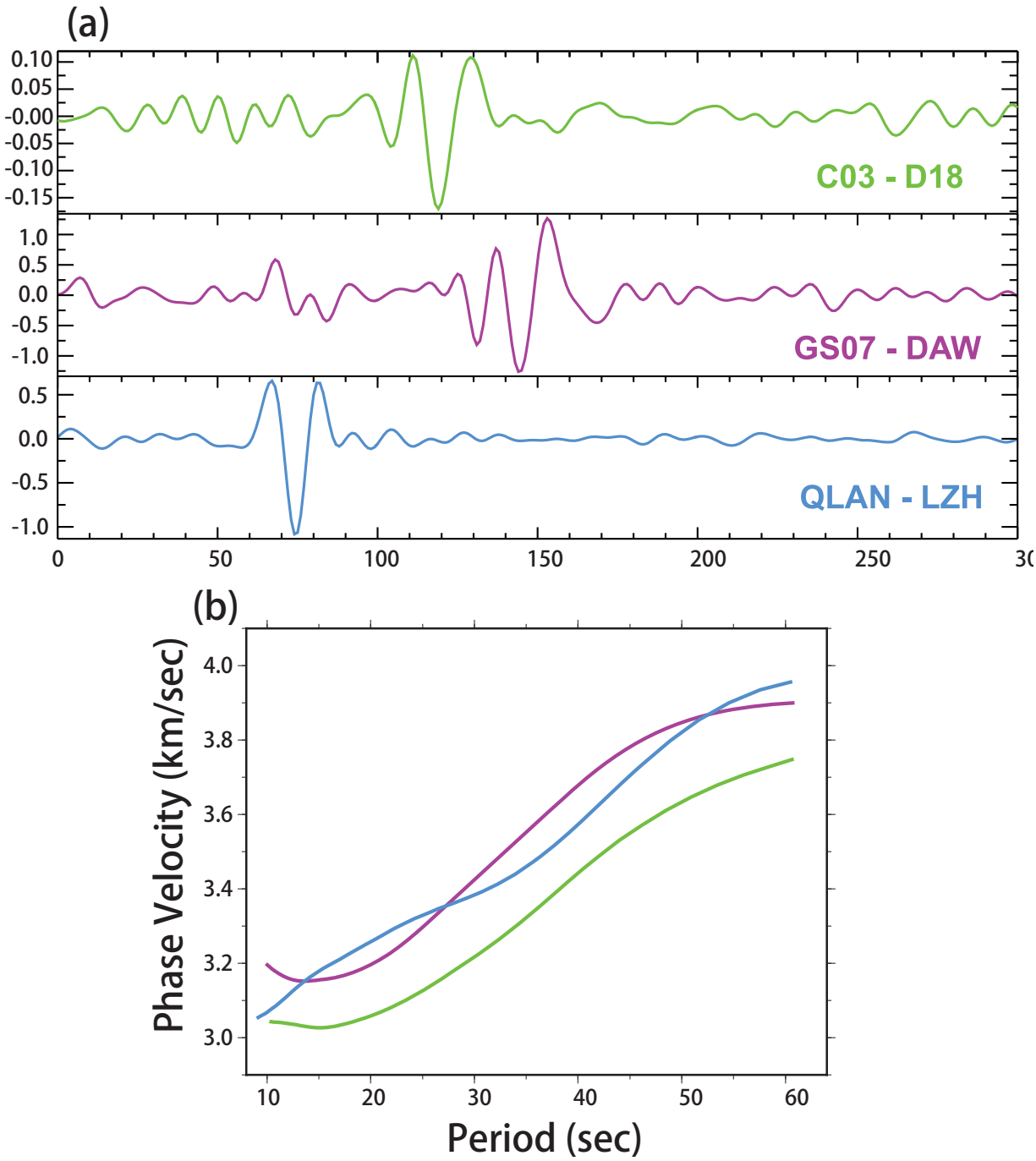

Figure 2.2: (a) Examples of the cross-correlations between station-pairs identified in Fig. 2.1b. (b) Computed Rayleigh wave phase velocity dispersion curves from the above cross-correlations. The stations DAW and LZH are from the Chinese provincial networks; the stations C03, D18 and GS07 are from the ASCENT array; the station QLAN is from the NETS array.

their corresponding dispersion curves are plotted in Figure 2.2. The dispersion curves in the Qiangtang and Songpan-Ganze Terranes between the station pair C03-D18 and in the west Qinling Orogen between the station pair DAW-GS07 both display negative slopes at 10-20 s periods, implying the presence of a low seismic velocity zone in the crust. However, the dispersion curve in the SE Qilian between the station pair QLAN-LZH displays monotonically increasing velocities with period, suggesting different crustal structures in the SE Qilian Orogen than in the Qiangtang, Songpan-Ganze Terranes and west Qinling Orogen.

Prior to performing tomography, data quality control is performed on the measured phase dispersion curves. This procedure is vital as it helps identify and reject bad measurements. To perform the data quality control, three criteria are adopted to retain high quality dispersion measurements for tomography: (1) the distance between each station-pair has to be longer than three wavelengths; (2) the signal-to-noise ratio (SNR), which is defined as the ratio between the maximum within a surface wave window defined by a group velocity of 2-4 km/s and the RMS of the trailing time series following the surface wave time windows, must be greater than 10; (3) the dispersion measurements must be fit well with misfits less than 3 s during tomography. After performing the data quality control, more than 10,000 cross-correlations are retained for periods shorter than 40 s; while, at 60 s period, ∼2,000 cross-correlations are left. The decrease of the number of paths towards the long period end is mostly due to the criteria of minimum three wavelengths for inter-station distances. The large number of cross-correlations ensures high density coverage of ray path in the study region (Figure 2.3a and b).

The retained phase dispersion measurements are then used to generate phase velocity maps on a $0.25^\circ \times 0.25^\circ$ grid using the tomography method of Barmin *et al.* (2001) as we did in Yang *et al.* (2010). During tomography, resolution is also simultaneously estimated. The resolution maps display an overall resolution of 30-50 km for most of the study areas (Figure 2.3c and d). To better visualize the resolution, we also conduct standard checkerboard tests at 25 and 40 s periods with anomaly sizes of $0.5^\circ \times 0.5^\circ$ and $0.75^\circ \times 0.75^\circ$. The results of checkerboard tests are shown in Figure 2.4. In most parts of the study region where path coverage is dense, including the east Kunlun Range, west Qinling Orogen, SW Qilian Orogen and NE Songpan-Ganze Terrane, velocity anomalies of $0.5^\circ \times 0.5^\circ$ are well recovered; while

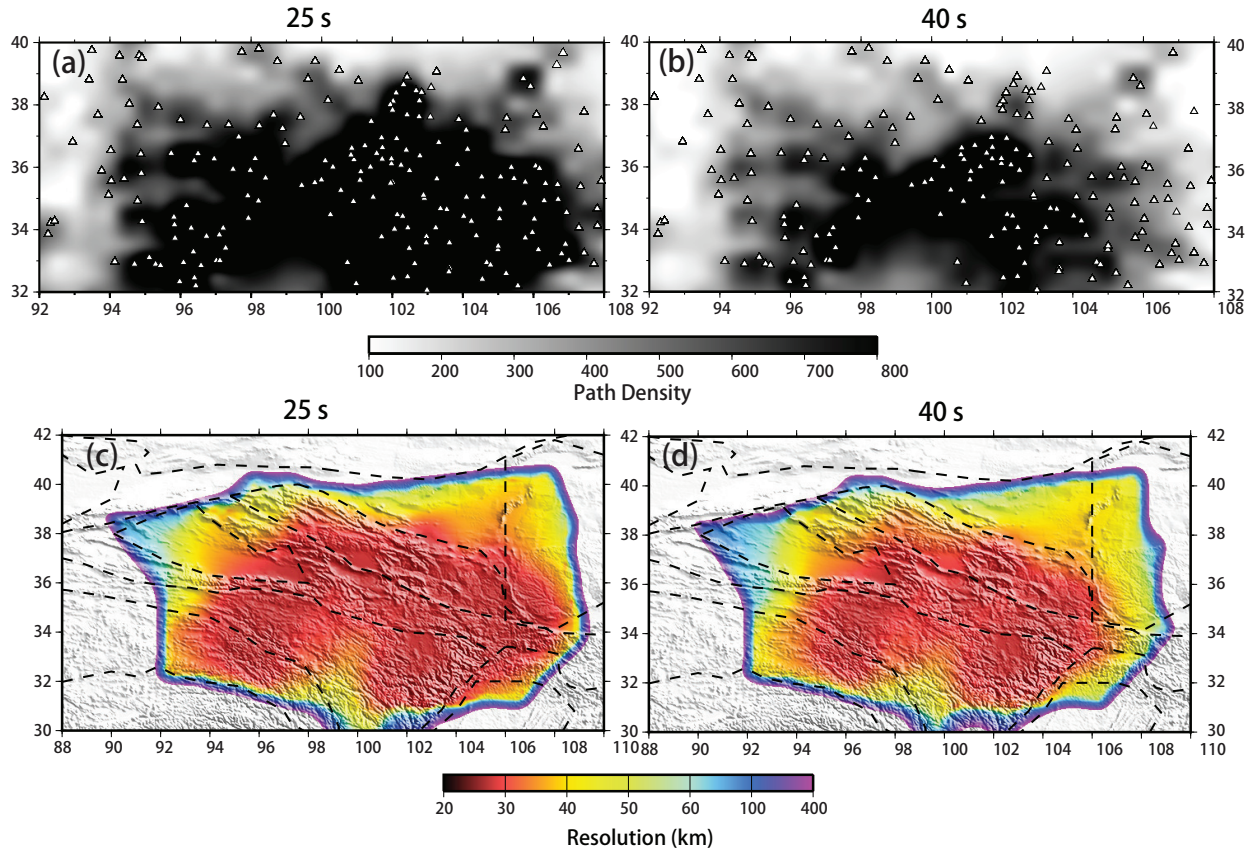

Figure 2.3: (a-b) The number of paths crossing each 0.5°×0.5° cell at 25 (a) and 40 (b) s periods respectively. The white triangles represent the seismic stations in the region.(c-d) Resolution maps at 25 and 40 s periods, presented as twice the standard deviation of the 2-D Gaussian fit to the resolution surface at each point.

in westernmost part of the study region, the resolution is slightly lower, and anomalies of $0.5^\circ \times 0.5^\circ$ are not resolved so well as in the central and eastern part, but anomalies of $0.75^\circ \times 0.75^\circ$ can be still well resolved.

2.4 Phase velocity maps

The resulting phase velocity maps at periods of 10, 25, 30 and 50 s are plotted in Figure 2.5. Large-scale velocity features are similar to those from our previous studies (Yang *et al.* (2012); Yang *et al.* (2010)]. However, the higher resolution of this study, estimated to be ∼30-50 km in most part of the study region, helps reveal more small-scale features.

At short periods less than 10 s, phase velocities are mostly sensitive to the upper crust

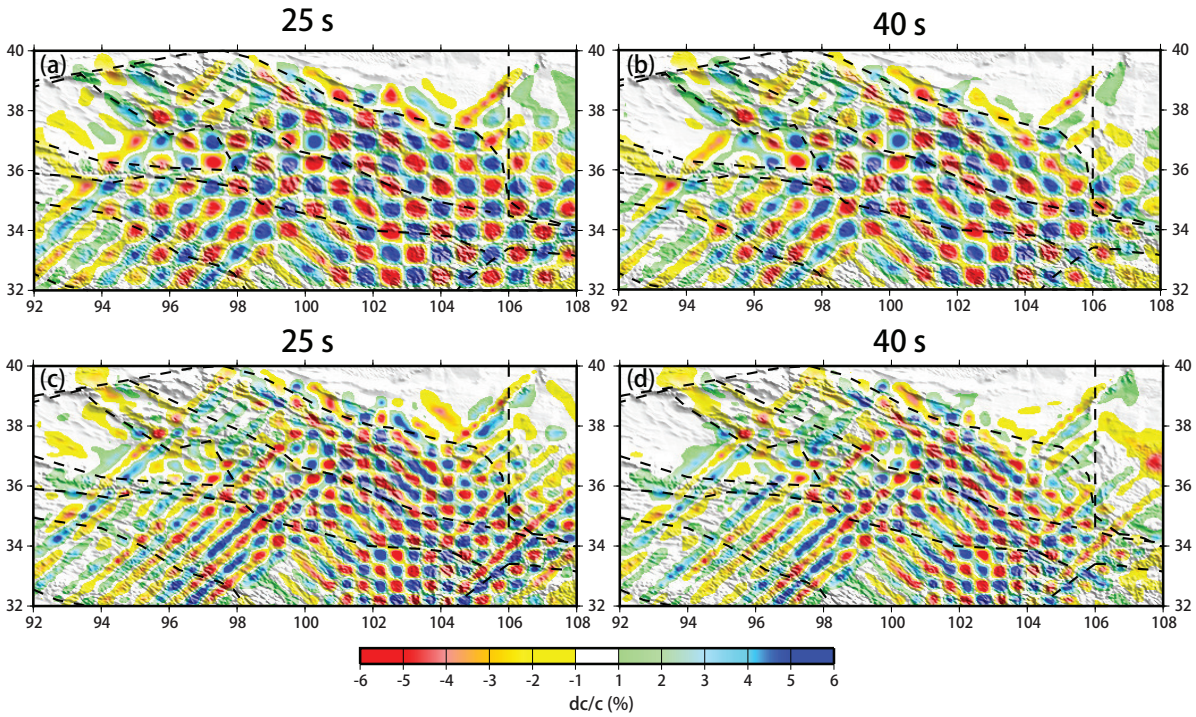

Figure 2.4: Recovered checkerboard structures with anomalies of $0.75^\circ \times 0.75^\circ$ (a, b) and $0.5^\circ \times 0.5^\circ$ (c, d) at 25 (left-hand column) and 40 s (right-hand column) period respectively.

where the presence of sedimentary layers in sedimentary basins results in much slower seismic velocities than in orogens and plutons. At these periods, low velocities are observed in the Qaidam Basin, northern Orodos Block and Sichuan Basin, where thick sediments are present. Noticeable low velocities are also observed in the Qiangtang and Songpan-Ganze Terranes with some patches of relatively high velocity regions separating the low velocities. In contrast, the Qilian, Kunlun and Qinling Orogens all exhibit high velocities.

At intermediate periods like 25 and 30 s, phase velocities are mostly sensitive to the middle crust. At these periods, nearly the whole NE Tibetan Plateau stands out as low velocities compared with the surrounding areas. Moreover, the low velocity anomalies extend 80-100 km northward across the Kunlun Fault into the west Qinling Orogen. Besides, low velocities are still observed in the central Qaidam Basin, where the sedimentary thickness is estimated to be more than 10 km [Yin *et al.* (2008)]. Comparable low velocities also exist in the NW Qilian Orogen. However, low velocities are not observed in the SE Qilian Orogen.

Phase velocities at 40-60 s periods, the long period end of this study, typically reflect the velocity structures of lower crust and uppermost mantle, and the Moho depth as well.

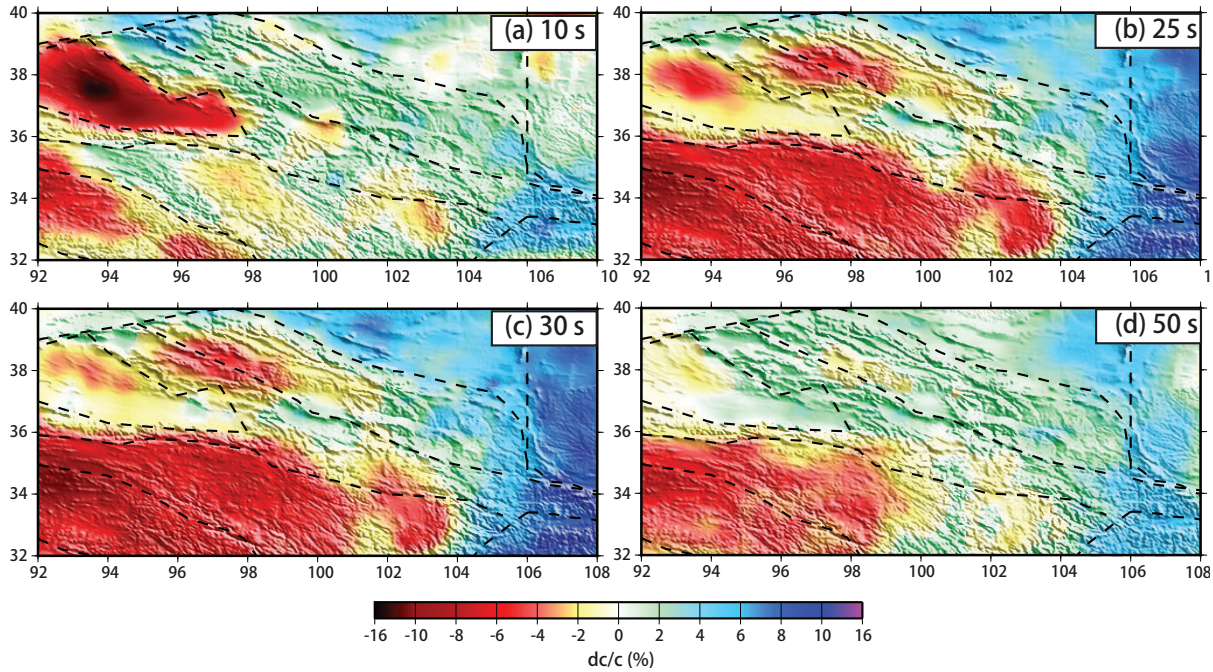

Figure 2.5: Rayleigh wave phase velocity maps at the periods of (a) 10 s, (b) 25 s, (c) 30 s and (d) 50 s, plotted as the percent perturbation relative to the average of each map (10 s: 3.086 km/s, 25 s: 3.333 km/s, 30 s: 3.436 km/s, 50 s: 3.797 km/s).

As seen in Figure 2.5d for 50 s phase velocity maps, strong low velocities are seen in the plateau where the double thickness crust is observed [Pan & Niu (2011); Shi *et al.* (2009); Vergne *et al.* (2002); Yue *et al.* (2012)]. Phase velocities gradually increase towards the neighboring areas of the NE Tibetan Plateau, reflecting the thinning of the crust away from the plateau.

Overall, the most prominent tomographic feature is the extension of low-velocity anomalies into the east Kunlun Range and west Qinling Orogen at 25-30 s periods, which is not clearly imaged nor extensively investigated by previous studies [Li *et al.* (2014); Yang *et al.* (2012)]. The estimated resolution of ∼30-50 km in these regions indicates that the extent of northward extension of the low-velocity anomalies is well resolved and robust.

From the resulting tomography images, we extract local dispersion curves at each geographic point, which reflects the subsurface seismic structures. In Figure 2.6a and b, six examples of local dispersion curves are displayed with their locations denoted in Figure 2.1a. The dispersion curves C and F from the Songpan-Ganze Terrane exhibit negative slopes at 10-20 s periods. The same pattern is also observed in the dispersion curve E, a point in

the west Qinling Orogen, which is consistent with the negative slope at 10-20 s periods in the inter-station dispersion curve of DAW-GS07 directly measured from cross-correlations as shown in Figure 2.2b. The local dispersion curves A, B and D, in the Qaidam Basin, east Kunlun Range and SE Qilian Orogen respectively, do not show the feature of negative slopes, indicating different crustal velocity structures beneath these regions.

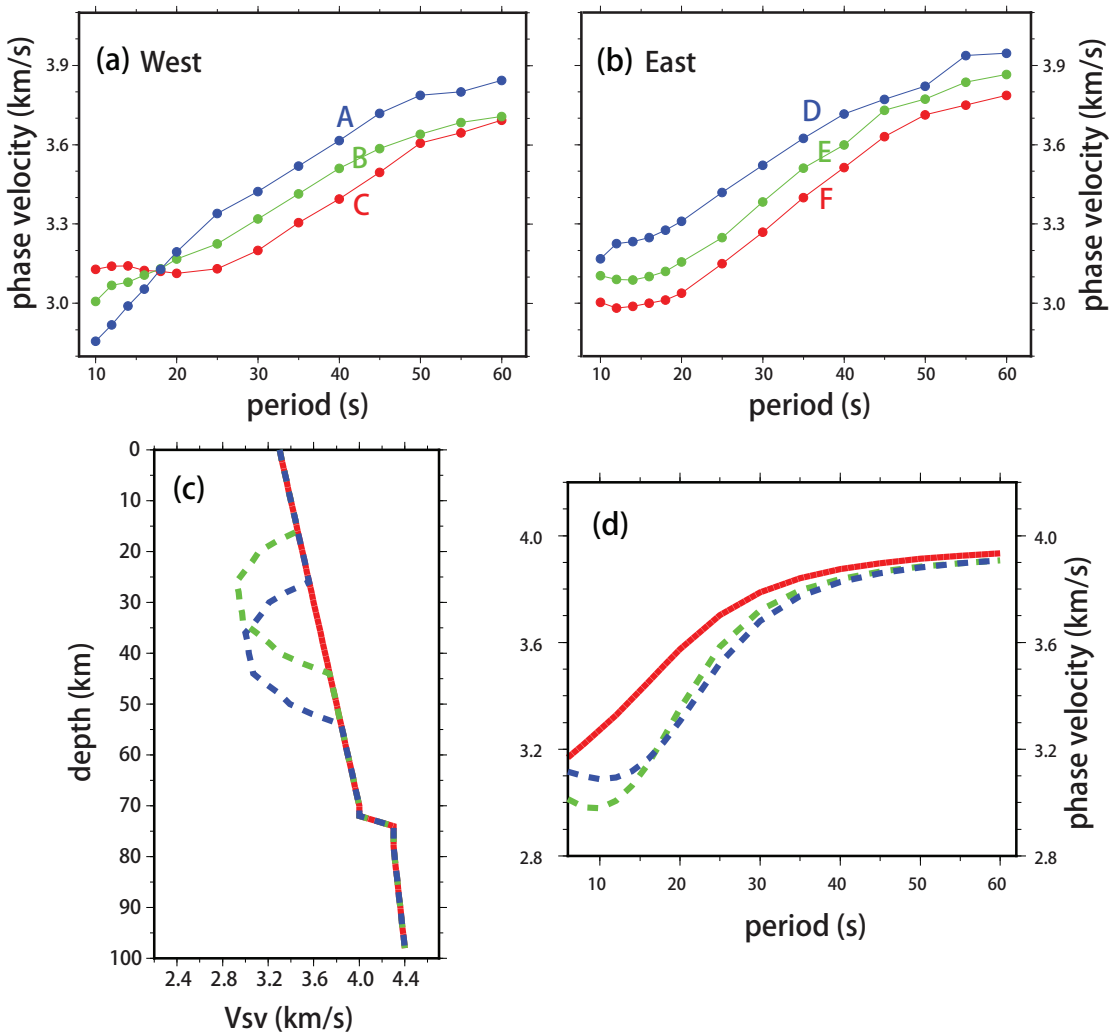

Figure 2.6: (a-b) Examples of local dispersion curves extracted from tomography maps at the locations identified by the coloured stars in Figure 2.1a. The blue, green and red lines in (a) represent dispersion curves extracted from the geological units of Qaidam Basin, east Kunlun Range and Songpan-Ganze Terrane respectively. Blue, green and red lines in (b) represent those located in South Qilian Orogen, Qinling Orogen and Songpan-Ganze Terrane respectively. (c) Synthetic velocity structures with and without LVZs. (d) The three corresponding dispersion curves predicted from the three velocity profiles shown in (c).

The presence of a negative slope in dispersion curves implies that there exists a low

velocity zone (LVZ) in the crust. To demonstrate the link between observed negative slopes in dispersion curves and features of LVZs, synthetic 1D Vs profiles are generated as shown in Figure 2.6c. In this figure, the three lines represent three different velocity models: the red line for a model without LVZ present, the green line for a model with a LVZ at the depth of 20-40 km and the blue line for a model with a similar LVZ as the green one but put at a greater depth. Corresponding dispersion curves for the three different models are calculated and plotted in Figure 2.6d. Similar features of negative slopes in the dispersion curves of the blue and green lines are observed as the real dispersion curves E and F shown in Figure 2.6b. It is reasonable to use the slope in dispersion curves at 10-20 s periods to judge whether a LVZ exists or not in the crust. However, to better constrain the amplitude and the depth of the LVZ, the inversion of local dispersion curves for 1D Vs profiles is needed, which is detailed in the following section.

2.5 Shear velocity inversion

The inversion of the extracted local dispersion curves for 1D shear velocity profiles is performed using a Bayesian Monte-Carlo method developed by Shen *et al.* (2013), which is briefly described below. More details of this method can be found in Shen *et al.* (2013). The method executes a comprehensive sampling through model space based on prior information to generate a posterior distribution of numerous acceptable models guided by a Metropolis algorithm [Shen *et al.* (2013); Yang *et al.* (2012)]. The model space is constructed using three layers from the surface to the depth of 150 km, including a single sedimentary layer if it exists according to the Crust 2.0 model [Bassin *et al.* (2000)], a crystalline crustal layer and an upper mantle layer. Three parameters are used to describe the sedimentary layer, including the layer thickness, Vsv at the top and bottom of the layer. Six parameters are employed to constrain the crystalline crustal layer, including the crustal thickness and five B-spline coefficients to represent Vsv variations with depth in the crystalline crust. In the upper mantle, five B-spline coefficients are used to represent Vsv variations from the Moho to 150 km depth. Thus, the model space is constructed using the total of 14 parameters described above.

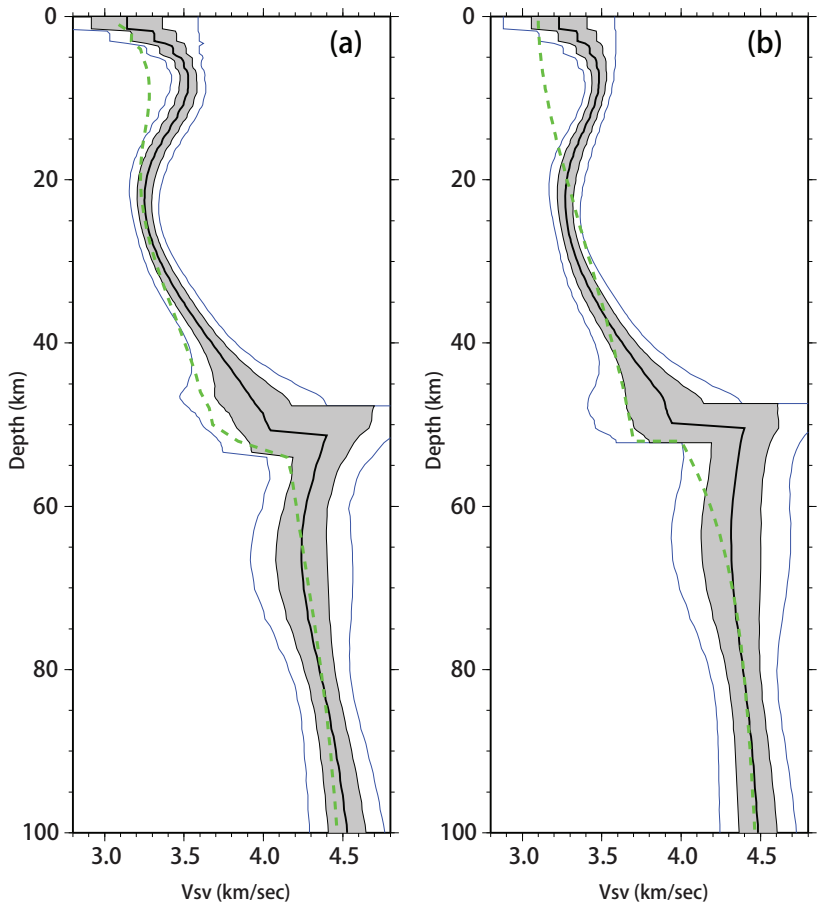

Figure 2.7: Inverted 1-D Vsv profiles at location E marked in Figure 2.1a with two completely different starting models (the dashed blue lines). The grey corridors identify one standard deviation around the mean produced from the Monte-Carlo inversion. The depths are all relative to the local surface. The green dashed lines represent the two different starting models for the Monte-Carlo inversion. The blue lines mark two standard deviations around the mean. The bold black lines are the average of the resulting ensemble of acceptable models from the Monte-Carlo inversion. Note that each of the three layers (the sedimentary layer, the crust layer and the upper mantle layer) is further divided into many sub-layers, resulting in a discrete appearance of 1D model in the figures.

To initiate the sampling, we take the Vsv model of Yang *et al.* (2012) as our starting model. As demonstrated in an example shown in Figure 2.7, the starting B-spline coefficients representing the starting Vs model have insignificant effects on the final Vs results. However, the starting model of Moho depth does strongly affect the final inversion results because surface waves alone cannot constrain velocity boundaries well. Thus, we investigate the impacts of the parameter of Moho depth on the inverted LVZs in section 2.7.1. When choosing acceptable models generated by the comprehensive sampling, the inversion method

takes four prior assumptions, including (1) Vsv linearly increases with depth in the sedimentary layer; (2) Vsv is free to vary in the crystalline crust; (3) Velocity contrasts across the sedimentary basement and the Moho are positive; 4) Vsv in the mantle is no more than 4.9 km/s.

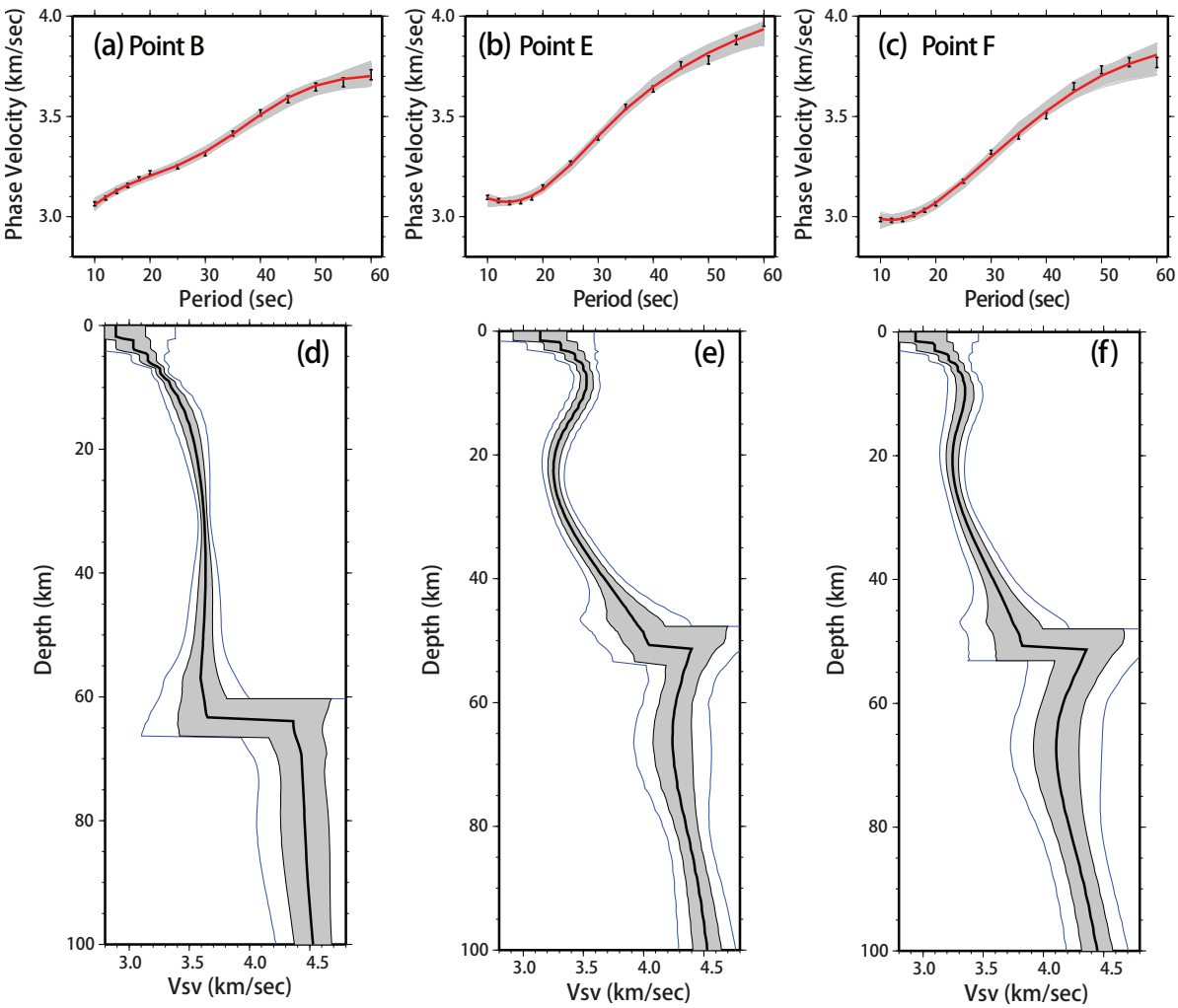

Figure 2.8: (a)-(c) Local phase velocity dispersion curves plotted with error bars at location B, E and F marked in Figure 2.1a. The grey lines present the predicted dispersion curves from accepted Vs models during inversion. (d)-(f) Inverted Vsv profiles at location B, C and F. The grey corridors represent one standard deviation around the mean produced from the Monte-Carlo inversion. The blue lines mark two standard deviations around the mean. The bold black lines are the mean of the resulting ensemble of acceptable models from the Monte-Carlo inversion. The depths are all relative to the local surface.Note that each of the three layers (the sedimentary layer, the crust layer and the upper mantle layer) is further divided into many sub-layers, resulting in a discrete appearance of 1D model in the figures.

During model space sampling, a dispersion curve is calculated from each constructed velocity model with prior assumptions listed as below. The crust and mantle are assumed as Poisson solids with Vp/Vs ratio set to 1.73; while, for the sedimentary layer, the Vp/Vs ratio is set to 2.0 by taking a median value of the ratio for the Vs range of 1.0-2.5 km/s [Brocher (2005)]. Density is calculated following the linear relation: $density = 0.541 + 0.3601 * Vp$ [Brocher (2005)] suggested by Christensen & Mooney (1995), in which the Vp is converted from the Vs according to the Vp/Vs ratio in each layer. In addition, attenuation effects on dispersion curves are corrected [Kanamori & Anderson (1977)] using Q values modified from the PREM model [Dziewonski & Anderson (1981)] following Yang *et al.* (2012).

The Bayesian Monte-Carlo inversion is executed for the local dispersion curve at each geographic point on a $0.25^\circ \times 0.25^\circ$grid. The resulting posterior distribution of the Bayesian Monte-Carlo sampling is a series of 1D Vsv profiles at each point. The mean of the distribution is taken as the final Vsv profile. The standard deviations of the distribution are taken as the Vsv uncertainties. Three examples of the constructed 1D Vsv profiles are presented in Figure 2.8 with their corresponding locations marked as points B, E and F in Figure 2.1a. Point B in the eastern Kunlun Range, where phase velocities increase with period, exhibits monotonically increasing Vsv with depth; while the other two points, one from the Songpan-Ganze Terrane and the other from the west Qinling Orogen, have Vsv profiles with strong LVZs in the middle crust and the minimum velocities appearing at 20-25 km depths. This is consistent with the results of forward modelling in section 2.4 in which negative slopes in dispersion curves reflect the presence of a LVZ in the crust.

2.6 The 3-D Vsv model

Figure 2.9 displays Vsv maps and their uncertainties at 10, 30 and 60 km depths as well as the estimated crustal thickness and its associated uncertainties. The Vsv maps are plotted as the velocity perturbations relative to the average velocities at individual depths. The uncertainties at the depths shallower than 40-50 km are ∼30-40 m/s for most of the study area, but increase towards the eastern edge around the Ordos Block where the station coverage is sparser. The uncertainties at 60 km depth are larger compared to those at shallower depths,

which is expected and mainly caused by the strong trade-off between the Moho depth and the velocities of lowermost crust and uppermost mantle.

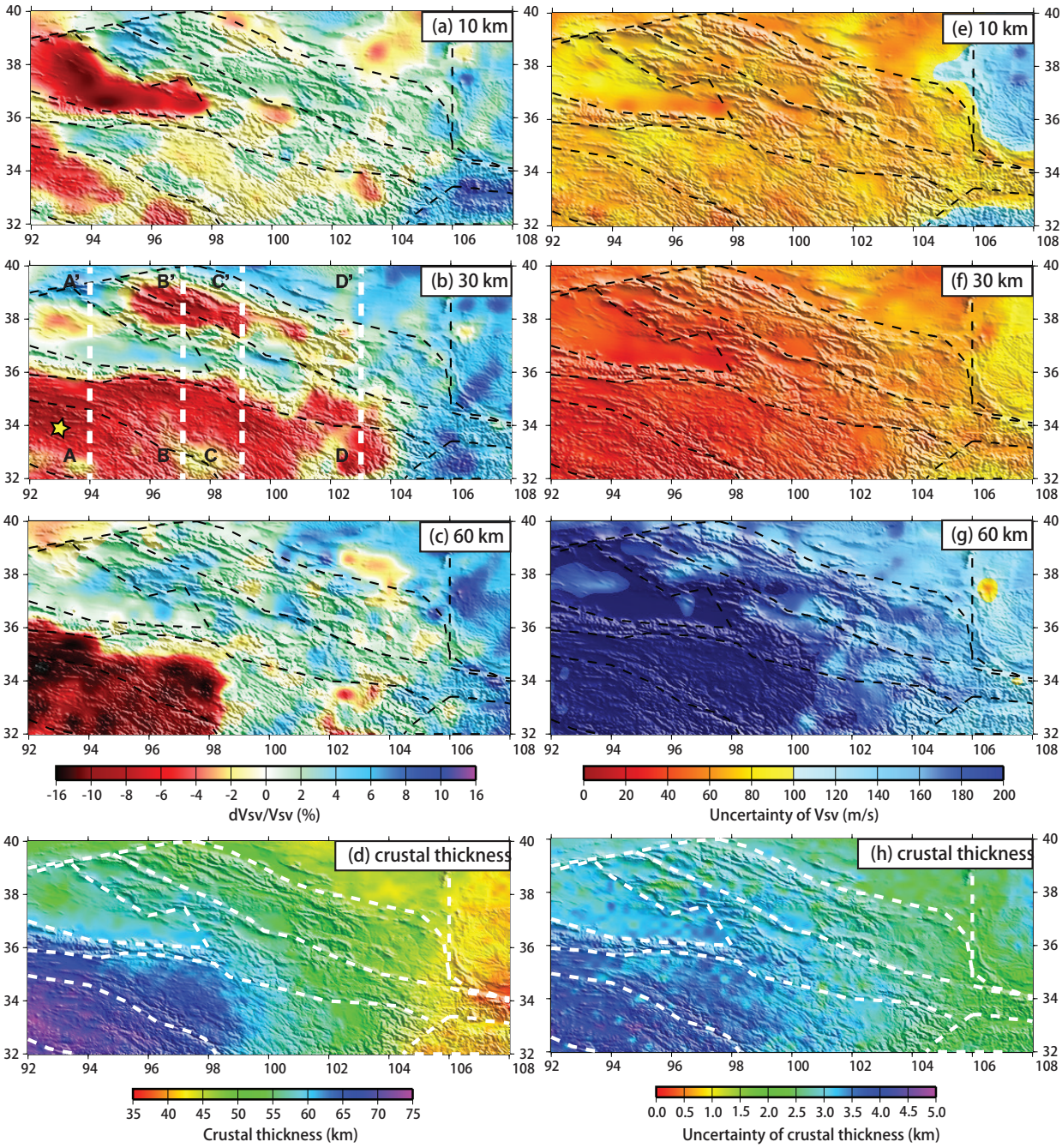

Figure 2.9: (a-c) Vsv maps at the depths of 10, 30 and 60 km respectively, plotted as perturbations relative to the averages across the entire research area. All depths are relative to sea level. (d) Map of estimated crustal thickness. (e-g) Maps of the Vsv uncertainties at each depth corresponding to the left panel. (h) Uncertainties of the estimated crustal thickness.

In the upper crust, strong low velocities are mainly imaged in the Qaidam Basin where sedimentary layers are believed to be thicker than 10 km [Yin *et al.* (2008)]. Noticeable low velocities are also seen in the Qiangtang and Songpan-Ganze Terranes; while most of the Qilian Orogen and Orodos Block show high velocities. Different from the upper crust, in the middle crust, such as at 30 km depth (Figure 2.9b), the Qiangtang Terrane, Songpan-Ganze Terrane and NE Qilian Orogen exhibit much lower velocities compared to the surrounding areas. Similar to the observations from tomography results, the lateral distributions of the low velocities exhibit different patterns from west to east along the Kunlun Fault. More specifically, in the west of $98\,^{\circ}E$, the low velocities reach the Kunlun Fault and east Kunlun Range but are absent beneath the Qaidam Basin. In the east of $98\,^{\circ}E$, low velocities, however, extend northward across the Kunlun Fault and penetrate into the Qinling Orogen over 100 km along the segment of $101\,^{\circ}E - 104\,^{\circ}E$. A comparable low velocity patch is also imaged in the NW Qilian Orogen and this low velocity patch appears to be not connected with the broader low velocity areas in the NE Tibetan Plateau, which is consistent with the result of Li *et al.* (2014). As suggested in Li *et al.* (2014), the LVZs beneath the NW Qilian Orogen may be an intra-crustal response to the far field effects from the Indian-Eurasian collision. At the depths of 50-60 km (Figure 2.9c), most of the regions in the NE Tibetan Plateau show much lower velocities compared to the surrounding areas. This is due to the reason that at these depths (Figure 2.9d), the velocities in the plateau are still crustal velocities; while velocities in surrounding areas already reflect the seismic velocities of the uppermost mantle.

To better examine the vertical extent of LVZs, four transects of absolute Vsv along the dashed lines marked in Figure 2.9b are plotted in Figure 2.10. Transects A-A' and B-B' are located in the west of $98\,^{\circ}E$, crossing the geological units of the Qiangtang, Songpan-Ganze, east Kunlun Range, Qaidam Basin and the west Qilian Orogen from south to north. As outlined by the black contour, LVZs are observed throughout the middle crust of the NE Tibetan Plateau although the minimum velocities vary slightly. LVZs are mainly present at $\sim$18-35 km depths with their northern extent clearly terminating right in the front of the Kunlun Range and Kunlun Fault. LVZs certainly do not appear beneath the Qaidam Basin. Contrary to the observations in the west, LVZs in the east of $98\,^{\circ}E$ clearly penetrate to the

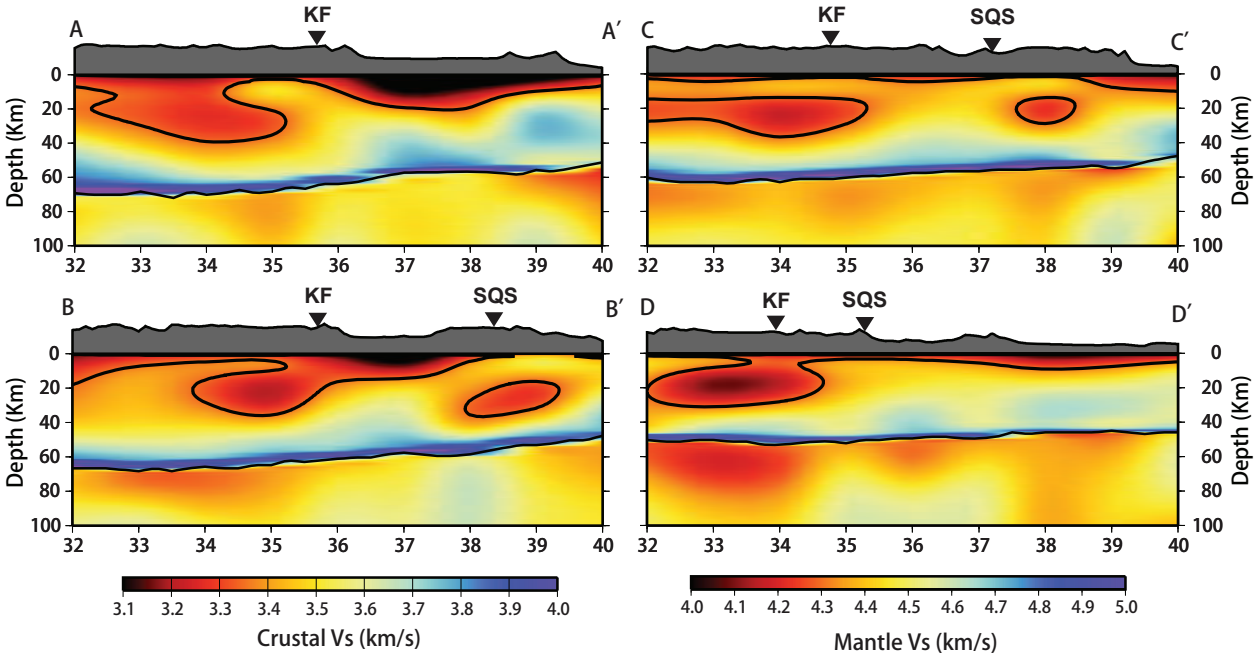

Figure 2.10: Vertical cross-sections of Vsv plotted as absolute velocities along the four lines marked as the white dashed lines in Figure 2.9b. All depths are relative to sea-level. Black triangles on the top of each cross-section denote the surface locations of the Kunlun Fault (KF) and South Qilian Suture (SQS). The black contour outlines areas with Vsv less than 3.4 km/s.

north, extending 100 km beyond the Kunlun Fault at the comparable 15-35 km depths as shown in transects C-C' and D-D'.

One advantage of the Bayesian Monte-Carlo inversion is that the possibility of a certain feature in the model, such as the presence of LVZs in the middle crust, can be estimated. To assess the possibility of the presence of LVZs in the middle crust, we plot the percentage of accepted Vsv models (Figure 2.11) at each geographic point with the minimum Vsv at 15-40 km depth range smaller than Vsv at both 15 and 40 km depths, which apparently indicates the presence of LVZs in the middle crust. Comparing this possibility map (Figure 2.11) with the Vsv map at 30 km depth shown in Figure 2.9b, we find that, in most of the regions with LVZs (Figure 2.9b), more than 80% of the models of the posterior distributions from the inversion have LVZs in the middle crust at ∼15-40 km depths, indicating the resolved distributions of LVZs is statistically robust.

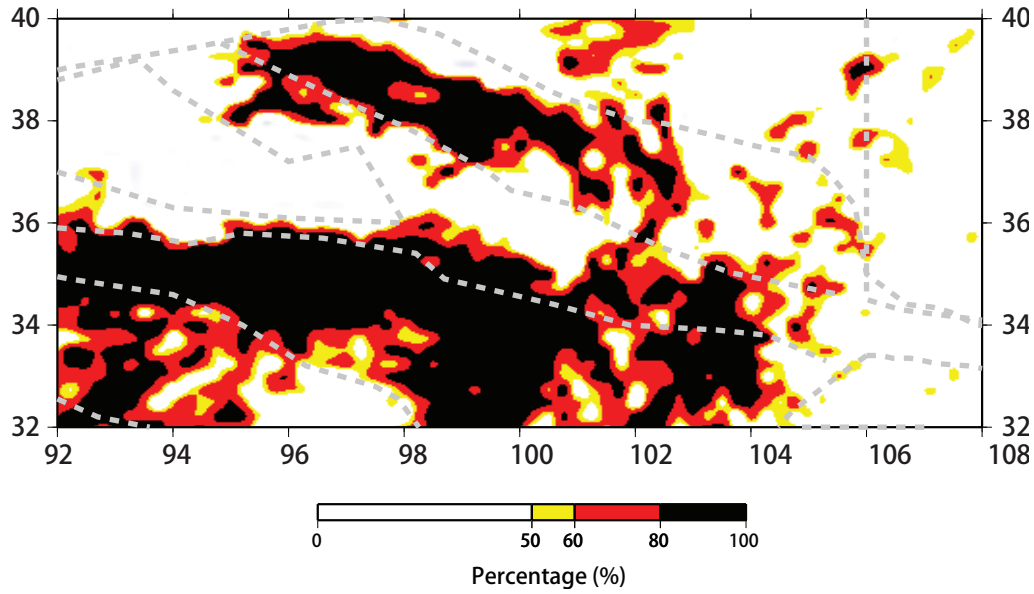

Figure 2.11: Percent of accepted models from the Monte-Carlo inversion with the minimum Vsv at 15-40 km depth range smaller than Vsv at both 15 and 40 km depths for each geographic location on a grid of $0.25^\circ \times 0.25^\circ$.

2.7 Discussion

2.7.1 Resolution tests

Our 3D Vsv model reveals that there are pronounced mid crustal LVZs in the NE Tibetan Plateau, and the LVZs display distinct distribution patterns along the Kunlun Fault (Figures 2.9 and 2.10) with LVZs sharply terminating at the Kunlun Range in the west of $98^\circ E$, but extending northward to the Qinling Orogen in the east of $98^\circ E$. Presented with the sharp lateral variations of LVZs, one may wonder whether such strong lateral variations could really be resolved by our tomography and whether smoothing and possible smearing in surface wave tomography could contribute to the lateral variations of LVZs along the Kunlun Fault.

To assess these concerns, we perform resolution tests by designing a testing model with a low velocity zone located at 20-40 km depths in the areas where LVZs are imaged but with its northern extent sharply bounded by the Kunlun Fault. The background model is homogeneous except that the variations of Moho depth from our 3D model are added into the model. In the background model, shear velocities in the crust linearly increase with a slope of 0.008 km/s per km depth from the surface to local Moho depths starting from 3.3

km/s at the surface. A 0.4 km/s velocity jump is added across the Moho. Then, shear velocities in the upper mantle linearly increase again with the same slope of 0.008 km/s per km depth to 4.5 km/s at 100 km depth. On top of that, LVZs with 10% velocity reduction are introduced in the depth range of 20-40 km beneath the targeted regions. The map view of the synthetic model at 30 km depth and a cross section along latitude $97^{\circ}N$ are plotted in Figure 2.12a. To generate synthetic data, we first calculate local dispersion curves at 10-60 s periods and then construct phase velocity maps at each individual period. Based on the phase velocity maps, we calculate inter-station dispersion curves for all the station pairs we get from real data. To make the synthetic data more realistic, we also add Gaussian random noise with a 0.5 s standard deviation to the inter-station phase travel time, which is about the standard deviation of the phase travel time misfits in the tomography for real data. The same inversion procedures as we apply to the real data are applied to the synthetic data. The recovered model from the synthetic data is plotted in Figure 2.12b. Compared with the synthetic model, the distributions of the LVZs are recovered very well, and the LVZs along the Kunlun Fault are well delineated without suffering from smearing and smoothing.

Another synthetic model, in which LVZs extend across the Kunlun Fault from the NE Tibetan Plateau with the distribution pattern and amplitude of the LVZs similar to the inverted LVZ, is also designed to test whether the features of penetration can be well recovered. The testing results are demonstrated in Figure 2.13, which shows that the penetration of the LVZs into the west Qinling Orogen are recovered almost perfectly without noticeable differences in the lateral extent of the LVZ between the recovered model and the synthesised model.

As mentioned in section 2.6, the uncertainties of Vsv increase at depths right above and beneath the Moho due to the trade-off between the Moho depth and velocities in the lowest crust and uppermost mantle. We thus investigate whether the trade-off between the velocities and the Moho depth will affect the distribution and amplitude of our inverted LVZs in the middle crust. To address this question, we use the same synthetic model as described in the preceding resolution testing. In the inversion for 1D Vsv profiles from observed local dispersion curves, the Moho depth is allowed to change within a range of 10%. In this test, we allow the Moho depth to vary in a 20% range from the starting model, which should

be large enough to accommodate the real Moho depth even given the large uncertainties of Moho depth in the starting model. The results of the test are plotted in Figure 2.12c with a velocity map at 30 km depth and a cross section along the latitude 97 °N. Although the exact Moho depth in the recovered model is affected by the trade-off, the distribution and amplitude of inverted LVZs at 20-40 km depth are well recovered without suffering from the impact posed by the trade-off.

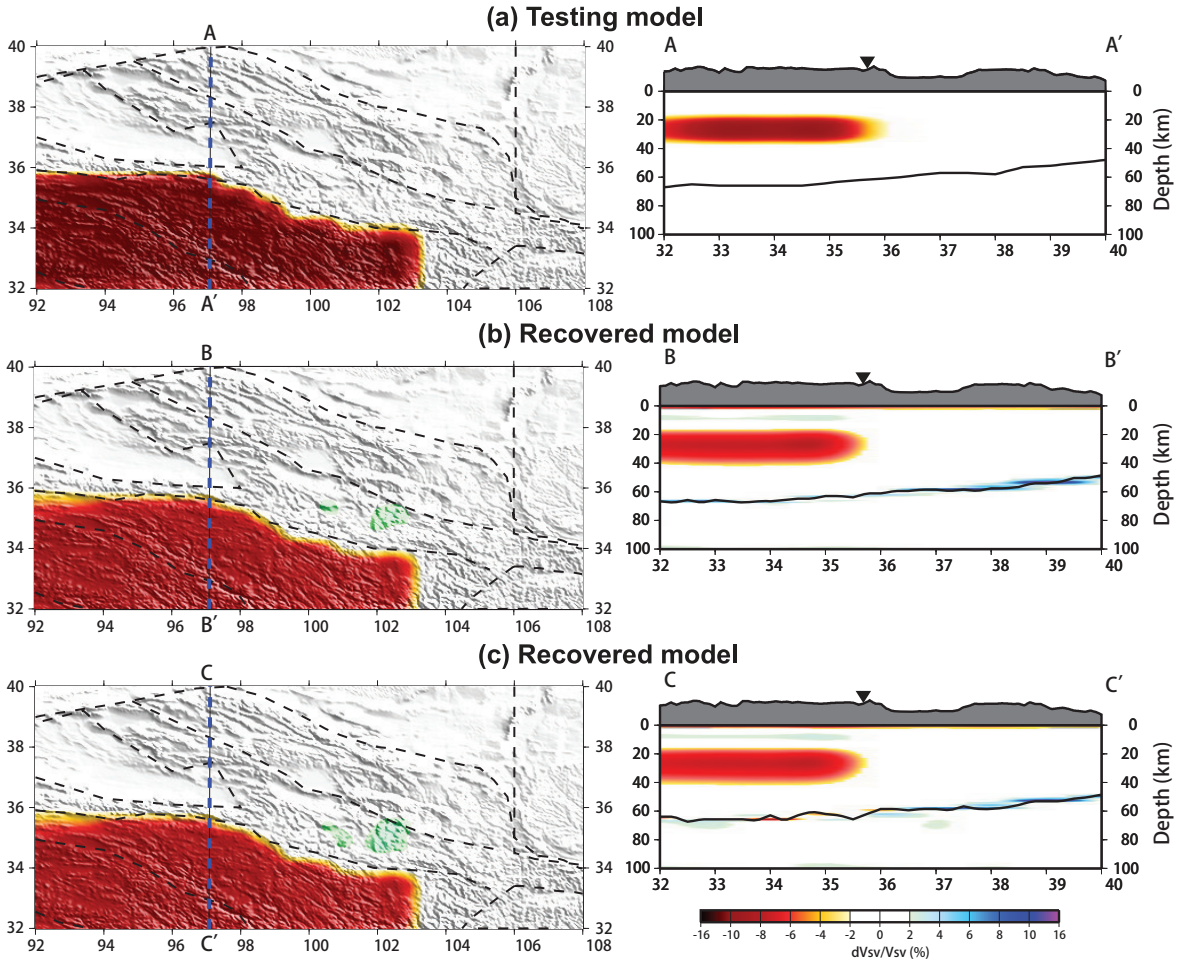

Figure 2.12: Results of resolution tests. All figures are plotted as perturbations relative to the initial model without LVZs. The left-hand columns are Vsv maps at 30 km depth; the right-hand columns are Vsv cross-sections along the longitude 97 °E, where the black lines indicate the Moho. (a) The testing model. (b) The recovered model obtained applying the exact same inversion procedure as real data. (c) The recovered model obtained by allowing the Moho to vary in larger depth range than in (b).

2.7.2 The origin of LVZs

To completely understand the origin of the LVZs across the NE Tibetan Plateau, we need to know temperature, pressure, rock types and their mineral compositions in the middle crust, each of which is not a trivial task and is out of scope of this study. Very recently, Hacker *et al.* (2014) have calculated seismic velocities of middle crustal rocks in central Qiangtang based on well constrained temperature gradient and rock types from xenoliths. They found that seismic wave speeds calculated from a range of dry mid-crustal rocks cannot match the observed low shear seismic speeds in the middle crust at ∼25-45 km depths. They concluded that low velocities and at least 4% radial anisotropy [Xie *et al.* (2013)] observed in the mid/lower crust require the presence of a partially melted, mica-bearing layer. The point used in their calculation and treated as a typical point for the Tibetan Plateau is located at $(93\,^{\circ}E, 34\,^{\circ}N)$, which is very close to the eruption site of the xenoliths, marked by the star in Figure 2.9b. The LVZs in the mid crust from our study beneath most areas of the NE Tibetan Plateau are more-or-less close to the velocities at the selected point of Hacker *et al.* (2014), which may suggest that the existence of partial melt in the mid/lower crust of the plateau may be quite widespread if we assume the thermal status and rock compositions are similar across the NE Tibetan Plateau.

A magnetotelluric profile collected in the west part of our study area imaged a highly conductive mid-crustal layer [Le Pape *et al.* (2012)] with its depth and shape very close to our observed LVZs, which probably indicates that the low seismic velocities and high conductivities have the same origin, very likely the presence of partial melt as interpreted by previous magnetotelluric studies [Le Pape *et al.* (2012); Unsworth *et al.* (2004); Wei *et al.* (2001)]. In addition, a recent discovery of Malanshan-Bukadaban rhyolites [Wang *et al.* (2012)] near the margin of the northern Tibetan Plateau (marked by the diamond in Figure 2.1a), which are suggested to be generated by dehydration melting of the mid/lower crustal rocks, provide direct petrologic evidence for the existence of partial melt.

Partial melting in the middle crust of NE Tibetan Plateau could be triggered by radioactive heating of partially subducted crustal materials [Jamieson *et al.* (1998)] in the

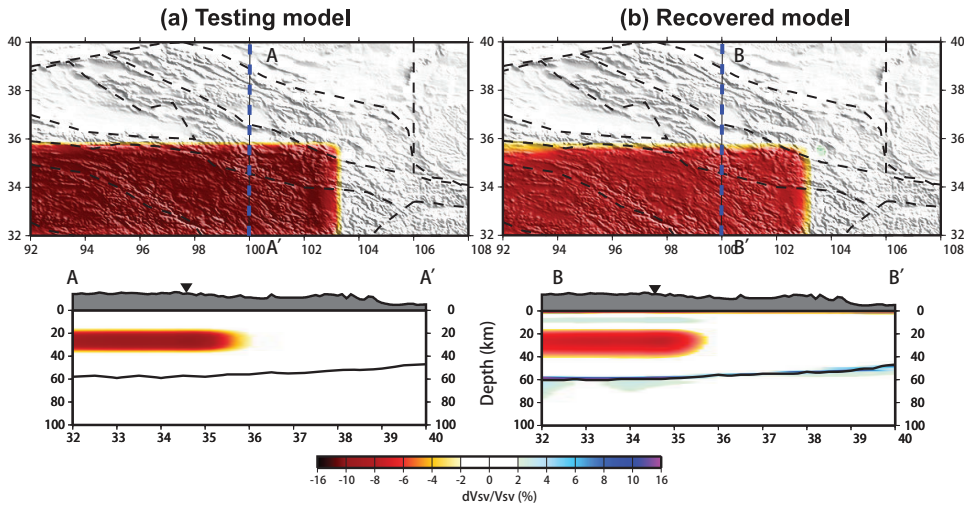

Figure 2.13: Resolution tests for a synthetic model with LVZs across the Kunlun fault in the east of 98 °E. Left-hand column: Vsv map of the testing model plotted at 30 km depth and a cross-section A-A' along the longitude of 100 °E. Right-hand column: same as the left-hand column, but for the recovered model.

double-thickened crust, which contain high concentration of radioactive elements in meta-sedimentary rocks [Wollenberg & Smith (1987)], or by a hot asthenosphere upwelling resulting from lithospheric thinning beneath the north Tibetan Plateau [Chung *et al.* (2005); Turner *et al.* (1993)]. The high thermal status in the plateau is supported not only by the occurrence of extensive young potassium magmatism [Chung *et al.* (2005); Ding *et al.* (2007)], but also by some direct and indirect thermal estimates, including a temperature of 700 °C at 18 km depth inferred from seismic detection [Mechie *et al.* (2004)]; the depth of the Curie isotherm of 550 °C at ∼15 km depth inferred from satellite magnetic measurements [Alsdorf & Nelson (1999)]; a temperature of $800 - 1000$ °C at the depth of 30-50 km indicated by the xenoliths erupting from the mid to deep crust of the Qiangtang Block [Hacker (2000)].

2.7.3 The geological implications of the observed distribution of LVZs

Our 3D Vsv model shows that strong and ubiquitous LVZs exist in the middle crust of NE Tibetan Plateau, and reveals the detailed distributions of the LVZs along the Kunlun Fault, the north boundary of the Tibetan Plateau. In the west of 98 °E, LVZs reach the Kunlun

Fault and the eastern Kunlun Range, but are not observed beneath the Qaidam Basin, while, in the east of $98\,^{\circ}E$, LVZs extend and penetrate northward into the east Kunlun and Qinling Orogen over at least 100 km.

Along a profile in the west part of our study region striking NE from point $(92\,^{\circ}E, 33.5\,^{\circ}N)$ to point $(95\,^{\circ}E, 36.5\,^{\circ}N)$, electrical structures from an improved magnetotelluric method show that a highly conductive mid-crustal layer has penetrated into the Kunlun Range [Le Pape *et al.* (2012)]. Le Pape *et al.* (2012) interpret the highly conductive layers as a partially molten layer and postulate that the penetration of crustal melts probably characterises the growth of the plateau to the north. Our observed LVZs along that profile have a similar pattern as the highly conductive mid-crustal layer, consistent with the interpretation of the northward growth of Tibetan Plateau by Le Pape *et al.* (2012). Our 3D model reveals a detailed distribution of LVZs over a broad region of NE Tibetan Plateau, which may provide a large picture of the growth mode in the NE Tibetan Plateau (Figure 2.14).

The distinct distribution pattern of mid-crustal LVZs from west to east along the Kunlun Fault may be related to the different tectonic units neighboring the Kunlun Fault in the north. A strong crust of the colder and high-velocity Qaidam Basin in the west may be blocking the penetration of LVZs, but a weak crust in the Qinling Orogen may be facilitating the extrusion of LVZs. The weaker crust of the Qinling Orogen could be in part due to the fact that its chemical composition is rather felsic as constrained by refraction and reflection explorations [Liu *et al.* (2006); Pan & Niu (2011)], and felsic rocks are usually weaker than intermediate/mafic rocks under the same temperature and pressure conditions [Wilks & Carter (1990)]. The blocking of the LVZs in the west by the Qaidam Basin may in turn contribute to the slightly thicker crust [Shi *et al.* (2009); Vergne *et al.* (2002); Xu *et al.* (2014); Yue *et al.* (2012)] in the west than in the east.

As discussed in section 2.7.2, the existence of partial melt in the middle crust of NE Tibetan Plateau is highly possible. Based on experimental results, melt volumes of 1-8% could significantly decrease the strength of rocks, maybe up to 90% of its initial value [Jamieson *et al.* (2011)]. Partial melting in the middle crust results in a much weaker mid-crustal channel [Beaumont *et al.* (2006); Clark & Royden (2000)], which could flow under the northward push by the Indian Plate. Xie *et al.* (2013) report 5-6% radial anisotropy with

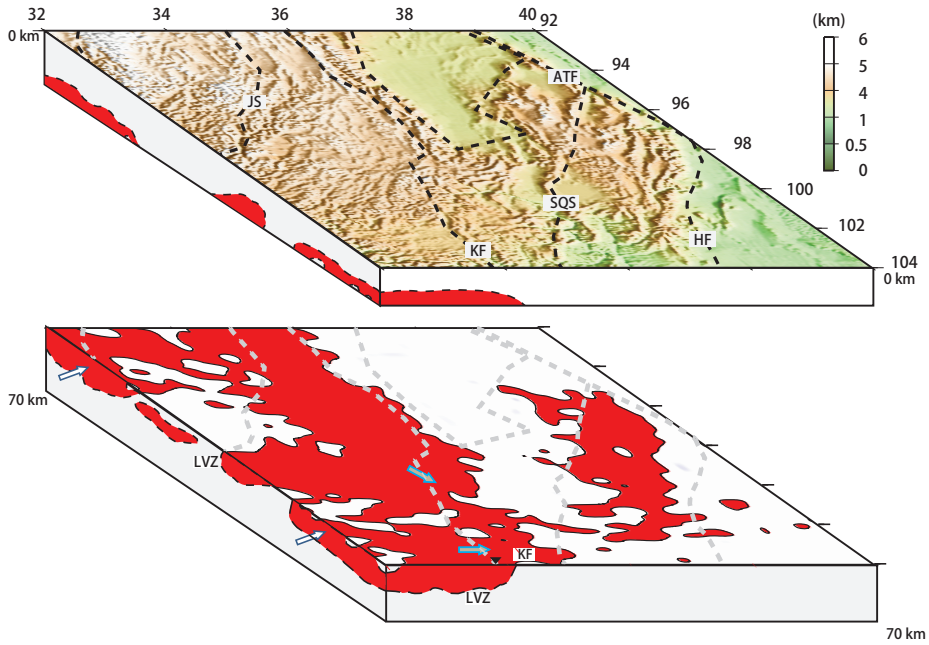

Figure 2.14: Cartoon of the distribution of crustal LVZs beneath the NE Tibetan Plateau. The upper panel shows the topography of the research area with geological boundaries including HF-Haiyuan Fault, ATF-Altyn Tagh Fault, SQS-South Qilian Suture, KF-Kunlun Fault, JS-Jingsha Suture. The lower panel is the distribution of LVZs with the red regions outlined by a contour of 70% probability for the existence of LVZs in the middle crust from Figure 2.12. The open arrows represent possible flow of the crustal LVZs. The vertical extent of the LVZs drawn with dashed lines is just for illustration.

Vsh higher than Vsv in the middle crust of eastern Tibetan Plateau and consider that the radial anisotropy is caused by a shallow dipping foliation of sheet silicates, such as mica. The shallow dipping foliation of mica could be caused by sub-horizontal simple shear as the result of the north-eastward flow of the weak and ductile mid-crustal channel. This is also consistent with the interpretations of the existence of sub-horizontal simple-shear zones in the NE Tibetan Plateau from seismic reflection data [Wang *et al.* (2011)] although the mechanisms for the deformation may be complicated.

If blocked by the Qaidam Basin, the weak and ductile mid-crustal rocks may pile up in the west and tend to move eastward along the left-strike slip Kunlun Fault during the eastward extension [Klemperer (2006); Royden *et al.* (2008); Shapiro *et al.* (2004)] of the whole plateau. At the bending segment of the Kunlun Fault around 98 $^{\circ}E$, they may start to move north-eastward because of the weaker crust in that region. The flow may become stronger towards the east part where the neighboring crust is weak and facilitates the broad

extrusion of the weak and ductile mid-crustal rocks into the Qinling Orogen, transferring the surface deformation along the boundary of the Kunlun Fault partially into the mid crust. Thus the possible increasing flow in the mid crust is consistent with the eastward decrease of the slip rate along the Kunlun Fault on the surface [Kirby *et al.* (2007)]. Although the observed LVZs show a complicated distribution (Figure 2.14), in a nutshell, the pattern of the distribution of observed LVZs is consistent with the channel flow model which can explain the extrusion of mid-crustal channels in the NE Tibetan Plateau [Clark & Royden (2000); Royden *et al.* (2008); Searle *et al.* (2011)].

2.8 Conclusion

Based on the analysis of continuous ambient noise data collected from 280 stations between 2008 and 2010 in the NE Tibetan Plateau and surrounding regions, a 3-D Vsv model with a resolution of ∼30-50 km is constructed. Our 3D model reveals strong LVZs in the middle crust across NE Tibet and shows significant variations of lateral distribution of LVZs from west to east along the Kunlun Fault. In the west of $98^{\circ}E$, LVZs are confined to regions of the Kunlun Fault and the eastern Kunlun Range but absent beneath the Qaidam Basin, while in the east of $98^{\circ}E$, LVZs extend beyond the Kunlun Fault and penetrate northward into the Qinling Orogen over 100 km. Regions with strong LVZs are coincident with the regions with strong mid-crustal radial anisotropy [Xie *et al.* (2013)], which can be explained by the mid-crustal channel flow model aided by a partially melted mica-bearing mid/lower crustal layer [Hacker *et al.* (2014)]. Our 3D model clearly delineates the north extent of the mid-crustal LVZs, probably reflecting the status of channel flow in the NE Tibetan Plateau.

3

Crustal structure in the junction of Qinling Orogen, Yangtze Craton and Tibetan Plateau: implications for the formation of Dabashan Orocline and the growth of Tibetan Plateau

3.1 Abstract

The crust at the conjunction of Qinling Orogen, Yangtze Craton and NE Tibetan Plateau bears imprints of the Triassic collision and later intra-continental orogeny between Qinling Orogen and Yangtze Craton, and the Cenozoic growth of Tibetan Plateau. Investigating detailed crustal structures of this region helps better understand these tectonic processes. In

this study, we construct a 3-D crustal Vs model using seismic ambient noise data recorded at 321 stations. Ambient noise tomography is performed to generate Rayleigh wave phase velocity maps at 8-50 s periods, which are then inverted for a 3-D isotropic Vs model using a Bayesian Monte-Carlo method.

Our 3-D model reveals deep-rooted high velocities beneath the Hannan-Micang and Shennong-Huangling Domes, which are located on the two sides of Dabashan Orocline. These high velocities likely represent intrusive complexes and uplifted basement rocks. Prominent high velocities are also present in the upper/mid crust of the western Qinling Orogen, reflecting the existence of large granitic batholiths in the shallow crust and intermediate to mafic residues in the mid/lower crust based on the geochemical signatures. Relatively low velocities are observed in the mid crust of Dabashan Orocline, probably representing shear zones and metasedimentary sequences. We suggest the crustal-scale bodies with high-velocity and high Poisson's ratio beneath the two domes and the western Qinling Orogen may represent mechanically strong rocks, which not only assist the formation of the major Dabashan Orocline during late Mesozoic intra-continental orogeny, but also impede the northeastward expansion of the Tibetan Plateau during Cenozoic era.

3.2 Introduction

The Qinling Orogen, a part of the central orogen in China, is bordered by the Dabie-Sulu orogen in the east and the Qilian-Kunlun orogen in the west (Fig. 3.1). The current tectonic framework of the Qinling Orogen is mainly shaped by the Triassic collision between the North China Craton and the Yangtze Craton [Ames *et al.* (1993); Li *et al.* (1993); Meng & Zhang (1999)], following a series of arc-continent and continent-continent collisions beforehand [Wu & Zheng (2013); Zhang *et al.* (2002); Zhang *et al.* (2001)]. After that, this orogen entered a period of intra-continental orogeny [Liu *et al.* (2005)], during which period, a series of foreland fold-thrust belts were developed in the northern and western margin of the Yangtze Craton, including the Dabashan, Hannan and Longmenshan belts [Burchfiel *et al.* (1995); Liu *et al.* (2005); Liu *et al.* (2015b); Meng & Zhang (2000); Yan *et al.* (2011)]. The intra-continental orogeny lasted possibly until the late Cretaceous [Liu *et al.* (2015a); Shi *et al.*

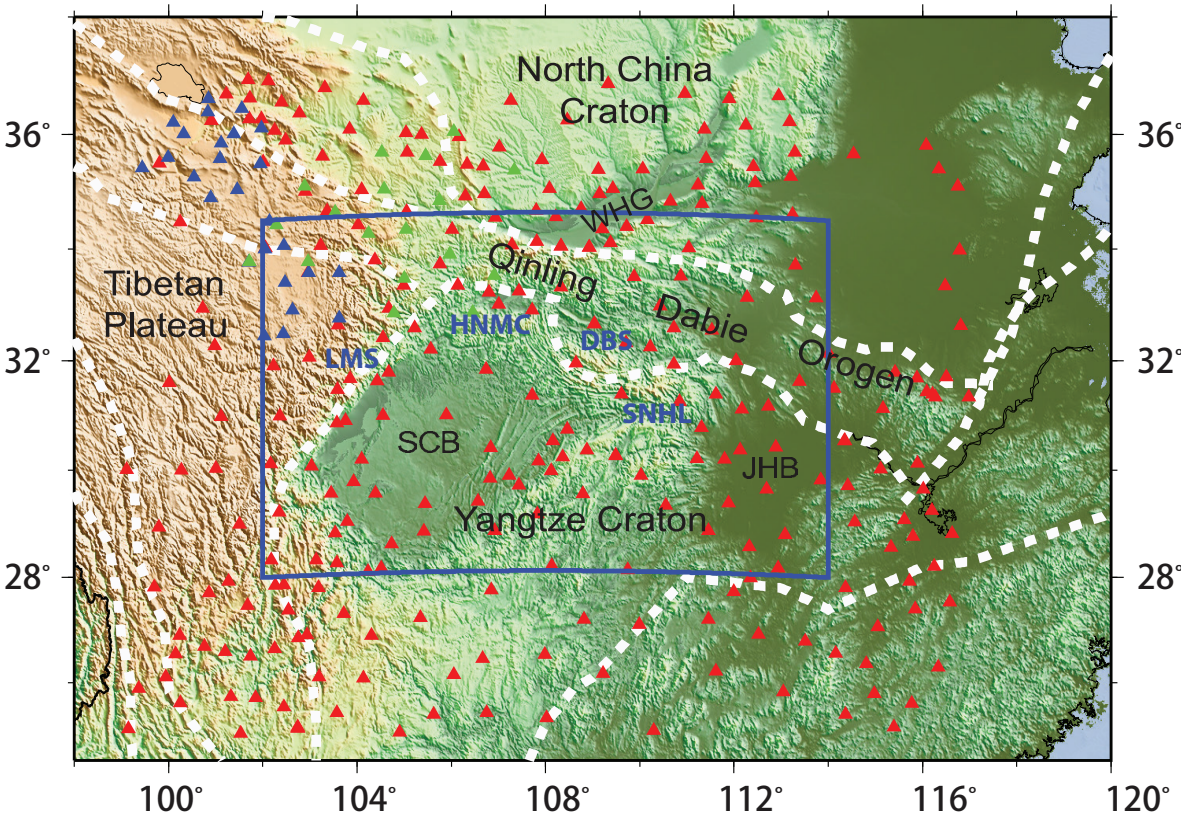

Figure 3.1: Tectonic units of the research area (outlined by the thick blue line) and its surroundings. Coloured triangles denote the seismic stations used in this study; Red: Chinese Provincial networks; Blue: Northeast Tibet Seismic Experiment (NETS); Green: A Seismic Collaborative Experiment in Northeastern Tibet (ASCENT). Thick dashed white lines delineate the main tectonic boundaries. Abbreviations: LMS-Longmenshan; HNMC-Hannan-Micang Dome; DBS-Dabashan Orocline; SNHL-Shennongjia-Huangling Domes; SCB-Sichuan Basin; JHB-Jianghan Basin; WHG-Weihe Graben.

(2012); Zhang *et al.* (2001)] when several local extensional basins were formed in the upper section of the orogen, representing the initiation of mountain collapse. In the Cenozoic era, the ongoing collision between the Indian and Eurasian plates and the subsequent uplift of the Tibetan Plateau has affected the uplift and exhumation of the neighbouring Qinling Orogen and the Yangtze Craton [Burchfiel *et al.* (2008); Clark & Royden (2000); Enkelmann *et al.* (2006); Hubbard & Shaw (2009)].

In spite of the intensive studies on the tectonic evolution of the Qinling orogenic belt from both geology [Liu *et al.* (2005); Liu *et al.* (2015a); Liu *et al.* (2015b); Meng & Zhang (2000); Zhang *et al.* (2001)] and geochemistry [Gao *et al.* (1992); Li & Sun (1996); Sun *et al.* (2002); Zhang *et al.* (2002)], how the tectonic features in the Qinling Orogen are shaped by the

collision between the North China Craton and Yangtze Craton and affected by the growth of the NE Tibetan Plateau in the Cenozoic still remain contentious. For example, the Dabashan Orocline is a prominent arc-shaped fold-thrust belt inside the orogenic conjunction. In the past few years, great efforts [Dong *et al.* (2013); Hu *et al.* (2012); Li *et al.* (2013); Liu *et al.* (2015a); Shi *et al.* (2012)] have been devoted to investigate the deformation process and the formation mechanism of this arcuate structure. Based on geological evidence, an indentation model has been proposed [Shi *et al.* (2012); Wang *et al.* (2003)], in which the Hann3-Dan-Micang (HNMC) and Shennong-Huangling (SNHL) Domes are suggested to act as strong indenters during the southward thrusts of the Qinling Orogen (Fig. 3.2). However, questions still remain about whether the crust beneath HNMC and SNHL Domes is mechanically strong and spatially large enough for the domes to be the indenters. On the other hand, the Tibetan Plateau is considered to grow outward through ductile channels in the mid/lower crust [Clark & Royden (2000); Royden *et al.* (2008); Royden *et al.* (1997)], and the ductile channels may intrude into the west Qinling Orogen and facilitate the uplift of the western Qinling Orogen [Enkelmann *et al.* (2006)]. However, the evidence for the intrusion of ductile channels into the western Qinling Orogen is still elusive.

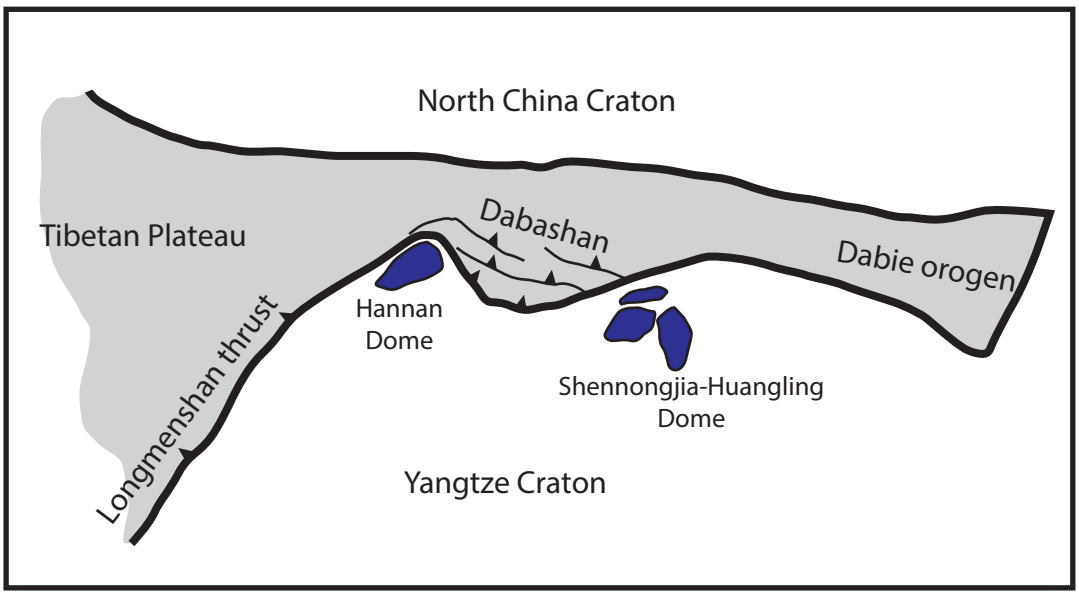

Figure 3.2: A sketch of the indentation model for the formation of the Dabashan Orocline (after Wang *et al.* (2003)).

Detailed images of crustal structures help to examine subsurface tectonic features, which

are results of deep dynamics. Previous geophysical explorations in the Qinling Orogen and its neighbouring region have gained important insights from the images of crustal structures. For example, the recognition of eclogitized mafic crust beneath the northern margin of Yangtze Craton [Dong *et al.* (2013)] is regarded as a possible driving force for the continuous intra-continental collision between the North China and South China Cratons during the Mesozoic. However, most early seismic studies either focus on linear seismic profiles [Dong *et al.* (2013); Yuan (1996); Zhang *et al.* (2009)] or cover only small parts of the orogenic belt, leaving most of the Qinling Orogen and its surrounding tectonic units not fully explored.

In this study, by collecting data from 321 broadband seismic stations from the Qinling Orogen and its adjacent Yangtze Craton and NE Tibetan Plateau, we construct a high-resolution 3-D crustal velocity model in the region using ambient noise tomography. By investigating the 3-D model, we mainly focus on addressing two scientific questions related to the interaction of the Qinling Orogen with the surroundings: 1) whether there is strong crust on both sides of the Dabashan Orocline to support the indentation model for its formation, and 2) if there is evidence for the intrusion of ductile mid/lower crustal channels into the western Qinling Orogen. The answers to the above two questions may not only help illuminate the tectonic interactions between the Qinling Orogen and its surroundings during the intra-continental orogeny, but also improve our understanding of the Cenozoic growth of Tibetan Plateau.

3.3 Ambient noise tomography

We collect ambient noise data from a total of 321 stations from the China Provincial Networks [Zheng *et al.* (2009)], the networks of Northeast Tibet Seismic Experiment (NETS) and a Seismic Collaborative Experiment in Northeastern Tibet (ASCENT) operating between 2007 and 2010. The distribution of stations is plotted in Fig. 3.1. We only use the vertical components of continuous seismic data to retrieve Rayleigh waves from ambient noise.

The processing procedures of ambient noise data are the same as those adopted in our earlier studies [Jiang *et al.* (2014); Yang *et al.* (2012)] following Bensen *et al.* (2007). First, instrument responses are removed from all the collected continuous ambient noise

data, and then all waveforms are band-pass filtered at 5-150 sec period. Both temporal and frequency normalisation is then applied to the filtered data. Afterwards, cross-correlations between all station-pairs are performed on a daily basis, which are stacked to form the final cross-correlations. In the end, the stacked cross-correlations are cut to obtain positive and negative components (Fig. 3.3) before the two components are stacked together to get the symmetric components. The method of automated frequency-time analysis (FTAN) [Bensen *et al.* (2007); Dziewonski *et al.* (1969); Levshin & Ritzwoller (2001)] is applied to the symmetric components to measure Rayleigh wave phase velocity dispersion curves at 8-50 sec periods.

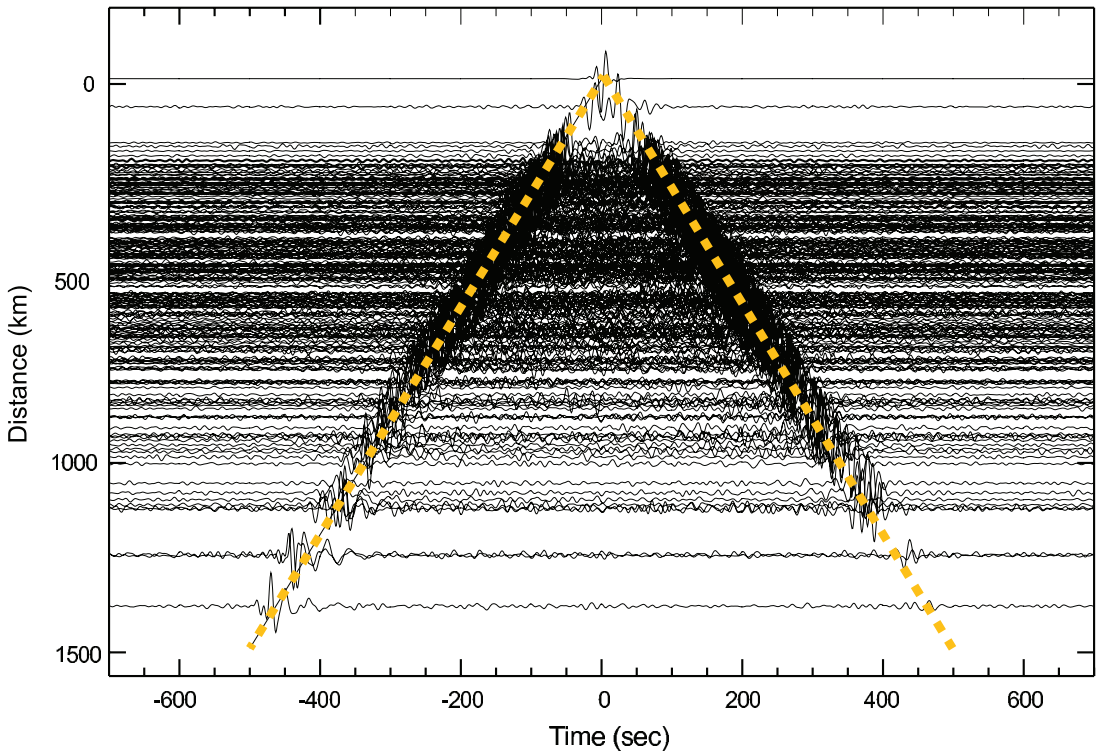

Figure 3.3: Examples of two-year ambient noise cross-correlations filtered at 10-50 s periods. The yellow dashed lines display a surface wave move-out of 3 km/s.

Quality control is performed on the measured phase velocity dispersion curves to remove bad measurements. Three criteria are adopted for the quality control: (1) the distance between each station-pair has to be longer than two wavelengths; (2) the signal-to-noise ratio (SNR), which is defined as the ratio between the maximum within a surface wave window defined by a group velocity of 2-4 km/s and the RMS of the trailing time series following

the surface wave time windows, must be greater than 15; (3) The misfits of the dispersion measurements must be less than 3 s during tomography. After the quality control, more than 30000 cross-correlations are retained for most of the periods (12-25 s). Although the number of paths decreases at periods longer than 30 s, there are still ∼9200 paths retained at 50 s. The decreasing of paths towards the long period end is mostly due to the criteria of minimum two wavelengths for the inter-station distances.

The selected phase velocity dispersion curves are then inverted for phase velocity maps on a $0.5^\circ \times 0.5^\circ$ grid using the well-established tomography method of Barmin *et al.* (2001). During the tomography, resolution is also estimated simultaneously by evaluating the individual rows of the resolution matrix for corresponding spatial nodes, following the method of Barmin *et al.* (2001) and Levshin *et al.* (2005). According to the resolution maps, the lateral resolution of most of our study region is ∼60-70 km. To better visualise the resolution, checkerboard tests are also performed. Two examples of resolution distributions and recovered checkerboard models with $1^\circ \times 1^\circ$ anomalies at 25 and 40 s periods are plotted in Fig. 3.4. It is clear that velocity anomalies are well recovered in most of our study region.

3.4 Phase velocity maps

The resulting phase velocity maps at 10, 20, 25 and 40 s periods are plotted in Fig. 3.5. The pronounced low velocities in the Tibetan Plateau through nearly all the periods are consistent with that seen in early ambient noise tomography models at this region [Jiang *et al.* (2014); Yang *et al.* (2012); Yang *et al.* (2010); Li *et al.* (2014)]. In the Yangtze Craton, the main tomographic features from this study are similar to those seen in Zhou *et al.* (2012). However, this study covers more stations in the regions north of $33^\circ N$, where the model of Zhou *et al.* (2012) loses resolution. In addition, our tomography reveals a series of interesting features which have not been imaged in detail and/or addressed in previous studies.

At short periods like 10 s, phase velocities are mainly affected by the upper crustal structures. At these periods, strong low velocities are observed beneath the Weihe Graben, the centre of Jianghan Basin and the Sichuan Basin. Interestingly, two localised areas in the

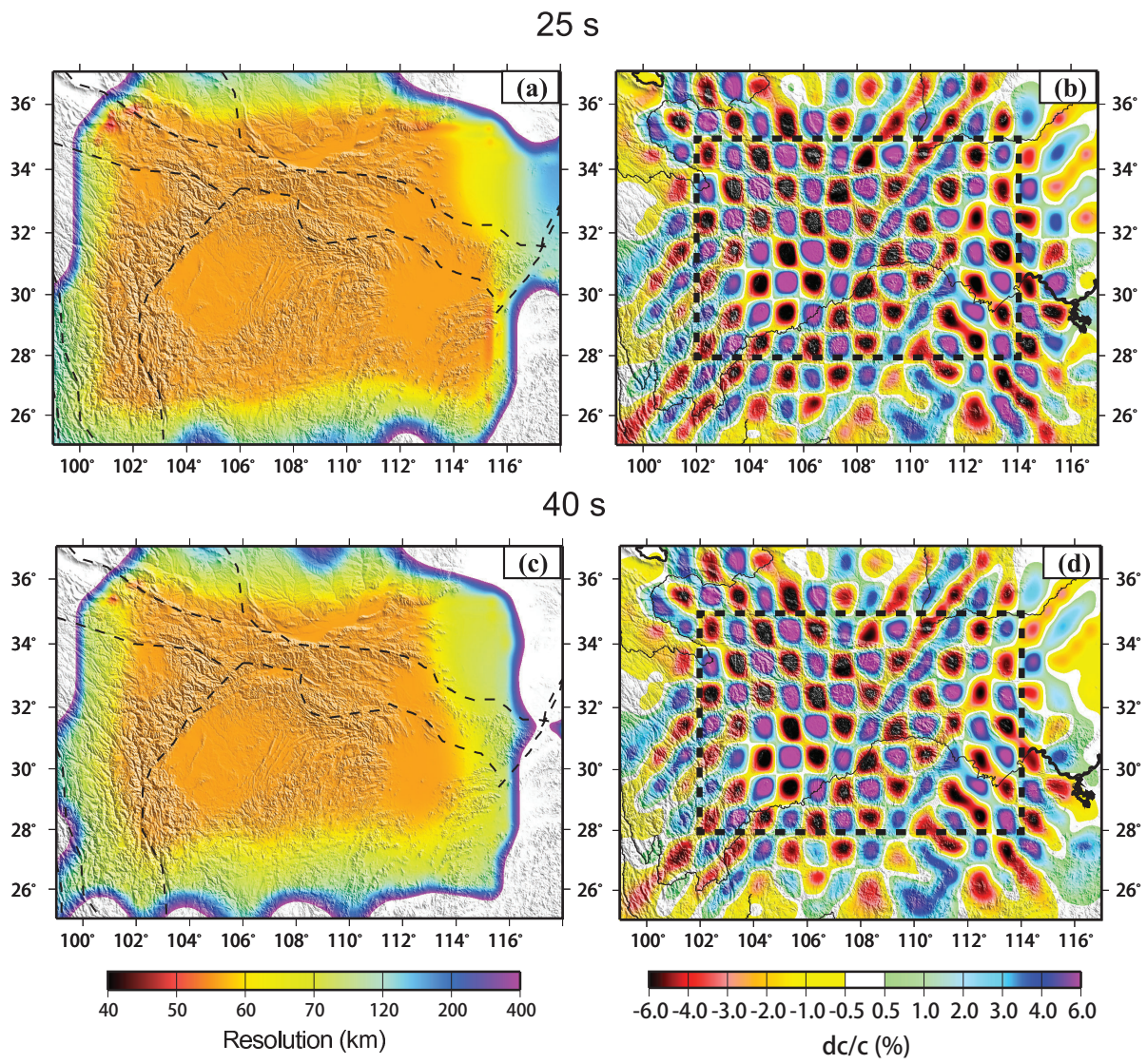

Figure 3.4: Resolution maps (a, c) and recovered checkerboard models (b, d) at 25 and 40 s periods. The black dashed lines in Fig. 3.4a and c delineate the main tectonic boundaries as that in Fig. 3.1. The thick black dashed squares in Fig. 3.4b and d outline the main research area of this study, where phase velocity maps are plotted in Fig. 3.5 and inverted Vsv maps in Fig. 3.7.

northern Sichuan Basin have lower velocities than elsewhere in the basin, coincident with the two depositional centres as shown by Richardson *et al.* (2008). The low velocities in the Sichuan Basin appear to extend further northeast into the Dabashan Orocline. This low velocity region in the Dabashan Orocline is sandwiched by two prominent high velocity bodies in the HNMC and SNHL Domes on both sides of the orocline. Relative higher velocities are observed in the segment of 106 °E-109 °E of the Qinling Orogen.

At intermediate periods of 20 and 25 s, phase velocities mainly reflect seismic structures

in the mid/lower crust. Low velocities are continuously observed beneath the Dabashan Orocline; while the Sichuan Basin starts to stand out as high velocities as the velocities reflect the cratonic basement. A noticeable feature shown at these periods is the relatively higher velocity in the regions to the east of the western boundary of the Jianghan Basin. This eastward increase of velocities is most likely attributed to the thinner crust in the east than in the west.

At long periods like 40 s, phase velocities mainly reflect the variations of the Moho depth in our study region. Nearly homogeneous high-velocities are observed beneath the Qinling Orogen and Yangtze Craton, while much lower velocities are seen in the NE Tibetan Plateau. This mostly reflects the decreasing of crustal thickness from the NE Tibetan Plateau to its surroundings with a sharp boundary clearly separating the very thick plateau crust with the rest.

3.5 Shear velocity inversion

Phase velocity maps provide us with integrated velocity structures of the crust because surface waves at individual periods are sensitive to a broad depth range. In order to investigate the structures at specific depths, we invert local phase velocity dispersion curves for depth-dependent shear velocities. We extract local dispersion curves at 8-50 sec periods from the inverted phase velocity maps. Three examples of local dispersion curves with their locations marked as coloured stars in Fig. 3.5c are plotted in Fig. 3.6a-c. We invert the extracted local dispersion curves for 1D Vs profiles using a Bayesian Monte-Carlo method developed by Shen *et al.* (2013). The detailed discussion of this method can be found in Shen *et al.* (2013), and we only briefly describe it here.

The model space is constructed from the surface to a depth of 150 km with two or three layers, including a sedimentary layer if the thickness of the sedimentary layer is larger than 2 km according to the Crust 2.0 model [Bassin *et al.* (2000)], a crystalline crustal layer and an upper mantle layer. The sedimentary layer is constrained by two parameters including the layer thickness and the average Vs. The vertical velocity variations in the crystalline crustal layer are represented by four B-spline coefficients and the crustal thickness is included as a

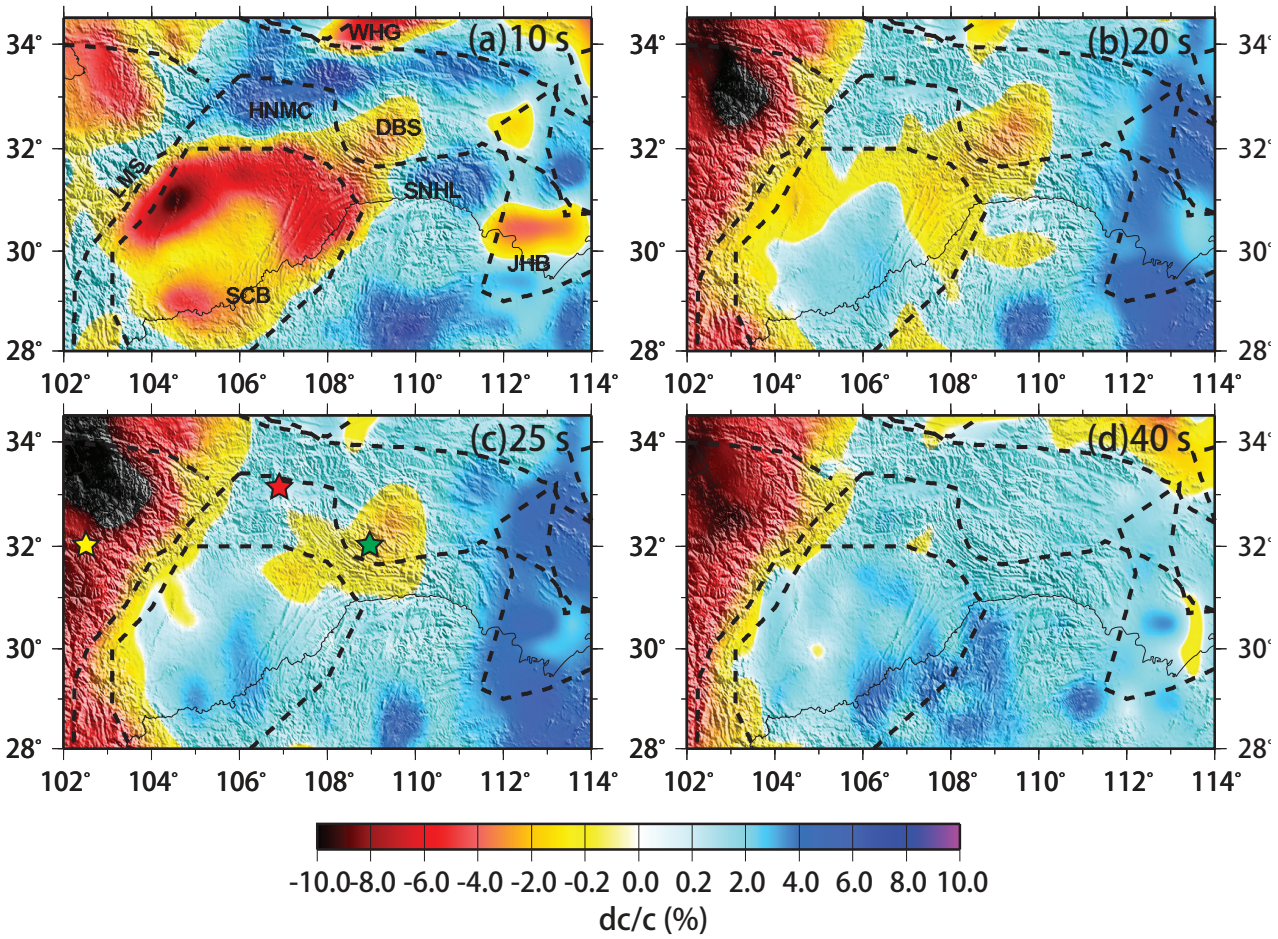

Figure 3.5: Rayleigh wave phase velocity maps at the periods of (a) 10 s, (b) 20 s, (c) 25 s and (d) 40 s, plotted as the percent perturbation relative to the average of each map. The colored stars in the velocity map of 25 s mark the locations of the three points referred in Fig. 3.6. Abbreviations: LMS-Longmenshan; HNMC-Hannan-Micang Dome; DBS-Dabashan Orocline; SNHL-Shennongjia-Huangling Domes; SCB-Sichuan Basin; JHB-Jianghan Basin; WHG-Weihe Graben.

parameter in the inversion. The velocities of the upper mantle from the Moho to 150 km depth are described by five B-spline coefficients. In the inversion, we only invert for Vs by scaling Vp and density to Vs. The Vp/Vs ratio in the sedimentary layer is set to 2.0 by taking a median value of the ratio for the Vs range of 1.0-2.5 km/s [Brocher (2005)]; while the ratio of Vp/Vs in crust and mantle are set to 1.73 as Poisson solids. Density is calculated based on the Vp value, which is converted directly from the Vs model according to the Vp/Vs ratio in each layer following the linear relation of $density = 0.541 + 0.3601 * Vp$ [Brocher (2005)] as suggested by Christensen & Mooney (1995). Moreover, attenuation effects on dispersion curves are corrected [Kanamori & Anderson (1977)] using Q values modified from

the PREM model [Dziewonski & Anderson (1981)] as Yang *et al.* (2012) and Jiang *et al.* (2014) did.

In the inversion, we take the Vs model and the Moho depth of Zhou *et al.* (2012) as our starting model for the regions roughly to the south of $33^\circ N$; while, for the remaining areas not covered by the model of Zhou *et al.* (2012), we use a Vs profile calculated by averaging that of the region south of $33^\circ N$, and the Moho depth for the region not covered by Zhou *et al.* (2012) is set to the same value as the point nearest to it. In this study, we sample the space within $\pm 20\%$ variations of the starting model. As demonstrated in our previous studies [Jiang *et al.* (2014)], the initial Vs model has insignificant effects on the final Vs results except the Moho depth. However, in this study, the Moho depth is allowed to vary in a 20% range from the starting model, which should be able to accommodate the real Moho depth of the region.

During the inversion, three prior constraints are taken when choosing acceptable models. (1) Vs in the crust is constrained to increase linearly in the first 5 km when a sedimentary layer is present, but is set to vary completely freely for the regions without sedimentary layers; (2) velocity contrasts across the sediment-basement interface and the Moho are both positive; (3) Vs in the mantle cannot exceed 4.9 km/s. After comprehensively sampling through model space based on the prior information, a posterior distribution of acceptable models is displayed by a series of 1D Vs profiles at each point on a $0.5^\circ \times 0.5^\circ$ grid. The mean of all the acceptable models for each geographic point is taken as the final Vs profile for that point and the standard deviation as the Vs uncertainties. The derived 1D Vs profiles at three points are presented in Fig. 3.6d-f. The local dispersion curves are well fitted by the predicted dispersion curves from the inverted model. All of these 1D Vs profiles are then assembled to form a 3-D Vs model.

3.6 The inverted 3-D Vs model

Four slices of the resulting 3-D model at the depths of 10, 18, 25 and 35 km are plotted in Fig. 3.7, and four transects along the profiles marked as solid grey lines in Fig. 3.7a are presented in Fig. 3.8.

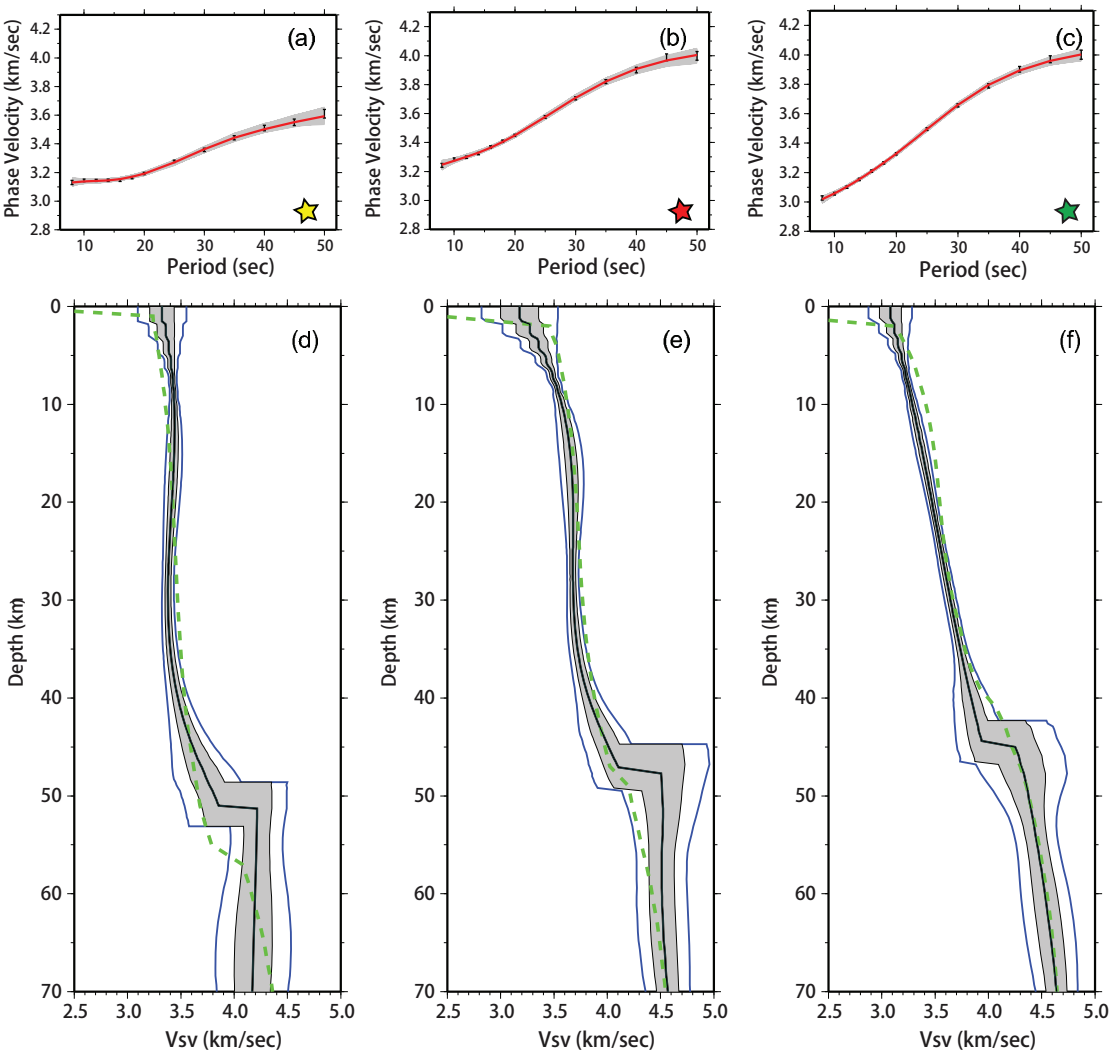

Figure 3.6: (a-c) The observed phase velocity dispersion curves at the three geographic points marked in Fig. 3.5. The grey lines represent the predicted dispersion curves from accepted Vs models during the inversion. (d-f) Inverted Vs profiles at correspondent points of Fig. 3.6a-c. The grey corridors represent one standard deviation around the mean produced from the Monte-Carlo inversion. The blue lines mark two standard deviations around the mean. The bold black lines are the mean of the resulting ensemble of acceptable models from the inversion. The green dashed line is the starting model. All depths are relative to the local surface. Note that each of the three layers (the sedimentary layer, the crust layer and the upper mantle layer) is further divided into many sub-layers, resulting in a discrete appearance of 1D model in the figures.

At the shallow depths like 10 km, low velocities are mainly seen in the Weihe Graben, the Dabashan Orocline, the centre of Jianghan Basin, and the west and SE corner of the Sichuan Basin, where two correspondent depositional centres are located [Richardson *et al.* (2008)]. The low velocities in these regions are mainly due to the presence of thick sedimentary layers.

The remaining areas, mostly orogenic belts, exhibit high velocities. The high velocities are mainly attributed to the presence of metamorphic and crystalline rocks. In particular, extensive high velocities are seen beneath both HNMC and SNHL Domes on the two sides of the Dabashan Orocline, with a lateral dimension of more than 200 km. Moreover, the high velocity body beneath the HNMC Dome seems to be connected with similar high velocities in the segment of 106 °E-109 °E of the Qinling Orogen. These high velocities are observed to extend to the mid/lower crust level, as clearly demonstrated in the cross-section C-C' of Fig. 3.8.

In the mid/lower crust such as depths of 18 and 25 km, strong low velocities are found beneath the NE Tibetan Plateau, which are delineated by a sharp velocity contrast to the east, geographically following the Longmenshan front. The clear velocity separations extend further north into the west Qinling Orogen, mainly around 105 °E-106 °E as shown in Fig. 3.7b-c. At these depths, the Sichuan Basin shows high velocities, as also illustrated by the velocity profiles of A-A' and D-D' in Fig. 3.8. The vertical profiles clearly display the uniformly distributed high velocities beneath the Sichuan Basin, increasing from ∼3.7 km/s at 20 km in the mid crust to more than 4.0 km/s in the lower crust. The velocities, however, become lower moving northward into the Dabashan and the adjacent Qinling Orogen. The low velocities beneath the Dabashan appear to be sandwiched by the two high velocity bodies seen in the cross-sections (C-C' of Fig. 3.8).

At 35 km depth, a clear trend of velocity increasing from west to east is exhibited. The low velocities in the NE Tibetan Plateau and the segment of Qinling Orogen to the west of 104 °E still represent velocities of the mid crust; while the Qinling Orogen and the western Yangtze Craton mostly reveal the seismic velocities of the lower crust. Higher velocities are observed beneath the Sichuan Basin, probably reflecting the cold cratonic basement. In the region roughly east of longitude 111 °E, the average crustal thickness is 32 km. The velocity higher than 4.4 km/s at 35 km reflects uppermost mantle velocity for that region.

Since the main aim of this study is to address questions on regional geology and tectonic evolution based on our derived velocity model, it is important to ensure the reliability of the velocity model. On top of the fact that synthetic tests demonstrate a good recovery of a checkerboard model with a general resolution of 60-70 km in the research area, we find that

the major velocity features, based on which further interpretations are made in the following section, are also consistent with the models from previous studies. For example, the pattern of relatively lower velocities beneath the Dabashan Orocline sandwiched by higher velocities beneath the HNMC and SNHL Domes at the shallow and middle crust are also observed in the models of Zhou *et al.* (2012), Bao *et al.* (2013) and Bao *et al.* (2015). Connected high velocities beneath the western edge of the Sichuan basin, the HNMC Dome and Qinling Orogen are also displayed in the crustal model of Bao *et al.* (2013). However, interpretations of these important features, which help to shed new insights into regional tectonics, are not addressed in these studies. In this study, the concentration on the crustal structure in the conjunction of Qinling Orogen, Yangtze Craton and Tibetan Plateau illustrates the above features more clearly. When integrated with the interpretations from geological, geochemical and other geophysical studies in the region, we demonstrate that significant information on local geology can be revealed.

3.7 Discussion

3.7.1 Geological correlations with the velocity model

Our 3-D velocity model demonstrates distinguishable variations of crustal thickness from east to west: a thin crust in the east, an intermediate crust in the middle and a thick crust in the west.

Previous geophysical observations [Zhang *et al.* (2009); Zhou *et al.* (2012)] demonstrate that the crustal structures in the Jianghan Basin and the areas to the east of it exhibit signatures of extension. In this study, this feature is best shown by the abrupt variations of crustal thickness from the vertical velocity profile of C-C' in Fig. 3.8, jumping from a crust with a thickness of ∼45 km in the west to a much thinned crust with an average thickness of ∼34 km. The Jianghan Basin, characterised by low velocities in the shallow crust, is a Cretaceous to Early Tertiary extensional basin [Liu *et al.* (2005)]. This is consistent with our observation of a relatively thin high-velocity layer (> 4.0 km/s) in the deep crust of the basin (C-C' in Fig. 3.8), and also the seismic reflection result of Zhang *et al.* (2009).

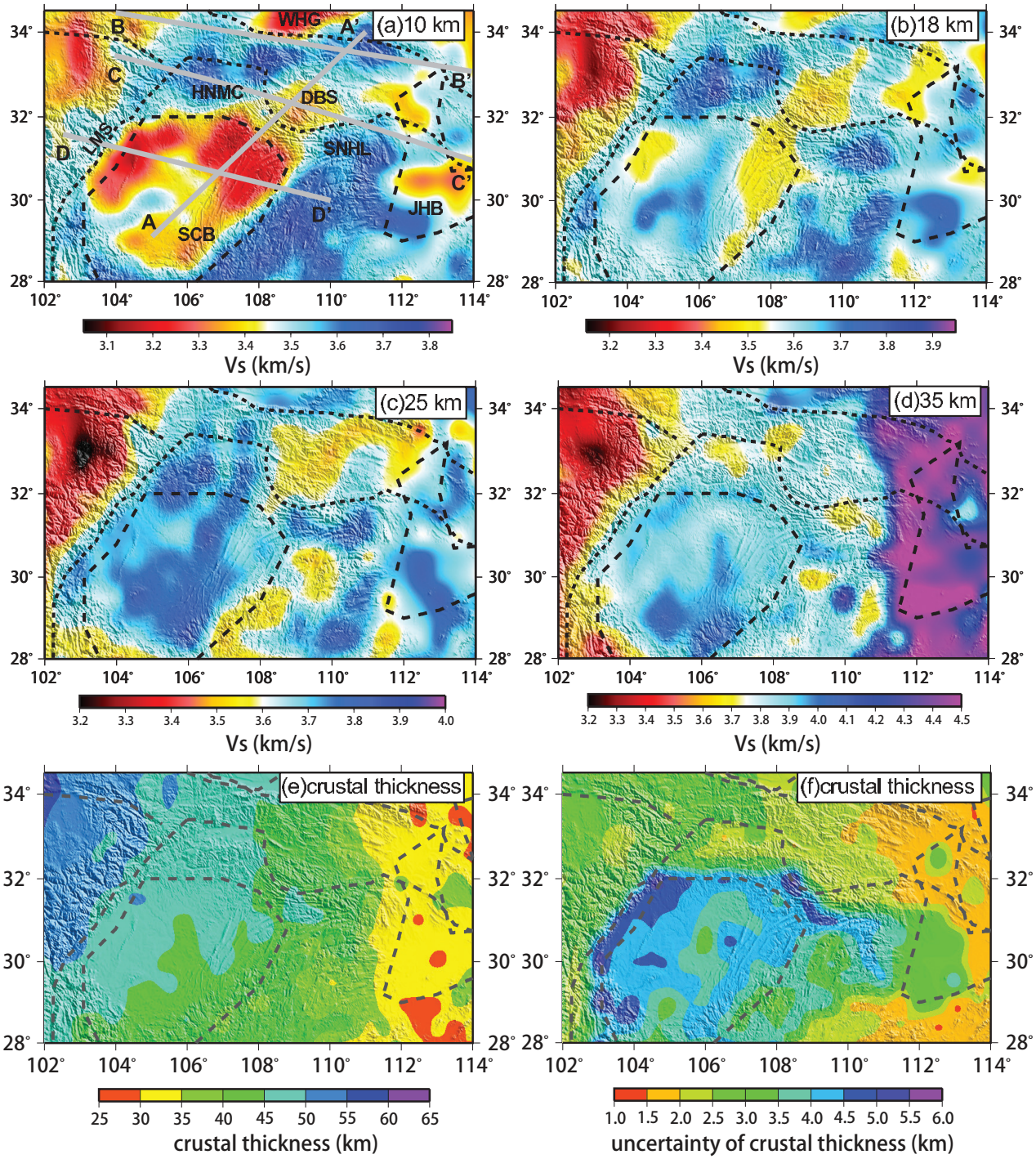

Figure 3.7: (a-d) Vsv maps at the depths of (a) 10, (b) 18, (c) 25 and (d) 35 km respectively. All depths are relative to sea level. The solid grey lines in Fig. 3.7a outline the locations of the profiles of four transects shown in Fig. 3.8. Abbreviations: LMS-Longmenshan; HNMC-Hannan-Micang Dome; DBS-Dabashan Orocline; SNHL-Shennongjia-Huangling Domes; SCB-Sichuan Basin; JHB-Jianghan Basin; WHG-Weihe Graben. (e-f) Maps of estimated crustal thickness from the inversion and its associated uncertainties.

Meanwhile, the variations of crustal structures roughly following the longitude of 111 $^{\circ}E$ are coincident with the North and South gravity lineament (NSGL) [Ma (1989)].

In the central part of our research area, the average crustal thickness is ∼45 km, which is close to the thickness of typical platform crust [Christensen & Mooney (1995)]. Different from the extensional environment in the east during the late-Mesozoic, the central region is divided into two deformational regimes. On the margins of the Sichuan Basin, a series of foreland fold-thrust belts is developed, which include the Dabashan and Hannan belts in the north, and Longmenshan belt in the west [Burchfiel *et al.* (1995); Liu *et al.* (2005); Liu *et al.* (2015b); Meng & Zhang (2000); Yan *et al.* (2011)], indicating a continuous crustal shortening following the Triassic collision between the North China Craton and Yangtze Craton. The Sichuan Basin, which is probably the core of the Yangtze Craton, undergoes little internal deformation [Burchfiel *et al.* (1995)]. The two depositional centres in the Sichuan Basin where extreme low velocities are imaged in the shallow crust correspond to the Longmenshan and Dabashan foreland basins respectively.

Except for the Dabashan Orocline, most orogenic belts display high velocities due to the dominance of crystalline volcanic and/or metamorphic rocks at these belts. This is particularly evident beneath the HNMC and SNHL Domes. On the surface of the HNMC Dome, one of the largest intrusive complexes in the Yangtze Craton, termed Hannan-Beidian complex [Gao *et al.* (1990); Zhou *et al.* (2002)], is exposed. The complex is suggested to have been formed on the northern margin of the Yangtze Craton during the accretion and rifting of the Rodinia supercontinent, although its detailed origin is still controversial [Gao *et al.* (1990); Li *et al.* (2003); Li *et al.* (1999); Zhou *et al.* (2002)]. At the SNHL Dome, Archean basement and associated intrusive and metamorphic rocks are exposed, with the widely exposed Kongling complex representing the oldest rocks in the Yangtze Craton [Gao *et al.* (1999); Qiu *et al.* (2000)]. The intrusive complexes in the region include mafic gabbro, tonalite-trondhjemite-granodiorite (TTG) rocks and felsic granites. The imaged high velocities in the shallow and mid crust beneath the two domes probably represent similar rock combinations to those exposed on the surface.

Shear velocities of rocks not just depend on rock types but also on other physical parameters of temperature, pressure. Therefore, shear velocities cannot be straightforwardly linked

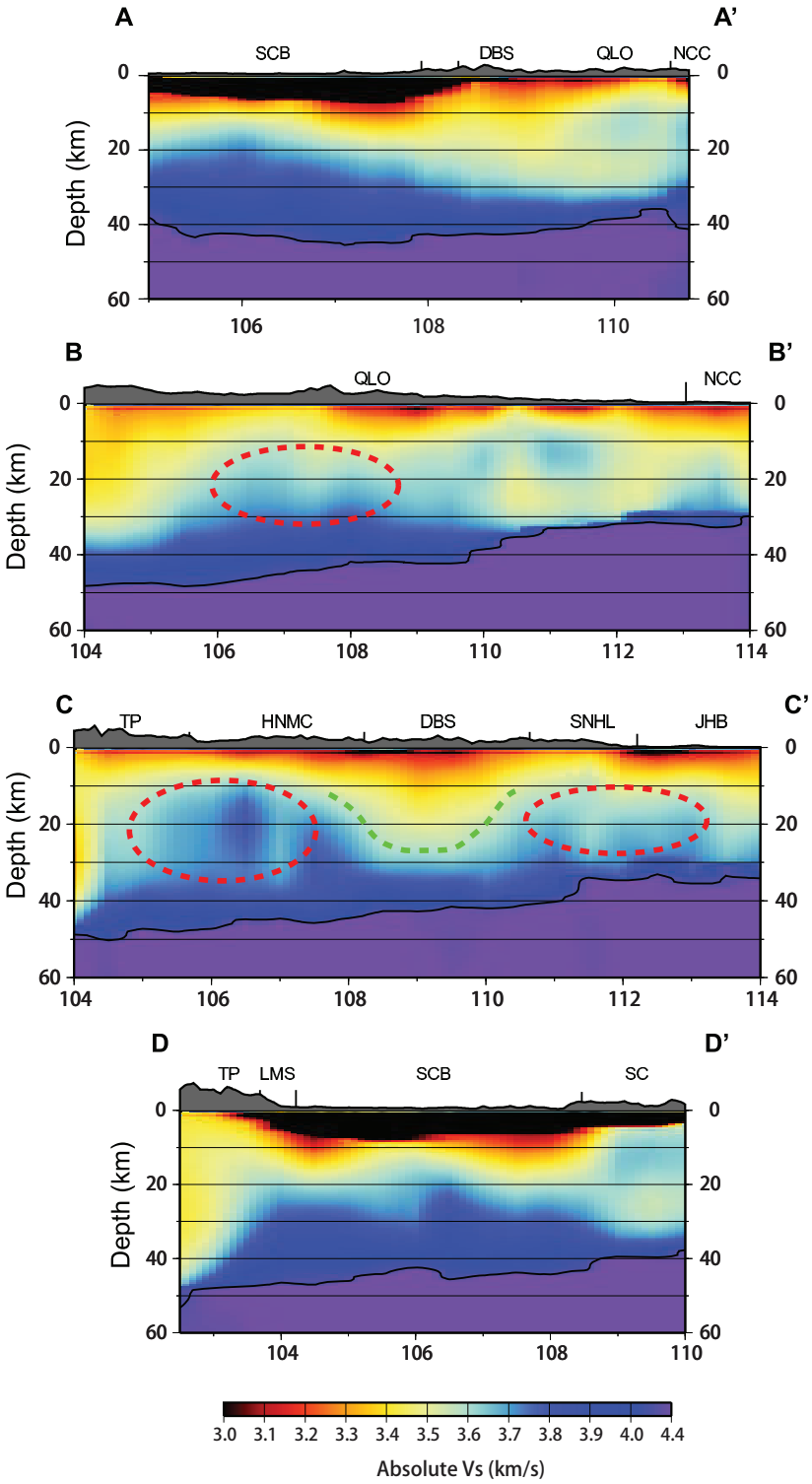

Figure 3.8: Transects of the Vs model plotted as absolute velocities along the four lines marked in Fig. 3.7a. All depths are relative to sea-level. The red dashed circle in B-B' outlines the elevated high velocities beneath the segment of 106°-109° of the Qinling Orogen. The red dashed circles in C-C' approximately outline the two similar high-velocity bodies beneath HNMC and SNHL; while the green dashed curve outlines the narrow channels of low velocities beneath the Dabashan Orocline. Abbreviations: SCB-Sichuan Basin; DBS-Dabashan Orocline; QLO-Qinling Orogen; NCC-North China Craton; JHB-Jianghan Basin; TP-Tibetan Plateau; HNMC-Hannan-Micang Dome; SNHL-Shennongjia-Huangling Domes.

to rock composition. However, the situation is different for rocks' Poisson's ratio. Because temperature and pressure have little effects on the Poisson's ratio, the value is regarded as a good indicator for bulk composition in the crust as suggested by laboratory studies [Christensen (1996)]. Thus, to indirectly relate our velocity model with rock compositions, we assemble all available Poisson's ratios of the crust in our research area from a series of receiver function studies [Huang *et al.* (2014); Pan & Niu (2011); Wang *et al.* (2010)] and plot them in Fig. 3.9a. The associated uncertainties are plotted in Fig. 3.9b for comparisons of the data reliabilities. As seen from the figure (Fig. 3.9a), the Poisson's ratio averages 0.26-0.27 in the Yangtze Craton, which is close to the global average of the continental crust [Christensen & Mooney (1995)]. Meanwhile, the three measurements from the Dabashan Orocline also display similar values as the Yangtze Craton, suggesting its basement has an affinity with the Yangtze Craton. This is consistent with our velocity model that the lower crust beneath the Dabashan Orocline and that beneath the Sichuan Basin have similar velocities. The Poisson's ratios for the crust in the HNMC and SNHL Domes are relatively higher with one station in the HNMC reaching as high as $\sim$0.29. As the surface exposures in the two domes are dominated by granitic intrusion, which has a Poisson's ratio of $\sim$0.24 [Tarkov & Vavakin (1982)], the mid/lower crust must contain considerable amount of mafic composition to compensate for the high Poisson's ratio as suggested by studies conducted in other regions [Pan & Niu (2011); Zandt & Ammon (1995)]. At the same conditions of temperature and pressure, mafic rocks are usually stronger in rheology compared to felsic [Wilks & Carter (1990)] and sedimentary rocks. Thus, the high velocities beneath the HNMC and SNHL Domes probably reflect crustal rocks with high strength.

Besides the high velocities beneath the HNMC and SNHL Domes, similar high velocities are observed in the shallow and mid crust of Qinling orogen, especially between the segments of $106\,^{\circ}E$-$109\,^{\circ}E$. On the surface of the Qinling orogen, Triassic granites are widely outcropped and are regarded as direct responses of the Triassic collision between the North China and Yangtze Craton [Dong *et al.* (2012); Ping *et al.* (2013); Qin *et al.* (2009); Sun *et al.* (2002)]. The high velocities at depths shallower than 10 km are probably the results of the crystallised batholiths of such granites. The measurements of Poisson's ratio in the region are either from the southern or the northern edges of the Qinling Orogen, and the

values from the southern edge are a bit lower than those in the HNMC and SNHL Domes. However, the geochemical signatures of the deep crust brought up by the Triassic granites indicate the southern Qinling Orogen may share similar basement rocks and tectonic evolutions as most of the Yangtze Craton before its rifting in early Palaeozoic [Dong *et al.* (2011); Ping *et al.* (2013); Zhang *et al.* (2001)]. Thus, the high velocities in the mid crust beneath the segment of 106 °E-109 °E in the Qinling Orogen may represent similar crustal compositions as those beneath the HNMC Dome though more work needs to be done to verify this conclusion. The relative low velocities in the mid crust of the Dabashan Orocline most likely result from the existence of shear zones, sedimentary and meta-sedimentary sequences as will be further discussed in section 3.7.2.

The crustal velocity model of this study indicates the crust of the Qinling Orogen and its adjacent regions may be mechanically strong. The strong crust was most likely formed either during the late stage of the collision or during the Neo-Proterozoic as we discuss in the preceding paragraphs. During the subsequent post-collisional history, the strong crust had significant impacts on the deformation of the crust, especially on the formation of the Dabashan Orocline during the late Mesozoic intra-continental orogeny and the Cenozoic growth of the Tibetan Plateau, as discussed in the following two sections.

3.7.2 Formation of the Dabashan Orocline

The Dabashan Orocline is a prominent feature in the conjunction of Qinling Orogen, Yangtze Craton and the NE Tibetan Plateau. The most popular model to explain its formation is the indentation model, in which HNMC and SNHL Domes stand as strong indenters during the southward thrusts of the Qinling Orogen (Fig. 3.2).

Our 3-D Vs model provides direct evidence to support this model by revealing detailed crustal structures of the region. Based on both the velocity maps at different depths (Fig. 3.7) and the transects crossing the orocline (Fig. 3.8), it is clear that significant high velocities are seen in the mid/lower crust of the northern margin of the Yangtze Craton, right beneath the HNMC Dome to the west of the orogen and the SNHL Dome to the east. The high velocity bodies appear to extend to the upper crust with some local areas even reaching

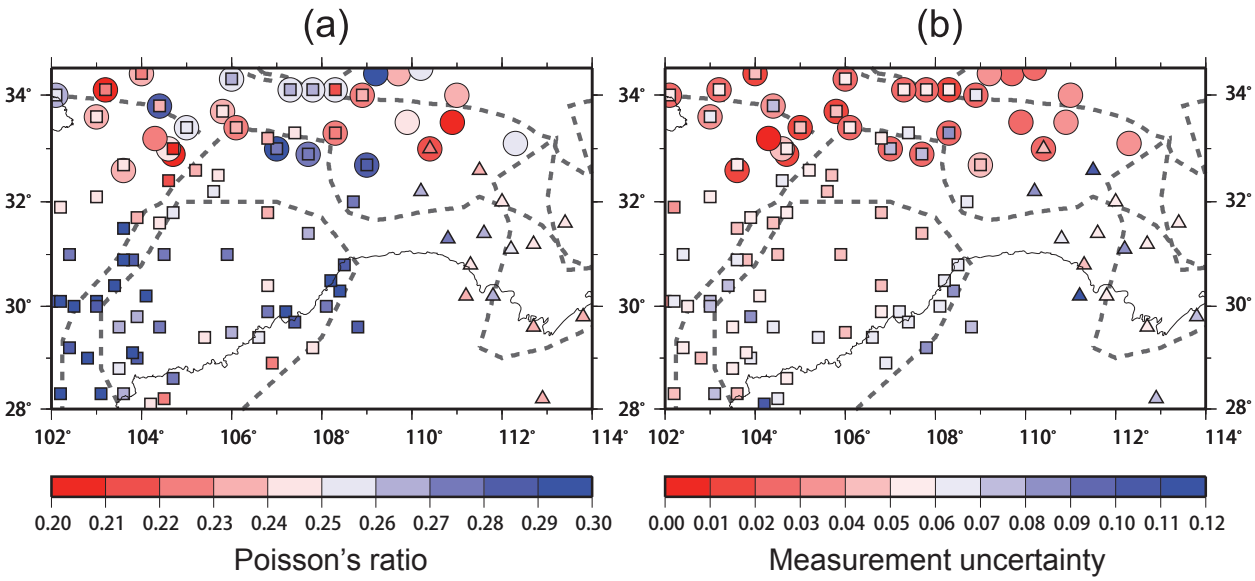

Figure 3.9: Measurements of Poisson's ratio in the research area from receiver functions by previous studies (a) and the associated uncertainties of their measurements (b). Different symbols represent the results from different studies: Circles: Pan & Niu (2011); Triangles: Huang *et al.* (2014); Squares: Wang *et al.* (2010). The points where two symbols are superimposed represent the place where Poisson's ratio measurements are from two different studies.

a depth shallower than 10 km (Fig. 3.8). Because our velocity model is mostly based on surface waves with periods longer than 8 sec, the constraints on the uppermost crust are weak. However, the surface exposures of granitoids, mafic intrusives and Archean basement rocks around the HNMC and SNHL Domes as discussed in the preceding section indicate that the high velocities probably have extended to quite shallow depths or even to the surface. The relatively low velocities observed right beneath the Dabashan Orocline probably represent the metamorphosed sedimentary sequences, which were once parts of a passive continental marginal basin along the northern Yangtze block before the North China and South China collision [Zhang *et al.* (2001)]. This marginal basin is disrupted by later foreland sedimentation during the initial convergence between the North China Craton and Yangtze Craton, and is further involved in the deformation during collisional and intra-continental crustal shortening [Liu *et al.* (2015a)].

As discussed in the last section, the high velocities and high Poisson's ratio of the two domes probably reflect felsic upper crust with more mafic deep crust, which are likely mechanically strong compared to the sedimentary and meta-sedimentary sequences in the Dabashan

Orocline. Therefore, the two mechanically strong domes may stand as direct obstacles during the thrusting of the Dabashan Orogeny, forcing the weaker materials to move along the narrow channels between the two domed bodies (outlined by the green dashed line in C-C' of Fig. 3.8). The shortening of the Dabashan Orogen in the narrow channel is mostly via the development of shear zones and detachments at different depths as suggested in a previous geological study [Shi *et al.* (2012)]. The strong shortening also leads to thick foreland sedimentation in the front of the orogen [Richardson *et al.* (2008)], which are then buried and involved in the later thrusting movement [Dong *et al.* (2013)]. The dramatic low velocities (<3.0 km/s) observed in the shallow crust beneath the current southern margin of the Dabashan represent the foreland sedimentation resulting from the latest thrusting of the orogen [Liu *et al.* (2015a)].

However, one question still remains, which is whether the crustal-scale domes of HNMC and SNHL were already elevated to shallow crustal depths during the actual time of thrusting. Thermo-chronology results indicate that the samples from current surface exposures at the two domes were situated at a depth with temperature of ∼200 °C in the late Jurassic time [Xu *et al.* (2010)]. If we consider a thermal gradient of 20-30 °C/km during the Jurassic, the temperature of ∼200 °C probably suggests they were already situated in the upper crust at that time. The strong crustal shortening during the intra-continental orogeny may further assist the fast exhumation of the intrusive and basement rocks from the shallow crust to the surface. This is demonstrated by the rapid pre-late Cretaceous exhumation rate recorded at HNMC Dome [Tian *et al.* (2012)]. Furthermore, the granitoids of the Huangling dome had already been the provenance of the late Cretaceous strata in the Jianghan Basin [Shen *et al.* (2012)], suggesting parts of the Huangling dome were exposed at the surface before the late Cretaceous. Thus, our seismic observations along with the geological exhumation history and the surface structural interpretations suggest that the HNMC and SNHL Domes in the northern margin of the Yangtze Craton played the role of indenters to assist the formation of the Dabashan Orocline.

3.7.3 Implication for the growth of the Tibetan Plateau

Understanding how the enormous Tibetan Plateau forms and grows is one of the hottest topics in geosciences today. One of the most popular models for its growth mechanism is the channel flow model [Clark & Royden (2000); Royden *et al.* (2008); Royden *et al.* (1997)], in which a possible ductile and low viscosity layer exists in the mid/lower crust, and is capable of flowing outward under the push of the northward subducting Indian plate. According to the numerical modelling of Clark & Royden (2000), crustal flows from the central plateau possibly separate into two branches at the eastern margin: one flowing northeastward to the Qinling and eastern Qilian Orogens and the other turning southeastward to the Yunnan region.

A ductile and low viscosity layer in the mid/lower crust is typically the result of high temperature and/or the presence of fluids, such as water or partial melt, which also leads to seismic low velocities. Thus, seismic features of low velocity zones (LVZs) in the mid/lower crust could be a good indicator of a mid/lower crustal low-viscosity channel. In the past decade, such LVZs have been imaged widely across most of the Tibetan Plateau [Yang *et al.* (2012); Yang *et al.* (2010)] and also in the southeast margin of the Chuandian block [Liu *et al.* (2014); Yao *et al.* (2008); Yao *et al.* (2010)]. Combined with other geophysical features of LVZs, such as high conductivity [Bai *et al.* (2010); Le Pape *et al.* (2012); Unsworth *et al.* (2004); Wei *et al.* (2001)] and significant radial anisotropy [Shapiro *et al.* (2004); Xie *et al.* (2013)], LVZs are usually regarded as direct evidence for the channel flow model. Our recent study [Jiang *et al.* (2014)] demonstrates that, in the NE Tibetan Plateau, LVZs are imaged to extend northward to the east Kunlun and western Qinling Orogen over ∼100 km across the Kunlun Fault in the segment of $98\,^{\circ}E - 104\,^{\circ}E$, and no LVZs are observed in the central part of the Qinling Orogen, to the east beyond $104\,^{\circ}E$. The 3-D Vs model of this study provides a possible explanation for the distribution of LVZs in the NE Tibetan Plateau. Crustal-scale high velocity anomalies combined with high Poisson's ratio observed beneath the Sichuan Basin, the HNMC Dome and the central segment of the Qinling Orogen right north of the HNMC dome, most likely represent mafic and mechanically strong crust, which may act as allied strong obstacles to inhibit the eastward movement of the channelized crustal flow from

the plateau. The distribution of the LVZs in the NE Tibetan Plateau suggests the pattern of the crustal flows is strongly affected by the crustal structures of neighboring blocks.

3.8 Conclusion

We construct a 3-D Vs model with a lateral resolution of 60-70 km in the Qinling Orogen and its conjunction area based on the analysis of continuous ambient noise data collected from 321 stations. Strong heterogeneities are observed in the Qinling Orogen and the northern margin of the Yangtze Craton. In particular, crustal scale high-velocity bodies are seen beneath the HNMC and SNHL Domes, probably representing intrusive complexes and associated basement rocks that have been uplifted as results of initial intrusion and later strong crustal shortening. The two dome-like rigid structures are situated right on the two sides of the Dabashan Orogen, probably acting as indenters during the southward thrusting of the orogen and leading to the formation of a geometrical arc-shaped Dabashan Orocline. The sediments in the corresponding Dabashan foreland are buried and may further assist the migration of the orocline at a later stage via the development of shear zones and detachment faults. Extensive high velocities are observed in the segment of $106\,^{\circ}E$-$108\,^{\circ}E$ of the Qinling Orogen, reflecting the connected batholiths of the Triassic granites in the shallow crust and possible mafic materials in the mid/deep crust. This high-velocity body together with similar structures beneath the HNMC Dome and the rigid mid/lower crust of the Sichuan Basin may impede the channelized mid/lower crustal flow from the eastern Tibetan Plateau.

4

Complex layered deep-crustal deformation in the NE Tibetan Plateau and surrounding orogenic belts inferred from ambient noise tomography

4.1 Abstract

Orogenic belts and neighboring regions are often characterised by features of strong deformation, resulting from complex geodynamic processes such as plate subduction and continent-continent collision. Seismic anisotropy provides important insights into the deformation, thus contributing to a better understanding of dynamic processes inside the Earth. In this

study, we employ the eikonal tomography method of Lin *et al.* (2009) to investigate the azimuthal anisotropy in the NE Tibetan Plateau and its adjacent orogenic belts, including the Longmenshan and Qinling Orogens. Significant variations of anisotropic features with period are imaged beneath most of the region, indicating strong anisotropic layering at depth. However, the different orientation of fast axes in these regions relative to their orogenic trends suggests both vertically and laterally distinct deformation. In the Qinling area, orogen-parallel (E-W) fast directions in the upper/mid crust and orogen-perpendicular (N-S) fast directions in the deep crust are consistent with those from typical subduction related orogens. In the NE Tibetan Plateau and Longmenshan region, however, the anisotropic pattern is totally reversed, likely related to different dynamic processes. The upper crust in the region is dominated by E-W oriented fast directions, which are possibly related to the plateau's extension and thinning, whereas the mid/lower crust displays strongly NW-SE directed anisotropy, which is further categorised into two regions regarding origin: the region beneath most of the plateau may represent a separate channel of crustal flow; while the other region, located mainly beneath the Longmenshan, is likely caused by a combined effect of horizontal shortening and vertical ductile deformation. The seismic anisotropy from this study thus demonstrates distinct styles of mountain-building processes in and around the NE Tibetan Plateau.

4.2 Introduction

Seismic anisotropy is an important indicator of past and recent tectonic history due to its close associations with deformation [Karato *et al.* (2008); Mainprice (2007); Savage (1999); Silver (1996)]. In the uppermost crust, seismic anisotropy is usually attributed to shape preferred orientation (SPO), such as the alignment of cracks [Crampin (1984)], foliations and faults. In contrast, anisotropy in the mid/lower crust and upper mantle is thought mainly to be caused by lattice preferred orientation (LPO) of anisotropic minerals [Karato *et al.* (2008); Mainprice (2007)]. The dominant anisotropic minerals include amphibole [Tatham *et al.* (2008)] and mica [Mahan (2006); Meltzer & Christensen (2001); Shapiro *et al.* (2004)] in the mid/lower crust, and olivine [Nicolas & Christensen (1987)] in the upper

mantle. Because LPO most likely originates from deformation processes, seismic anisotropy of the upper mantle is closely associated with mantle flow [Zhang & Karato (1995)].

In the past decade, global scale anisotropic models have been constructed which demonstrate the existence of distinct anisotropic layering in the upper mantle [Ekstrom & Dziewonski (1998); Gung *et al.* (2003); Marone & Romanowicz (2007)]. In particular, two layers of different anisotropy have been observed beneath cratonic regions. One such layer occurs in the lithosphere and has been predominantly regarded as a fossil of past deformation. The second layer occurs in the asthenosphere and is generally believed to reflect present-day mantle flow. Consequently, the anisotropy in the asthenosphere is usually suggested to be linked to present day absolute-plate motion (APM) [Gung *et al.* (2003); Marone & Romanowicz (2007)]. Models from these global seismic studies provide the first-order image of anisotropic layering in the upper mantle. Thanks to the availability of dense regional seismic arrays in recent years, and particularly the innovation of ambient noise tomography in the past decade [Lin *et al.* (2009); Moschetti *et al.* (2010); Shapiro *et al.* (2005); Yang (2014)], increasingly fine-scale and shallow (crustal-level) structures can now be characterised. The characterisation of fine-scale anisotropic structures has provided critical constraints on the operation of fundamental dynamic processes in the crust such as crustal magmatic intrusion [Jaxybulatov *et al.* (2014)], crustal-scale extension [Moschetti *et al.* (2010); Shapiro *et al.* (2004)] and mechanisms of orogeny [Huang *et al.* (2015)].

Many large orogenic belts, such as the European Alps [Fry *et al.* (2010)] and the Taiwan orogen [Huang *et al.* (2015)] typically exhibit two-layered deformation fabrics. In these regions, orogen-perpendicular anisotropy in the deep crust and uppermost mantle has been linked with subduction-induced shearing, and orogen-parallel deformation fabrics in the shallow crust have been associated with either collision-related SPO [Huang *et al.* (2015)] or gravitational collapse of the orogen [Fry *et al.* (2010)]. Therefore, imaging anisotropic features in orogenic belts helps to understand mountain-building processes.

A lot of attention has been focused on characterizing anisotropic structures in the Tibetan Plateau [Gao & Liu (2009); Huang *et al.* (2000); Lev *et al.* (2006); Liu *et al.* (2015c); McNamara *et al.* (1994); Ozacar & Zandt (2004); Pandey *et al.* (2015); Sandvol *et al.* (1997); Yao *et al.* (2010); Yu *et al.* (1995); Huang *et al.* (2010); Leon Soto *et al.* (2012);

Sol *et al.* (2007); Schulte-Pelkum *et al.* (2005)] as the plateau has been experiencing strong deformation related to its rapid growth due to the Indian-Eurasian continental collision [Yin & Harrison (2000)]. A number of these studies have concentrated either on the central [Huang *et al.* (2000);McNamara *et al.* (1994); Ozacar & Zandt (2004);], southern [Sandvol *et al.* (1997); Schulte-Pelkum *et al.* (2005)] or SE Tibetan Plateau [Lev *et al.* (2006);Yao *et al.* (2010); Sol *et al.* (2007)]. Seismic anisotropy in the crust of the NE Tibetan Plateau remains less known. In addition, the NE Tibetan Plateau is bordered by several orogenic belts. The Longmenshan to the east has the steepest topography gradient in the plateau, as the result of the plateau's eastward expansion [Hubbard & Shaw (2009)]. To the northeast, the Qinling Orogen is assumed to facilitate the extrusion of the plateau [Enkelmann *et al.* (2006)]. How these orogens are formed and relate to the growth of the Tibetan Plateau still remains enigmatic. Seismic anisotropy can provide valuable insights into the deep crustal deformation in the NE Tibetan Plateau and its adjacent areas.

In this study, we investigate azimuthal anisotropy in the same region as Chapter 3, building on previous efforts of characterising the isotropic velocity in the conjunction area of Tibetan Plateau, Qinling Orogen and Yangtze Craton [Jiang *et al.* (2016)]. Based on derived patterns of azimuthal anisotropy at periods of 8-40 s from ambient noise tomography, we aim to address two questions: 1) are the Qinling and Longmenshan orogens characterised by two-layered anisotropic structures (thus constraining whether or not subduction is contributing to mountain building processes at these two regions)? 2) What are the deformation relationships between the NE Tibetan Plateau and its neighboring Qinling and Longmenshan orogens? Answers to these questions help to better understand the growth of the NE Tibetan Plateau and the nature of orogenic processes in general.

4.3 Tectonic setting

The Qinling Orogen is one part of the central orogen in China, which is bordered by the Dabie-Sulu orogen in the east and the Qilian-Kunlun orogen in the west. To the southwest, the Tibetan Plateau is the highest and largest plateau in the world with an average elevation of ∼4-5 km and a crustal thickness twice that of average continental crust. The plateau is

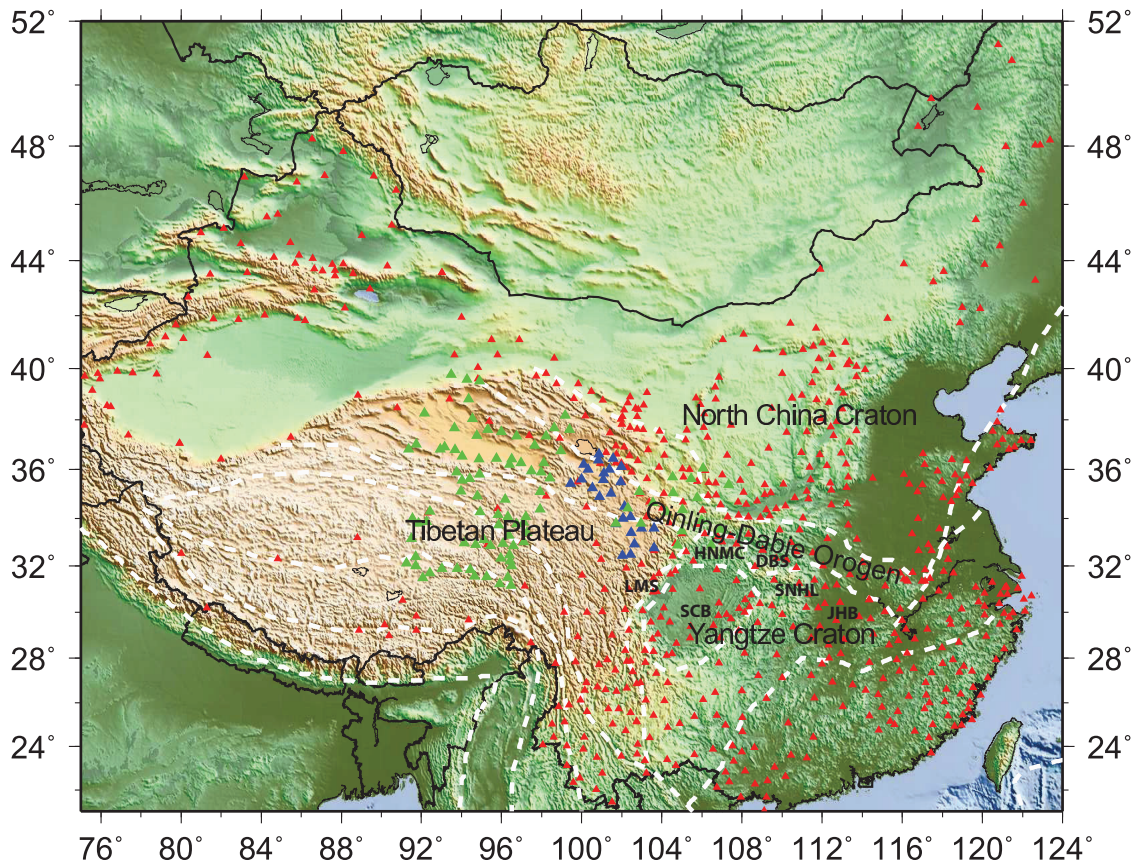

Figure 4.1: Topographic map of China. Thick white dashed lines denote the main tectonic boundaries in the research area. Triangles represent seismic stations from different networks: red ones are from Chinese Provincial networks, blue ones from Northeast Tibet Seismic Experiment (NETS), and green ones from a Seismic Collaborative Experiment in Northeastern Tibet (ASCENT). Abbreviations: LMS-Longmenshan; HNMC-Hannan-Micangshan Dome; DBS-Dabashan Orocline; SNHL-Shennongjia-Huangling Dome; SCB-Sichuan Basin; JHB-Jianghan Basin.

bounded by the Sichuan Basin in the east along the Longmenshan, which is the site of the steepest topographic gradient in the plateau. The Sichuan Basin is associated with the cratonic keel of the Yangtze Craton. Inside the craton, Archean basement and associated intrusive and metamorphic rocks are exposed at Huangling Dome [Gao *et al.* (1999); Qiu *et al.* (2000)], and the largest intrusive complexes of the craton are outcropped at Hannan Dome [Gao *et al.* (1990); Zhou *et al.* (2002)].

The Qinling Orogen results from the Triassic collision between the North China Craton and the Yangtze Craton [Ames *et al.* (1993); Li *et al.* (1993); Meng & Zhang (1999)], followed by a period of intra-continental orogeny. During this period, crustal shortening continued, driving the development of a series of foreland fold-thrust belts on the northern

and western margin of the Yangtze Craton, including the Dabashan, Hannan and Longmenshan segments [Burchfiel *et al.* (1995); Dong *et al.* (2013); Liu *et al.* (2005); Meng & Zhang (2000); Yan *et al.* (2011)]. In contrast, the Dabie Orogen experienced strong extension, as demonstrated by the exhumation of UHP/HP metamorphic rocks, and the formation of the Jianghan Basin on its western edge. The formation of several extensional basins in the upper crust of the Qinling Orogen reflects the initiation of extension in the late Cretaceous [Shi *et al.* (2012); Zhang *et al.* (2001)]. The distinct regimes of deformation in these two areas are attributed to the oblique subduction and clockwise rotation of the Yangtze Craton [Liu *et al.* (2015b); Meng *et al.* (2005); Wang *et al.* (2003)]. To the first-order, the growth of the Tibetan Plateau in the Cenozoic is attributed to the Indian-Eurasian continental collision, which is generally believed to have been initiated about 40-50 My ago [Yin & Harrison (2000)].

4.4 Data and Tomography

In order to image the anisotropic structure in the NE Tibetan Plateau and adjacent areas, we collect ambient noise data from a total of 736 stations (Fig. 4.1) that operated between 2007 and 2009. The seismic stations are mainly from three networks, including the China Provincial Networks [Zheng *et al.* (2009)], the networks of Northeast Tibet Seismic Experiment (NETS) and a Seismic Collaborative Experiment in Northeastern Tibet (ASCENT). We pre-process the ambient noise data by following the procedures described in Jiang *et al.* (2016). After retrieving the symmetric components of stacked cross-correlations from ambient noise, we employ the eikonal tomography of Lin *et al.* (2009) to derive azimuthal anisotropy at 8-40 s periods.

Compared to traditional ray-based tomography methods, such as that of Barmin *et al.* (2001), eikonal tomography [Lin *et al.* (2009)] is not subject to matrix regularisations, which normally include *ad hoc* parameters such as matrix damping and spatial smoothing [Rawlinson & Sambridge (2003)]. Rather, eikonal tomography relates phase velocity directly

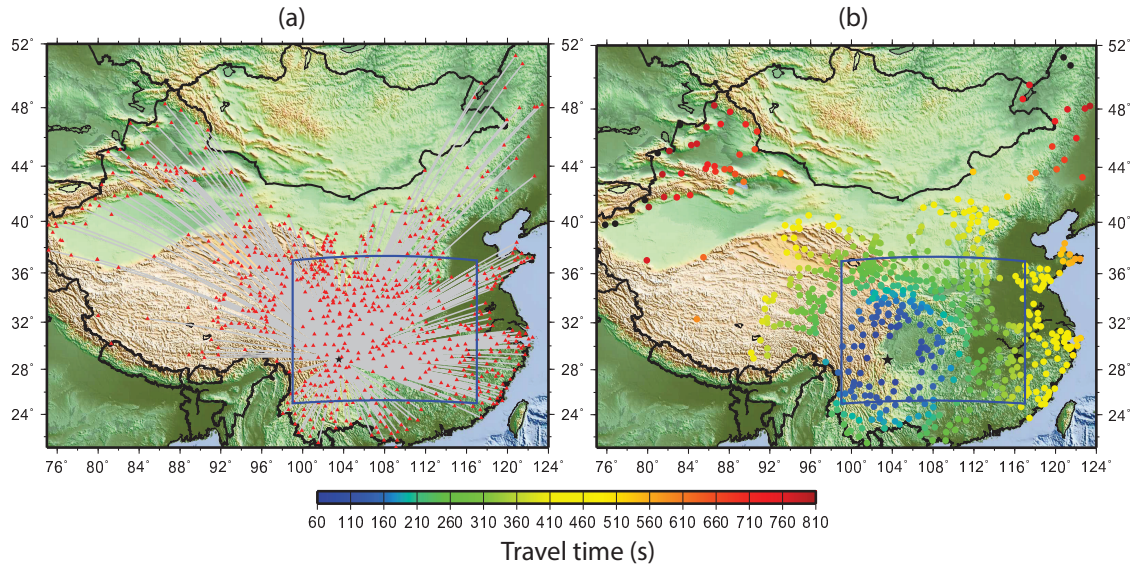

Figure 4.2: (a) Ray paths between station SCMBI (black star) and the remaining 735 stations (red triangles) obtained from cross-correlations. (b) Rayleigh wave travel time measurements based on the ray paths in (a). The blue lines in (a) and (b) outline the main research area of this study, where anisotropic structures are constructed and illustrated in Fig. 4.6-4.8.

to the local travel-time field by employing a simplified eikonal equation of the form

$$\nabla t(r_i, r) \cong \frac{k_i}{C_i(r)} \tag{4.1}$$

In this expression, $t(r_i, r)$ is the traveltime at position r when an effective source is located at $r_i, C_i(r)$ is the local phase velocity for the traveltime field i at position r, k_i is the unit wave number vector for the traveltime field i at position r, and ∇ is the gradient operator. This simplified equation is, however, only valid at high frequencies or if the spatial variation of the amplitude field is small enough compared to the gradient of the travel-time surface [Gouedard *et al.* (2012); Lin *et al.* (2009)]. In this study, our periods of interests of 10-40 s and our target region with a lateral dimension of 1000 km render such conditions well conformed. Fig. 4.2 illustrates an example of great circle paths (Fig. 4.2a) for the construction of a 20 s phase traveltime surface using travel-times calculated from the cross-correlations between station SCMBI and the remaining 735 stations (Fig. 4.2b). Only the traveltime surface inside the research area (outlined by the blue line in Fig. 4.2a and b) is used for the calculation of local phase velocities (Fig. 4.3).

Based on the simplified eikonal equation 4.1, both the local phase velocity and the direction of wave propagation are estimated. Consequently, the method allows a straightforward

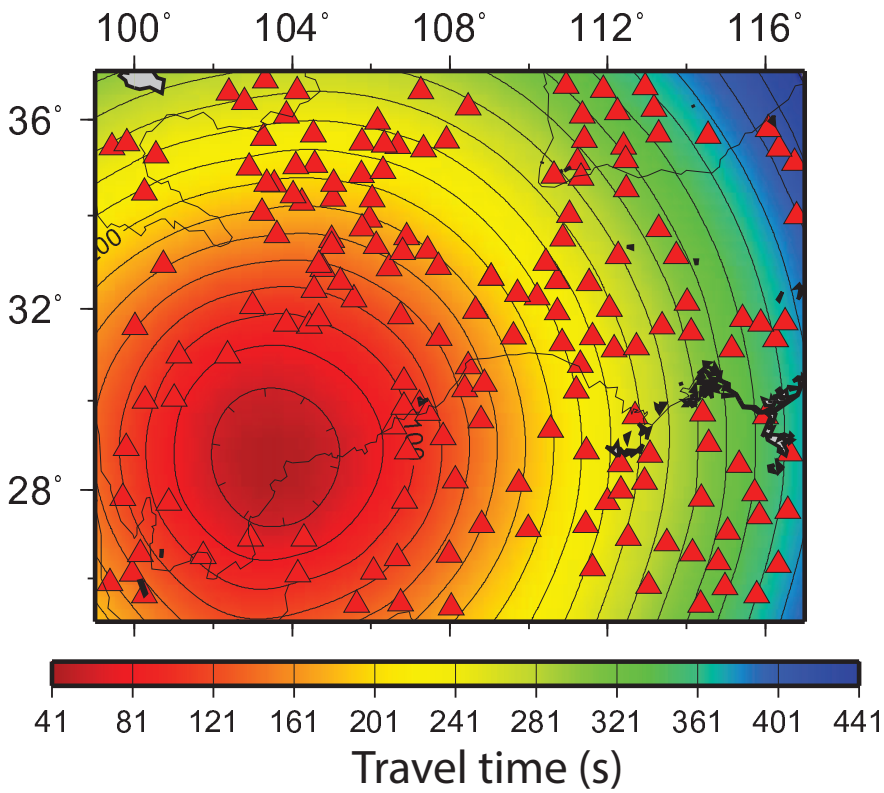

Figure 4.3: The interpolated phase traveltime surface for a 20 s Rayleigh wave centred at station SCMBI. Contours are separated by 20 s intervals.

consideration of azimuthal anisotropy. According to theoretical studies of weakly anisotropic media [Smith & Dahlen (1973)], the azimuthal dependence of phase speed follows the form of

$$c(\omega, \theta) = c_0(\omega) + Acos[2(\theta - \phi)] + Bcos[4(\theta - \alpha)] \tag{4.2}$$

where ω is the angular frequency, θ is the azimuthal angle of the wave number vector counting clockwise from north, A and B are the anisotropic amplitudes, and ϕ and α are the anisotropic fast axes for the 2θ and 4θ components, respectively. In this study, we only consider the 2θ term, which has been previously demonstrated to be the dominant component and a reasonable simplification at most conditions [Lin *et al.* (2010); Pawlak *et al.* (2012); Rawlinson *et al.* (2014a); Yao *et al.* (2010)]. Fig. 4.4 illustrates two examples of the azimuthal dependence of phase velocities and their uncertainties at periods of 10, 20 and 40 s at two locations: one in the NE Tibetan Plateau and the other in the Qinling Orogen.

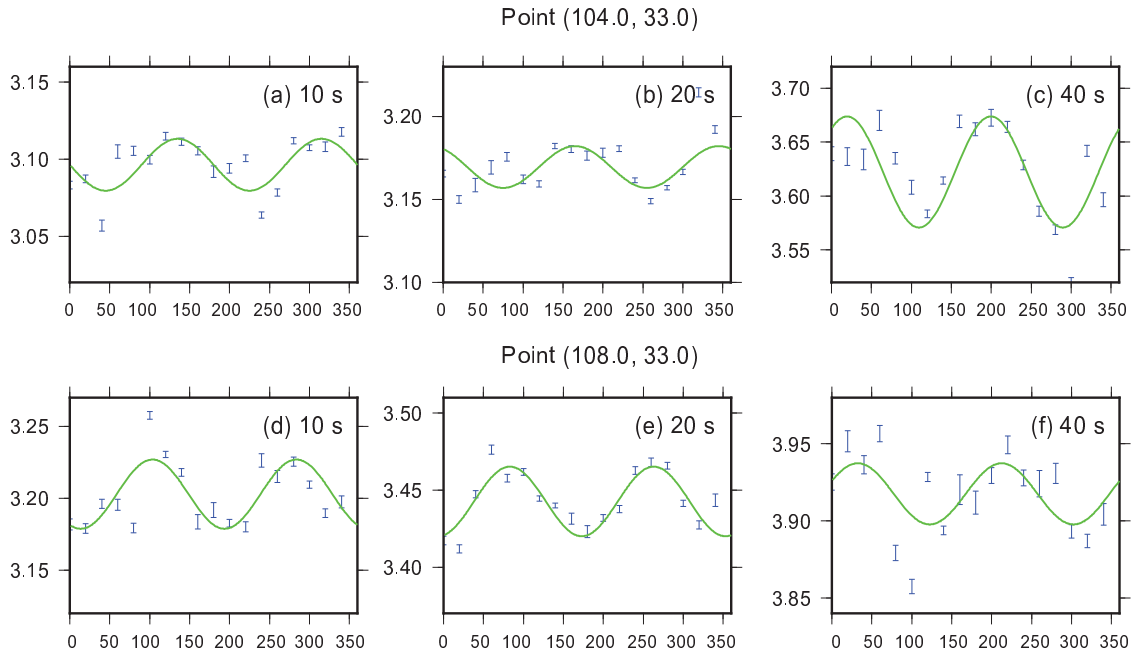

Figure 4.4: Examples of 10, 20 and 40 s period Rayleigh wave phase velocity measurements as a function of azimuth for points in the NE Tibetan Plateau (upper panel) and the Qinling Orogen (lower panel), respectively. The geographic coordinate of each point is denoted at the top of each panel. The solid green lines represent the best fit of the 2θ azimuthal variation (θ is the azimuth of wave propagation defined positive clockwise from north).

An important step in seismic tomography is the analysis of solution robustness [Rawlinson & Sambridge (2003)], in which resolving power is usually estimated by imposing a checkerboard perturbation onto the model inversion. It is, however, difficult to conduct synthetic tests in the case of eikonal tomography due to its accounting of ray-bending effects during the traveltime surface construction. Estimates of robustness thus require sophisticated numerical simulations to model a wavefield similar to that dealt in the tomography using real data. To overcome this limitation, Lin *et al.* (2009) suggested that employing a measurement of coherent length, which represents the extent of correlation between slowness measurements at different locations, can be used to access the resolution of eikonal tomography. Lin *et al.* (2009) demonstrated that such measurements can be approximated by the average inter-station spacing of the seismic stations, which is ∼100 km in this study. Therefore, tomographic features characterised by size >100 km are expected to be reliable, which adequately satisfies the interests of this study. In addition, we compare the isotropic velocity map (20 s) using eikonal tomography with that from Jiang *et al.* (2016) based on

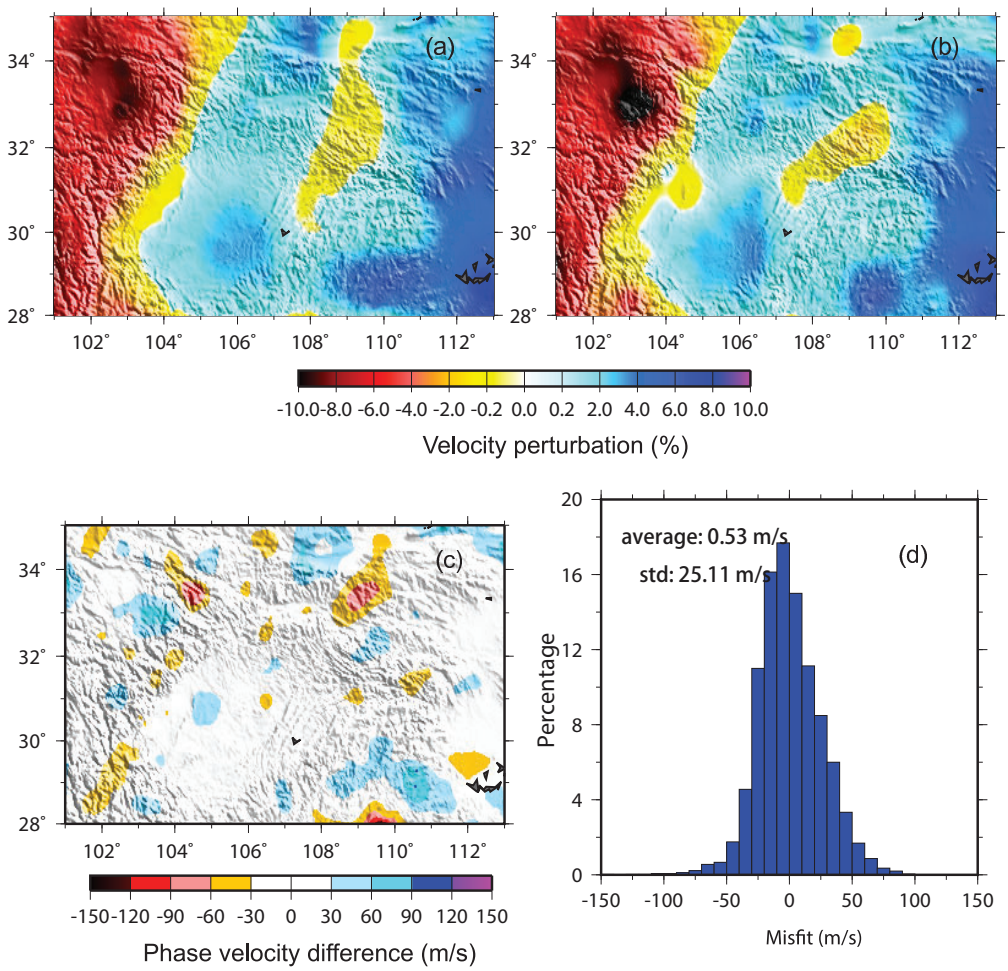

Figure 4.5: (a) Phase velocity map derived from eikonal tomography of Lin *et al.* (2009) from this study. (b) Phase velocity map derived from ray-based tomography of Barmin *et al.* (2001) from Jiang *et al.* (2016). (c) Difference between the maps shown in (a) and (b). (d) Histogram of the differences presented in (c).

ray theory (Fig. 4.5a and b). Minor differences between velocity maps from the two methods are found as shown in Fig. 4.5c and d, indicating that isotropic velocity maps from eikonal tomography are consistent with those from the ray-based method of Barmin *et al.* (2001), which has a general resolution of 60-80 km. The robustness of anisotropic features is even more difficult to assess compared to the resolution of isotropic velocity maps. However, the good fits of 2θ azimuthal variation of local phase velocity, as shown by the two examples in Fig. 4.4 and the small uncertainties of fast direction in most of the regions (Fig. 4.6-4.8) make us confident in azimuthal anisotropic features resolved on the scale of about $1^\circ \times 1^\circ$.

4.5 Results of azimuthal anisotropy

As isotropic velocity features have been discussed previously [Jiang *et al.* (2016)], here we concentrate our discussion on the results of azimuthal anisotropy. Azimuthal anisotropy at 10, 20 and 40 s periods are superimposed on their isotropic velocity maps in (a) of Fig. 4.6-4.8, along with the amplitude of anisotropy and the uncertainty of the fast axis in (b) and (c) of Fig. 4.6-4.8 respectively.

At 10 s period, which is mostly sensitive to upper crustal structures, anisotropy in the NE Tibetan Plateau and west Qinling Orogen ($> 3\%$) is much stronger than in the rest region (Fig. 4.6a). The fast direction of azimuthal anisotropy in these regions is mostly NW-SE, rotating to a nearly N-S direction when reaching the south of 30 °N. The amplitude of the anisotropy decreases slightly towards the eastern edge of the Longmenshan. The Sichuan Basin displays weak anisotropy with amplitudes less than 0.5%, and is associated with large uncertainties (Fig. 4.6c). In the east Qinling Orogen, the orientation of anisotropy mostly follows an E-W direction, although there are subtle differences along the strike of the Qinling Orogen.

At 20 s period (Fig. 4.7a), the velocity and azimuthal anisotropy mostly reflects mid/lower crustal structures at the Yangtze Craton and Qinling Orogen, whereas tomographic features at this period still reflect the middle crustal structures in the Tibetan Plateau due to its thick crust. Consistent with the results of Jiang *et al.* (2016), variations in isotropic velocities at this period reflect distinct variations of crustal thickness: a thin crust in the east of 110 °E, a "normal" crust in the middle (mostly beneath the Sichuan Basin) and a thick crust in the west beneath the Tibetan Plateau. Similarly, anisotropic features in the three regions are also distinct from each other. In most of the Tibetan Plateau and its adjacent west Qinling Orogen, the fast direction is still dominated by a NW-SE direction, as observed in the 10 s tomography. However, both amplitude and direction of the anisotropy are different from that at 10 s in the region abutting the Longmenshan, where the lowest isotropic velocities are observed. The fast axis in this region shows a trend of clockwise rotation from the north to the south, and it becomes parallel to the strike of the orogen in the region south of 32 °N. The Sichuan Basin continues to exhibit weak anisotropy at this period, while the adjacent

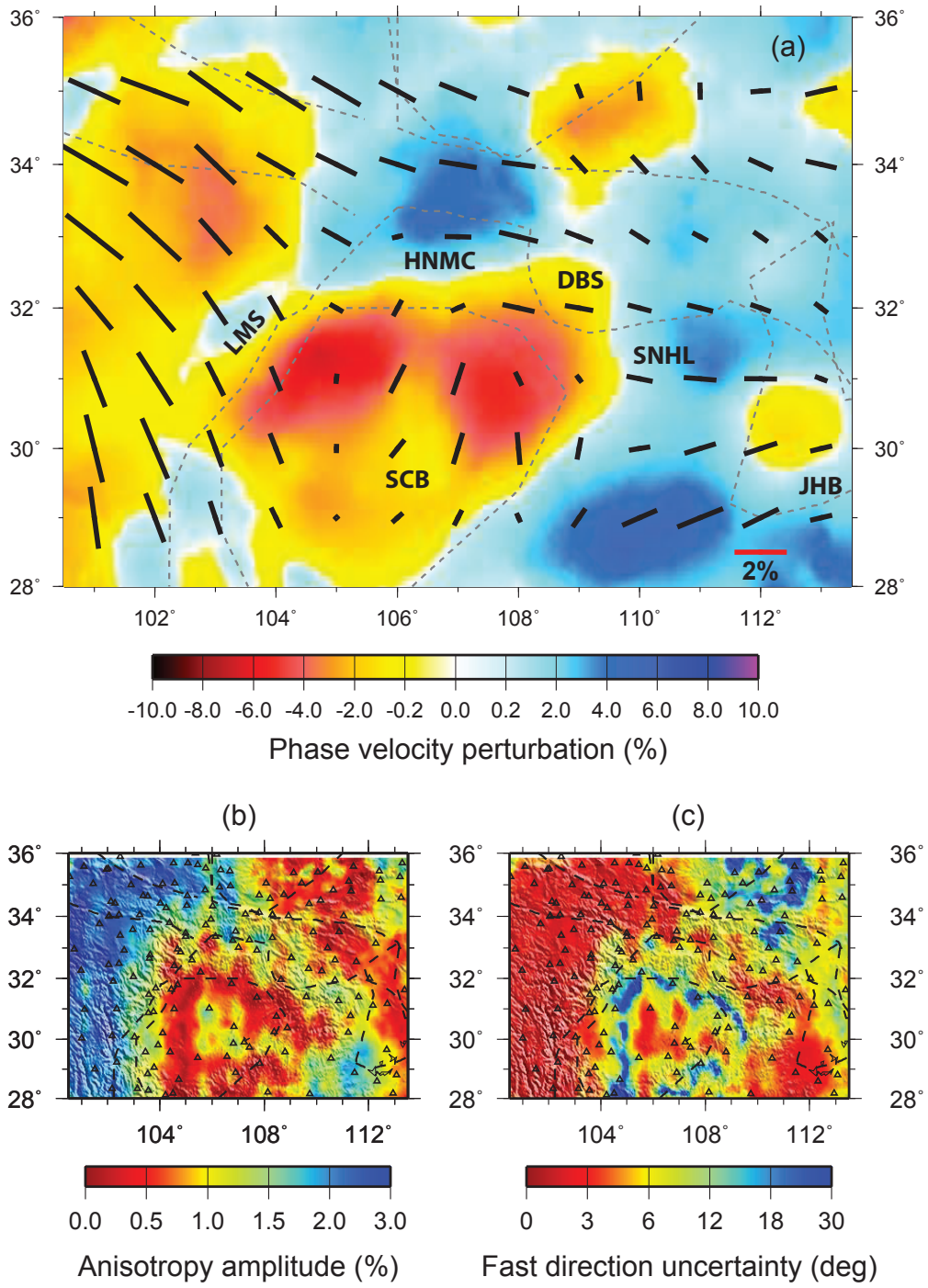

Figure 4.6: (a) The observed 10 s Rayleigh wave 2θ azimuthal anisotropy maps superimposed on the isotropic velocity maps. The lengths of the bars represent peak-to-peak amplitudes, proportional to the length of the bar denoted at the bottom right. (b) Peak-to-peak amplitude of anisotropy for the research area in Figure 4.6a, presented in percent. (c) The uncertainty in the angle of the fast direction θ for the research area in Figure 4.6a. Abbreviations: LMS-Longmenshan; HNMC-Hannan-Micangshan Dome; DBS-Dabashan Orocline; SNHL-Shennongjia-Huangling Dome; SCB-Sichuan Basin; JHB-Jianghan Basin.

east Qinling Orogen in the north continues to show a strong E-W fast direction. This pattern is distinct from the region east of 110 °E, where more complex anisotropic structure is observed.

At 40 s period (Fig. 4.8a), anisotropy in the region east of the Longmenshan reflects upper mantle structures, whereas that of the NE Tibetan Plateau continues to reflect mid/lower crustal structures. The most prominent feature at this period is a localised anisotropic anomaly with an amplitude of more than 3% at the NE corner of the Tibetan Plateau (Fig. 4.8b), mostly north of 30 °N. The fast direction in the region dominantly follows the NNE-SSW direction, which is parallel to the strike of the Longmenshan. This pattern is distinct from that in the remaining NE Tibetan Plateau (west of 102 °E and north of 35 °N), where azimuthal anisotropy is in a NW-SE direction, similar to that at the shorter periods of 10 and 20 s. The strong anisotropy extends further SE to the western edges of the Sichuan Basin. The rest of the Sichuan Basin still displays weak anisotropy. The fast direction is mostly NE-SW beneath the Qinling Orogen, especially in the Dabashan Orocline, rotating to a nearly N-S direction near the eastern boundary of the Tibetan Plateau.

The variations of fast direction shown above are confined by the boundaries of each tectonic unit, seemingly reflecting pronounced, but distinct deformation in these regions. The noted anisotropic features may be related to important mantle dynamic processes, which we discuss in the following section.

4.6 Discussion

4.6.1 Comparison with anisotropy from XKS splitting

We assemble anisotropic measurements from XKS (SKS, PKS and SKKS) splitting in the NE Tibetan Plateau from a number of studies [Huang *et al.* (2011); Huang *et al.* (2008); Leon Soto *et al.* (2012); Li *et al.* (2011); Wang *et al.* (2008); Wu *et al.* (2015); Zhang *et al.* (2012)], and plot them in Fig. 4.9a. Overall, the NE Tibetan Plateau is characterized by strong anisotropy with a dominant NW-SE direction. Although the fast direction derived from XKS splitting represents integrated anisotropy from the core-mantle boundary to the

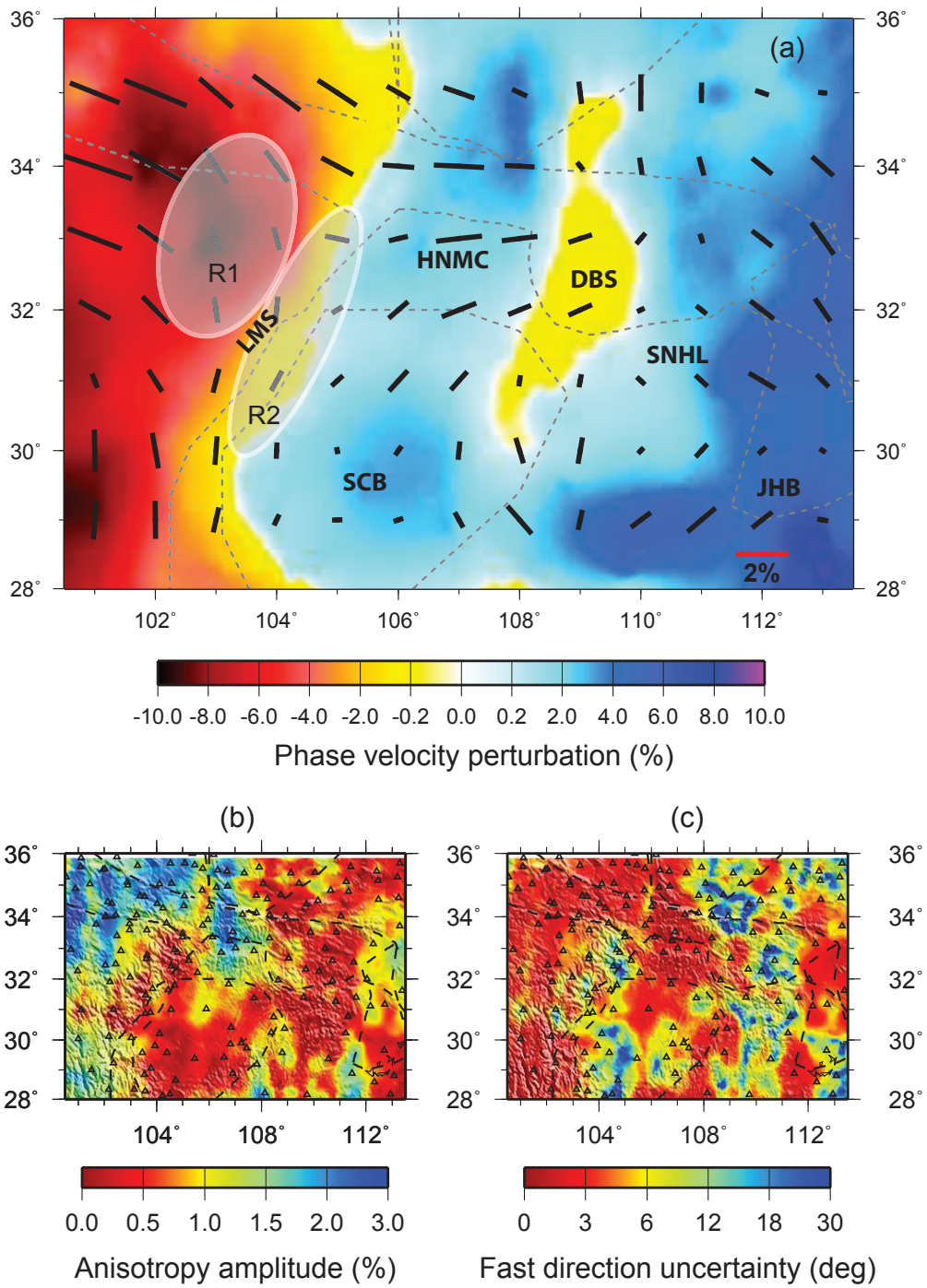

Figure 4.7: Same as Fig. 4.6, but for 20 s period. Grey shaded ellipses represent the two regions referred in the text. R1-Region 1; R2-Region 2.

surface, the consistent NW-SE fast axis at the depths of 75-175 km from seismic tomography [Pandey *et al.* (2015)] indicate that significant anisotropy exists in the upper mantle.

In this study, a consistent NW-SE fast direction at 8-40 s periods, as represented by the yellow line in Fig. 4.9b, is observed at some regions of the NE Tibetan Plateau (mostly in the west of 102 °E and north of 35 °N). This suggests that considerable anisotropy exists in the crust, playing an important role in explaining the overall NW-SE SKS splitting times. Such tomography-derived anisotropy is also consistent with the fast direction (NW-SE) resolved by receiver functions in the region [Wang *et al.* (2016)].

However, for most of the other regions in and around the NE Tibetan Plateau, the variations of fast direction with period from this study imply variations of seismic anisotropy with depth, suggesting depth-dependent deformation in the crust. Complex anisotropy is also observed east of 111.0 °E, in the region with a thin crust. In this study, we mainly highlight the anisotropic features in the Qinling Orogen, the Longmenshan and the NE Tibetan Plateau, and discuss their implication for different deformation mechanisms.

4.6.2 Two-layered anisotropic structures in the Qinling Orogen

The significant variations of anisotropic fast direction at short (<20 s) and long (>20 s) period ends in the period band of 8-40 s (represented by the blue line in Fig. 4.9b) suggest the existence of two anisotropic layers in the east Qinling Orogen, each of which may be related to different deformation processes.

Seismic anisotropy in the upper crust has been attributed to shape preferred orientation (SPO) of cracks and fractures [Crampin (1984); Crampin (1985)]. In the mid/lower crust, however, cracks and fractures must be closed due to the pressure from overlying rocks [Hrouda *et al.* (1993); Kern & Wenk (1990)]. Alternatively, foliated rocks may act as a major contributor to seismic anisotropy at these depths [Brocher & Christensen (1990); Okaya & Christensen (2002)]. The E-W orogen-parallel fast direction beneath the east Qinling Orogen observed at periods of 10-20 s (Fig. 4.6a and 4.7a) may be attributed to the combined effects of E-W directed faults and metamorphic foliations, resulting from widespread compression during the continent-continent collision between the North China Craton and Yangtze Craton

and the following intra-continental orogeny [Liu *et al.* (2015a); Meng & Zhang (2000); Zhang *et al.* (2001)]. In addition, small variations of fast axis along the strike of the orogen may reflect crustal heterogeneity in the northern margin of the Yangtze Craton [Jiang *et al.* (2016)]. This orogen-parallel anisotropy probably extends to the mid-crust level, as indicated by the sub-parallel anisotropic pattern between 10 and 20 s period. The subtle angular differences of the fast direction between the two periods indicate possible influences from the second anisotropic layer in the deep crust (Fig. 4.9b), where a consistent NE-SW fast direction is observed.

The fast axis of anisotropy at 40 s period is mainly perpendicular to the strike of the orogen, mostly in a NE-SW direction (Fig. 4.8a), which reflects the anisotropy in the lower crust and uppermost mantle. This feature is particularly evident beneath the Dabashan Orocline, where the arc-shaped orogen front extrudes and thrusts onto the Yangtze Craton. As suggested by Jiang *et al.* (2016), the Hannan (HN) and Shengnong-Huangling (SNHL) Domes in the region may be mechanically strong and spatially large enough to act as indenters to the thrusting, assisting the formation of the Dabashan Orocline. Compared to the Dabashan area, where the fast direction at this period points to the convex direction of the arcuate shape, azimuthal anisotropy in the rest of the east Qinling Orogen and the HN at corresponding periods rotate counter-clockwisely with the fast-axis at the longitude of 104 °E being nearly in a N-S direction.

From a seismic reflection profile crossing the main thrust of the Dabashan Orocline [Dong *et al.* (2013)], shear zones in the deep crust have been identified (mostly below ∼30 km depth). This is consistent with the regional Vs model of Jiang *et al.* (2016), in which localised low Vs is imaged at ∼30 km depth beneath the Dabashan. LPOs may be generated in the shear zones, where ductile deformation likely dominates [Ramsay (1980)]. The candidate anisotropic minerals under shearing include amphibole in the lower crust and olivine in the upper mantle, both of which are thought to be abundant at corresponding depths [Tatham *et al.* (2008); Nicolas & Christensen (1987)]. Shearing within the shear zones most likely originates from the subduction of the Yangtze Craton during the continent-continent collision [Li *et al.* (1993); Meng & Zhang (1999)]. Therefore, the shear zones in the mid/lower crust could possibly represent a transitional ductile regime to compensate

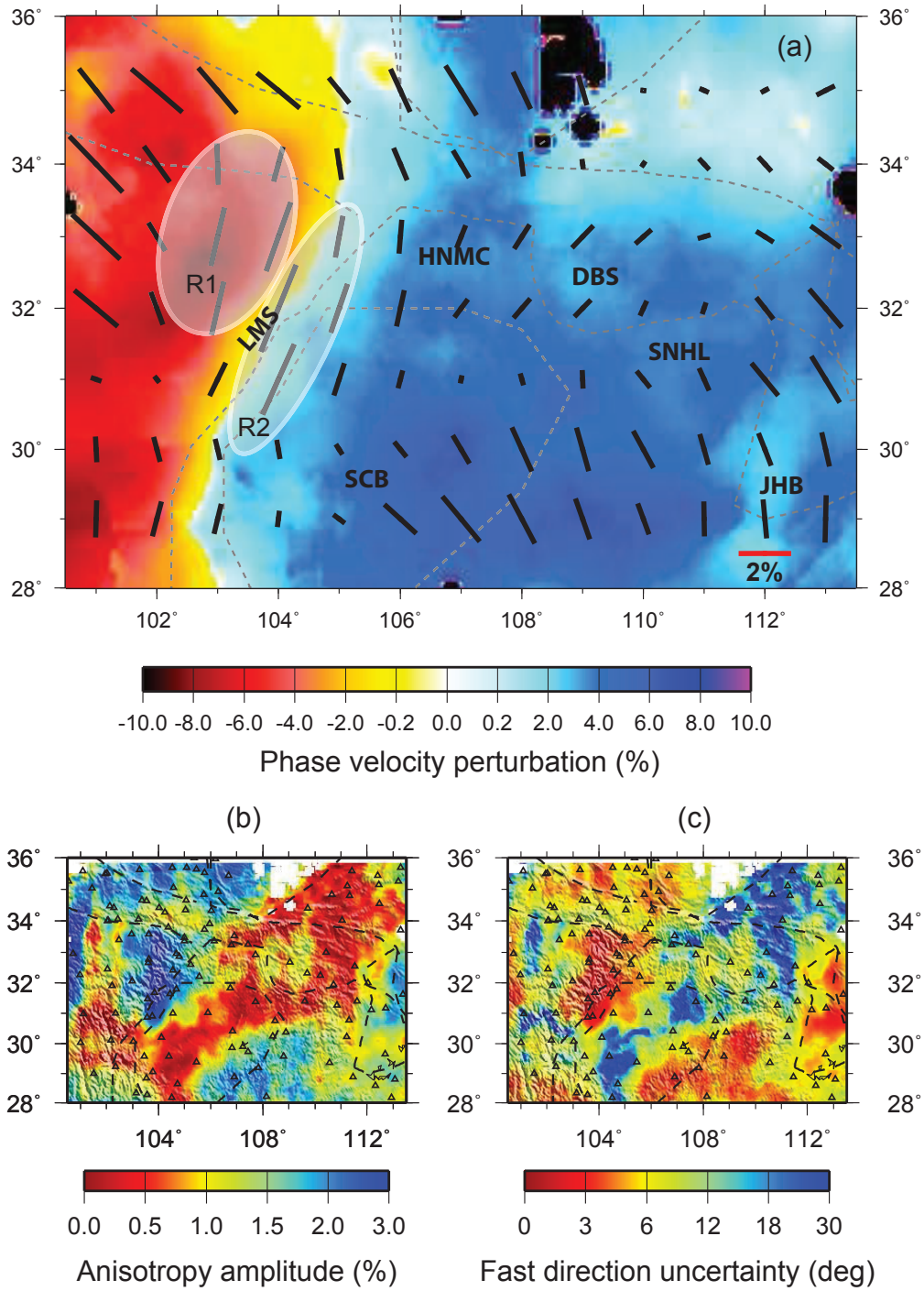

Figure 4.8: Same as Fig. 4.6 and 4.7, but for 40 s period. Grey shaded ellipses represent the two regions referred in the text. R1-Region 1; R2-Region 2.

both brittle deformation in the upper/mid crust, and subduction in the upper mantle. This suggests a mountain building process similar to that proposed for Taiwan orogen [Huang *et al.* (2015)], where two layers of anisotropy at corresponding depths with 90° rotation of anisotropic fabrics are also observed.

4.6.3 Two-layered anisotropic structures in the NE Tibetan Plateau and Longmenshan

Significant variations of fast direction with period are also observed in the NE Tibetan Plateau (east of 102 °E) and the adjacent Longmenshan, suggesting the existence of multiple crustal anisotropic layers.

The widespread NW-SE directed faults in the region could generate SPO with horizontal symmetry, contributing to the NW-SE fast direction observed at 10 s. Such interpretation is also consistent with the study of Xie *et al.* (2013), in which SPO of cracks and/or faults explains strong (∼3%) negative radial anisotropy (Vsv>Vsh) in the shallow crust of the region. In addition, Vergne *et al.* (2003) identified an anisotropic layer in the upper crust of the region, which is attributed to the LPO of flysch and schist. Both minerals are strongly anisotropic [Christensen (1965)] and are widely distributed in the Songpan-Ganze region [Nie *et al.* (1994); Zhou & Graham (1996)], serving as other possible contributors to the high-amplitude anisotropy seen in this study, under the far-field compression resulting from the Indian and Eurasian continental collision.

The fast axis of azimuthal anisotropy at 40 s (Fig. 4.8), mostly reflecting the mid/lower crustal structures in the region between 102 °E and the Longmenshan front, is nearly NE-SW. When compared with the isotropic velocity features, the anisotropic pattern in the region can be further categorized into two regions (Fig. 4.7a and 4.8a): region 1 is coincident with the existence of low velocity zones (LVZs) based on the results of Jiang *et al.* (2014) (represented by the green line in Fig. 4.9b); region 2 has no LVZs present (mostly beneath the Longmenshan front; represented by the red line in Fig. 4.9b).

Based on geophysical and petrological evidence, Jiang *et al.* (2014) concluded that the distribution of LVZs in the NE Tibetan Plateau is consistent with the channel flow model of

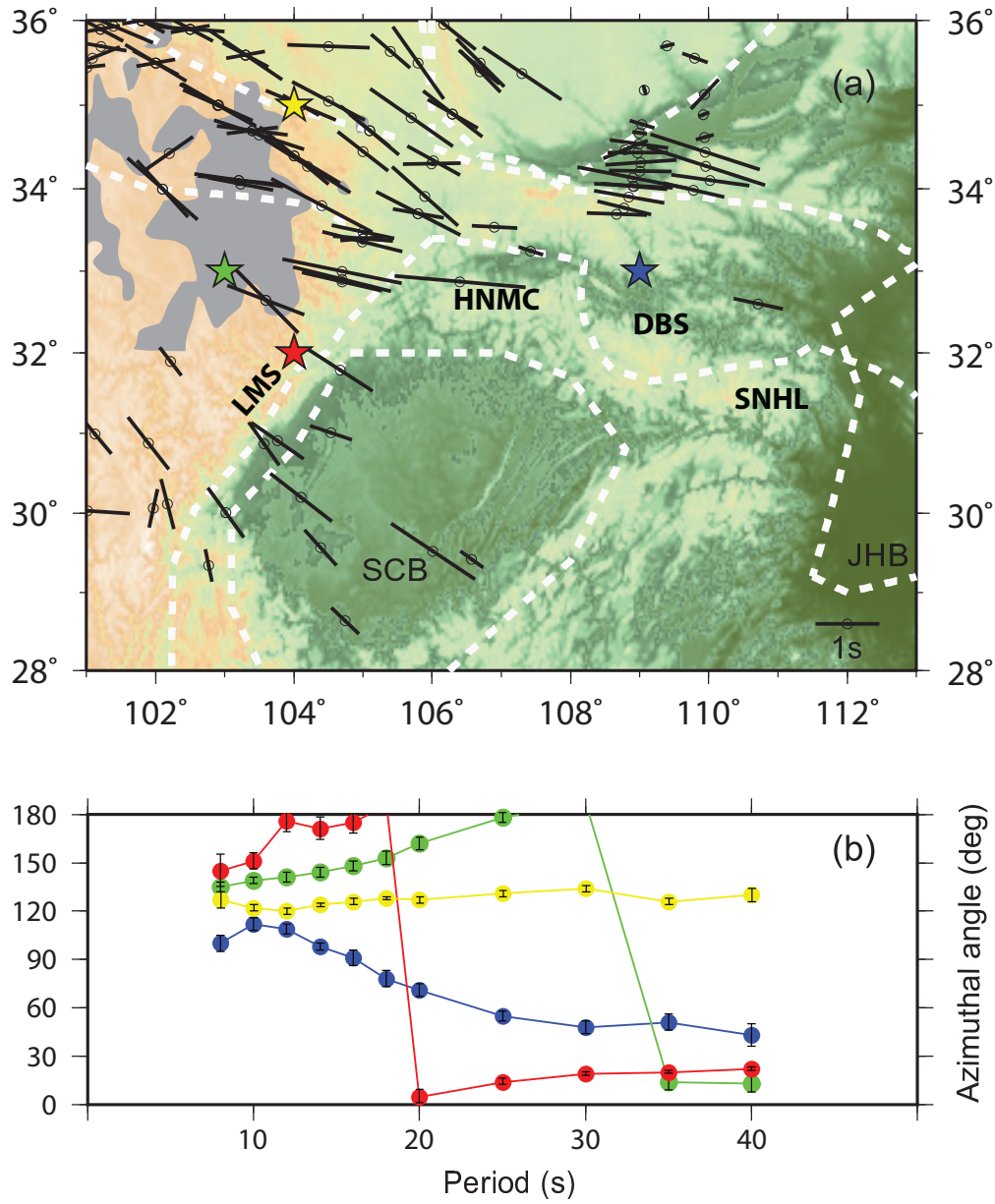

Figure 4.9: (a) XKS splitting measurements from the studies of Huang *et al.* (2011), Huang *et al.* (2008), Leon Soto *et al.* (2012), Li *et al.* (2011), Wang *et al.* (2008), Wu *et al.* (2015) and Zhang *et al.* (2012). The splitting time is scaled according to the bar shown in the bottom left of the figure. The four coloured points denote the geographic locations of the four examples where period-dependent anisotropic features are compared. The grey shaded region represents the area with 80% accepted models from the Monte-Carlo inversion with the minimum Vsv at 15-40 km depth range smaller than Vsv at both 15 and 40 km depths based on Jiang *et al.* (2014). Abbreviations: LMS-Longmenshan; HNMC-Hannan-Micangshan Dome; DBS-Dabashan Orocline; SNHL-Shennongjia-Huangling Dome; SCB-Sichuan Basin; JHB-Jianghan Basin. (b) Variations of fast axis direction with period for the four points marked in Fig. 4.9a. The vertical bars represent scaled uncertainty of the derived fast direction.

Clark & Royden (2000) and Royden *et al.* (1997), with noticeable extrusion of LVZs into the west Qinling Orogen between 102 °E and 104 °E. If so, shearing within the channel would preferentially orient the fast axis of anisotropic minerals to the flow direction, generating considerable azimuthal anisotropy within the region of LVZs, such as region 1. According to petrological models of Hacker *et al.* (2014), the mid/lower crust of Tibet is best explained by mica-bearing rocks aligned in a sub-horizontal plane with the presence of 2% silicate melt, considering the available geophysical features of extensive low velocities [Yang *et al.* (2012)] and 3-4% positive radial anisotropy [Xie *et al.* (2013)]. Therefore, mica could be a candidate for such an anisotropic mineral. However, the LPO caused by sub-horizontal alignment of mica can only explain the positive radial anisotropy as seen in Xie *et al.* (2013), not the azimuthal anisotropy observed in this study, due to its hexagonal symmetry. Alternatively, Liu *et al.* (2015c) proposed that SPO of fluid domains could generate a fast direction parallel to the fluid transfer/layering direction. Therefore, the 2% silicate melt inferred from petrological models could be connected in a NE-SW direction due to crustal flow, generating NE-SW directed azimuthal anisotropy; whereas mica-bearing rocks aligned in a sub-horizontal plane generate the positive radial anisotropy. Therefore, region 1 most likely represents a separate channel, where mid/lower crustal materials flow in a NE-SW direction. This separate channel beneath region 1 is distinct from a narrow region in the east, which is relatively higher in velocity [Jiang *et al.* (2014)] and exhibits weaker radial anisotropy [Xie *et al.* (2013)] and consistently azimuthal anisotropy in a NW-SE direction.

In region 2, the strong orogen-parallel anisotropy ($> 3\%$) in the mid/lower crust is coupled with strong negative radial anisotropy (Vsv>Vsh) of comparable amplitude [Xie *et al.* (2013)]. This is significantly different from that in region 1, where the mid/lower crust is dominated by positive radial anisotropy (Vsh>Vsv). In addition, the anisotropy in region 2 starts to fluctuate at shorter periods (approximately 20 s; represented by the red line in Fig. 4.9b) compared to that in region 1. The relatively faster isotropic Vs in region 2 suggests melt may not exist in the region, whereas mica could still be abundant. The sub-vertical foliation of mica sheets in the NE-SW oriented plane could explain both the azimuthal and radial anisotropy in the region. The NE-SW directed plane could be the result of NW-SE directed compression due to the interaction with the Sichuan Basin and

eastward extrusion of the plateau [Li *et al.* (2012)], while the sub-vertical foliation of mica may be caused by rheological differences in the lower crust associated with a pronounced Moho step beneath the Longmenshan and Sichuan Basin [Zhang *et al.* (2010)], leading the lower crust in the west of the Longmenshan to flow nearly vertically towards the east as the result of blockage of the strong Sichuan Basin. Therefore, the anisotropic patterns reveal a significantly different mountain building process beneath the Longmenshan compared to that beneath the Qinling Orogen.

4.7 Conclusion

In this study, we employ the eikonal tomography method of Lin *et al.* (2009) to investigate azimuthal anisotropy at the conjunction of Qinling Orogen, Yangtze Craton and NE Tibetan Plateau, as a complement to our previous isotropic velocity model in this region [Jiang *et al.* (2016)]. The model reveals depth-dependent anisotropic features in the region. In particular, two-layered anisotropic structures are observed beneath the Qinling Orogen, Longmenshan and the NE Tibetan Plateau. In the Qinling Orogen, the fast direction of anisotropy is parallel to the orogen in the upper/mid crust, while it is perpendicular to the trend of the orogen in the deep crust and uppermost mantle. The two-layered anisotropic feature suggests a mountain building process similar to that proposed for the Taiwan orogen [Huang *et al.* (2015)], where a transitional ductile regime in the lower crust serves to compensate brittle deformation in the upper/mid crust and subduction in the upper mantle. However, in the Longmenshan, the pattern of the anisotropic features relative to the orogenic geometry is completely reversed. The upper crust beneath the orogen is dominated by orogen-perpendicular fast directions; whereas the mid/lower crust displays orogen-parallel fast directions. This suggests that the anisotropy in the upper crust may be related to the fractures of dominant faults and the mid/lower crustal anisotropy reflects combined effects of horizontal shortening and vertical ductile deformation. Strong NE-SW oriented anisotropy is also imaged in the mid/lower crust of the NE Tibetan Plateau, with a distribution coincident with the presence of LVZs. This structure is interpreted to represent a separate channelized flow, developed as a response of the barrier of the Sichuan basin to the plateau's eastward

extrusion.

5

Crustal structure of the Newer Volcanics Province, SE Australia, from ambient noise tomography

5.1 Abstract

Intraplate volcanism is a widespread phenomenon, and is generally regarded to be independent of plate tectonics. The Newer Volcanics Province (NVP) of SE Australia represents the most recent (and arguably still active) intraplate volcanism on the Australian continent, and has been postulated to originate from the combined effect of localised shear flow and edge-driven convection. In this study, we use ambient noise tomography and Monte-Carlo inversion methods to construct the first local 3D crustal Vs model of the NVP region,

with a resolution of ∼35 km. The model displays distinct crustal velocity features near the eastern and western margins of the NVP, which may point to the existence of a lithosphere-scale plumbing system for the migration of melt associated with the boundary between the Delamerian Orogen and the Lachlan Orogen, which underlies the NVP. In particular, exceptionally high velocities are observed in the middle crust of the Delamerian Orogen, which are best explained by buried magmatic arcs. This suggests a subduction-accretion origin for the Delamerian Orogen. The model also images small localised velocity reductions in the lower crust at the region where the two distinct lithospheric units meet. The low velocity zone is spatially correlated with the top of a prominent lithosphere-scale low-resistivity zone (10-30 Ωm), which we interpret to represent intruded magmatic sills with small proportions of melt remaining. The minor erupted magmas and the small magmatic intrusions seen in the current lower crust indicate a much smaller magmatic plumbing system beneath the NVP than that of Yellowstone, which has a mantle-plume origin.

5.2 Introduction

Intraplate volcanism, such as the Yellowstone volcanoe in North America [Huang *et al.* (2015); Lowenstern & Hurwitz (2008); Yuan & Dueker (2005)] and the Changbai volcanoes in NE China [Guo *et al.* (2016); Lei & Zhao (2005); Tang *et al.* (2014); Zhao *et al.* (2009)] is a widespread phenomenon, which cannot be explained by the traditional paradigm of plate tectonics. The common explanations for such phenomena range from edge-driven convection [King & Anderson (1998)], plume-related hot-spot origin [Davies & Davies (2009)], glacial rebound [Uenzelmann-Neben *et al.* (2012)], lithospheric dripping [Le Pourhiet *et al.* (2006); Levander *et al.* (2011)], lithospheric cracking [Forsyth *et al.* (2006)] to shear-induced asthenosphere upwelling [Conrad *et al.* (2011)].

The Newer Volcanics Province (NVP) is the most recent active intraplate volcanism on the Australian continent. It includes more than 700 eruptions [Boyce (2013)], with the earliest at about 4 Ma ago [McDougall *et al.* (1966); Price *et al.* (1997)] and the latest at < 5 ka [Wellman & McDougall (1974)]. The erupted basaltic magmas cover a region more than 19,000 km^2 [Boyce (2013)], with an average thickness of less than 60 m [Johnson

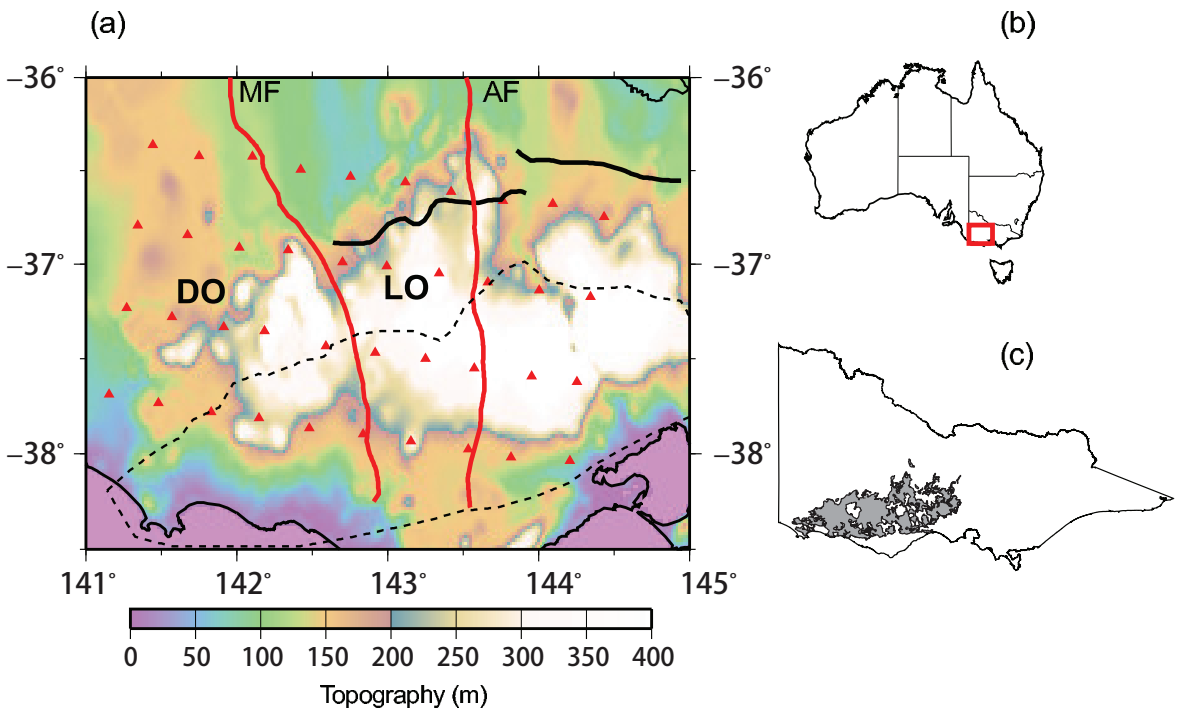

Figure 5.1: (a) Tectonic units overlying the topographic map of the research area. Red triangles denote the seismic stations used in this study. Thick red lines delineate the main crustal faults. Thin dashed black lines delineate the geographic boundaries of the erupted magmas around Newer Volcanics Province, whose exact distribution is shown in the insert map of c. Thick black lines denote the location of seismic reflection lines shown in Fig. 5.9a. MF: Moyston Fault; AF: Avoca Fault; DO: Delamerian Orogen; LO: Lachlan Orogen. (b) The geographic location (red square) of the research area within the Australian continent. (c) The distribution of the Quaternary New Volcanics Province in the south-western Victoria. The figure is created with the data downloaded from the Geological Survey of Victoria.

(1989)]. Previous studies have proposed that the NVP is the product of plume-related hot-spot magmatism based on their geochemical signatures [McDonough *et al.* (1985); Wellman & McDougall (1974)]. However, the E-W distribution of the NVP, which is perpendicular to the northerly drift of the Australian plate and the lack of an obvious age-progression to the eruptions does not support a simple plume model [Price *et al.* (1997); Sandiford *et al.* (2004)]. Previous seismic tomography studies in the region found little in the way of support for this scenario [Graeber *et al.* (2002); Rawlinson & Kennett (2008); Rawlinson & Fishwick (2012)]. Alternatively, the thermal instabilities [Lister & Davis (1989)] associated with the break-up of the Antarctic-Australian continent [Miller *et al.* (2002)] have been invoked as a possible mechanism for causing local asthenosphere upwelling. However, an age

gap of 80-50 Ma between the initial continental rifting and the eruption of volcanoes in the NVP [Vogel & Keays (1997)] renders such a theory problematic. A recent study of seismic tomography together with geodynamic modelling supports the mechanism of edge-driven convection [Demidjuk *et al.* (2007); Farrington *et al.* (2010)] in a localised thin lithosphere as being sufficient to generate such volcanism [Davies & Rawlinson (2014)]. However, it has been suggested that a nearby hotspot track - presumably fuelled by a plume - may have combined with the edge-driven convection cell to initiate the volcanism at about 4.5 Ma [Davies *et al.* (2015)].

While knowledge of the detailed lithospheric structure beneath intraplate volcanoes helps to understand their deep origins, storage and transportation of magma to the surface is largely dictated by crustal structure. For example, recent regional seismic tomography beneath Yellowstone [Huang *et al.* (2015)] has, for the first time, imaged a large basaltic magma reservoir in the deep crust, which is located beneath a previously well-resolved but smaller rhyolitic reservoir in the upper crust [Farrell *et al.* (2014)]. The two magmatic reservoirs with distinct compositions form the crustal magmatic plumbing system which helps connect mantle melting and upwelling processes with eruptions at the surface. The two bodies help explain both the bimodal basaltic-rhyolitic volcanism and the hydrothermal degassing budget required by the large thermal and CO_2 fluxes at the surface [Hurwitz & Lowenstern (2014); Lowenstern & Hurwitz (2008)], thus contributing to a better understanding of magmatic system dynamics.

The crustal magmatic system beneath the NVP is still not well known, mostly owing to a lack of information in the mid-lower crust. Crustal imaging studies in and around the NVP region are limited to several seismic reflection lines [Cayley & Taylor (2001); Cayley *et al.* (2011)] and tomographic studies with a lateral dimension of >1000 km [Arroucau *et al.* (2010); Pilia *et al.* (2015a); Young *et al.* (2013a)] in the region. Several important questions still remain however, such as the location of any magmatic reservoirs beneath the NVP and how the magmas migrate from the mantle to the surface. In particular, the NVP is located above a proposed boundary where two Palaeozoic orogens - the Delamerian Orogen (DO) and Lachlan Orogen (LO)- meet. Both geophysical [Graeber *et al.* (2002); Rawlinson & Fishwick (2012); Rawlinson *et al.* (2014b)] and geochemical studies [Handler *et al.* (1997);

McBride *et al.* (1996)] have revealed that the two orogens are floored by distinctly different lithosphere [Cayley *et al.* (2011); Davies & Rawlinson (2014)], with a possible Proterozoic continental lithosphere underlying the east Delamerian and a Phanerozoic lithosphere beneath the transition zone from the Delamerian to the Lachlan orogens. However, questions still remain about how these regional differences may have influenced the formation of the NVP.

In this study, we aim to construct a high-resolution 3D crustal model beneath the NVP and its northern conjunction with the DO and LO in western Victoria. We assemble approximately five months of ambient noise data from 40 seismic stations in the region in order to produce phase velocity maps at periods of 2-18 s. The resulting local dispersion curves on a $0.1^\circ \times 0.1^\circ$ grid are then inverted for a 3D crustal model using a non-linear Bayesian Monte-Carlo approach. By combining the highly resolved crustal Vs model, which has an average lateral resolution of about 35 km, with surface heat flow measurements and the Bouguer gravity field in the region, we aim to address two scientific questions: 1) what is the crustal tectonic setting of the NVP, and 2) how are the magmas of the NVP stored and how do they migrate through the crust? The answers to the above questions will not only shed light on the early accretionary processes of the eastern Australian continent, but will also help us to understand crustal magma dynamics in an intraplate geological setting.

5.3 Data and data processing

Seismic ambient noise data were collected from the LF98 (Lachlan Fold Belt 1998) array, which is the earliest component of the largest transportable seismic array experiment in the southern hemisphere, collectively known as WOMBAT. It consists of more than 700 station deployments in eastern Australia over the last 17 years and has an average spacing of about 50 km on the mainland [Kennett *et al.* (2015); Rawlinson *et al.* (2014b); Rawlinson *et al.* (2014a)]. LF98 used 40 short-period digital seismometers (1 Hz corner frequency) operating between May and September of 1998. The array covers a significant portion of the NVP as well as the transition between the Delamerian and Lachlan orogens in western Victoria (Fig. 5.1). The 40 seismic stations were laid out in four lines, with about 50 km spacing

between lines and about 30 km station spacing along lines [Graeber *et al.* (2002)]. Although most of today's ambient noise tomography studies rely on more than one year of ambient noise cross-correlations, the five month deployment of LF98 did gather sufficient background energy for surface wave tomography due to the proximity of the stations to the coastline, where seismic energy is supplied by ocean wave interactions (Fig. 5.2).

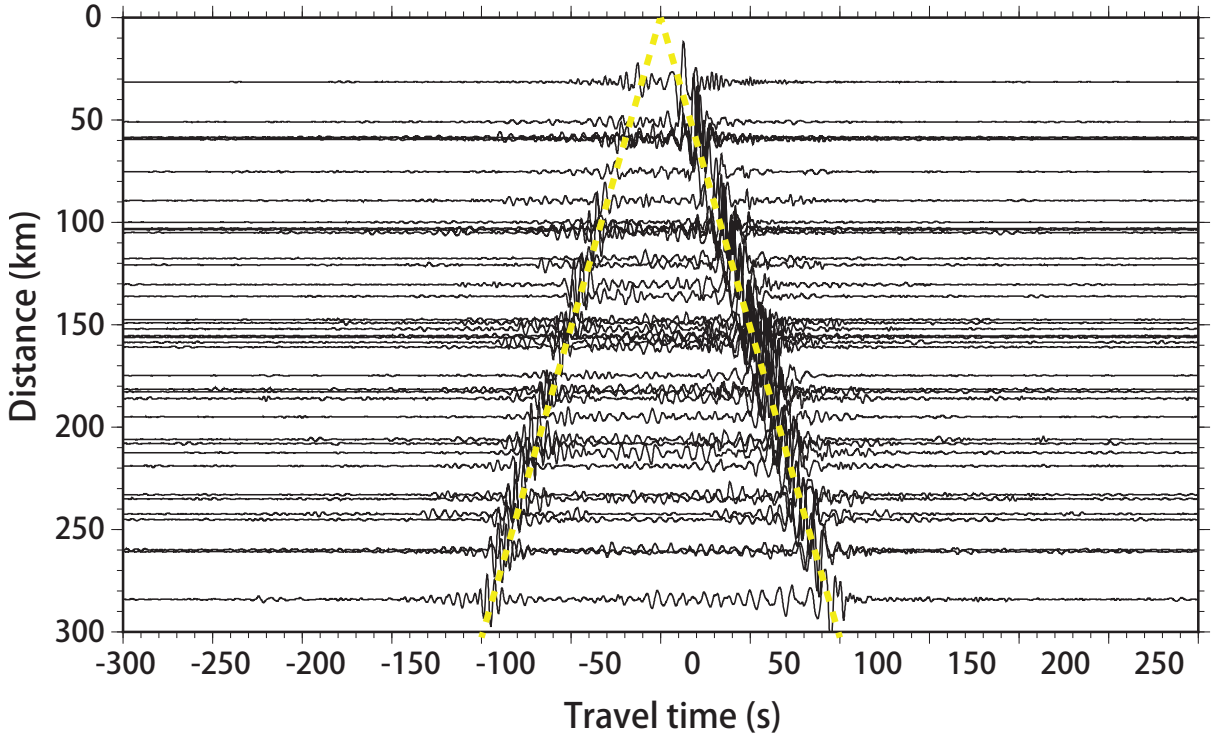

Figure 5.2: Examples of five-month ambient noise cross-correlations between A02 and the other 39 stations filtered at 2-20 s periods. The yellow dashed lines display a surface wave move-out of 3 km/s.

We process the ambient noise data following the procedures described in Bensen *et al.* (2007), except in the stacking procedure. Band-pass filters with periods of 0.4-100 s are first applied to all of the waveforms after removing the instrument responses. Both temporal and frequency normalisation are then applied to the filtered data. We perform the daily cross-correlations between all station pairs over the five months. Instead of following the convention of stacking them all linearly as we did in our previous studies [Jiang *et al.* (2014); Yang *et al.* (2012)], we first linearly stack the daily cross-correlations using a ten-day window. Then an S-transform based stacking method [Schimmel *et al.* (2011); Stockwell *et al.* (1996)] is applied to stack the ten days' worth of cross-correlations to produce the final inter-station

cross-correlations. The adoption of the S-transform based stacking method is designed to boost the signal to noise ratio (SNR) of the cross-correlations, and has been demonstrated to be effective in previous ambient noise tomography studies [Ren *et al.* (2013); Yang (2014)]. The final inter-station cross-correlations from the stacking procedure described above are compared with results from conventional linear stacking in Fig. 5.3a. As can be seen, the SNR has been improved significantly by using the new stacking procedures, which helps to retain more inter-station paths, especially at the long period end of this study (14-18 s). Finally, we cut the stacked cross-correlations to get positive and negative components, which are again stacked together to form the symmetric component. The method of automated frequency-time analysis (FTAN) [Bensen *et al.* (2007); Dziewonski *et al.* (1969); Levshin & Ritzwoller (2001)] is applied to the symmetric components to measure Rayleigh wave phase velocity dispersion curves at 2-18 s periods. Fig. 5.3b shows the inter-station phase velocity differences from the cross-correlations based on the new stacking procedure compared to conventional stacking. The small average through all the periods reflects the reliability of the inter-station phase velocity extracted from the new stack procedure, which is used in all subsequent analysis.

To discard bad measurements before conducting the tomography, we perform quality control on the measured phase velocity dispersion curves based on three criteria. Firstly, the distance between each station-pair must be longer than one wavelength. The adoption of one wavelength criteria is to improve the number of ray paths towards the long period end of this study, which otherwise would be too sparse for tomography. A recent study has verified that using one wavelength as the minimum distance can produce reliable tomography results [Luo *et al.* (2015)]. Secondly, the signal-to-noise ratio (SNR) of the final stacked symmetric cross-correlations must be greater than 15. Finally, the misfit of the travel time between dispersion measurements and that determined by an initial tomography run must be within 1.5 s, after which outliers are removed and the tomography procedure is repeated. After this quality control, more than 600 cross-correlations (80%) are retained for periods ranging from 4-10 s. Even at 18 s, there are still more than 200 cross-correlations used.

The selected phase velocity dispersion curves are then inverted for phase velocity maps on a $0.1^\circ \times 0.1^\circ$ grid using the iterative fast marching based eikonal tomography method

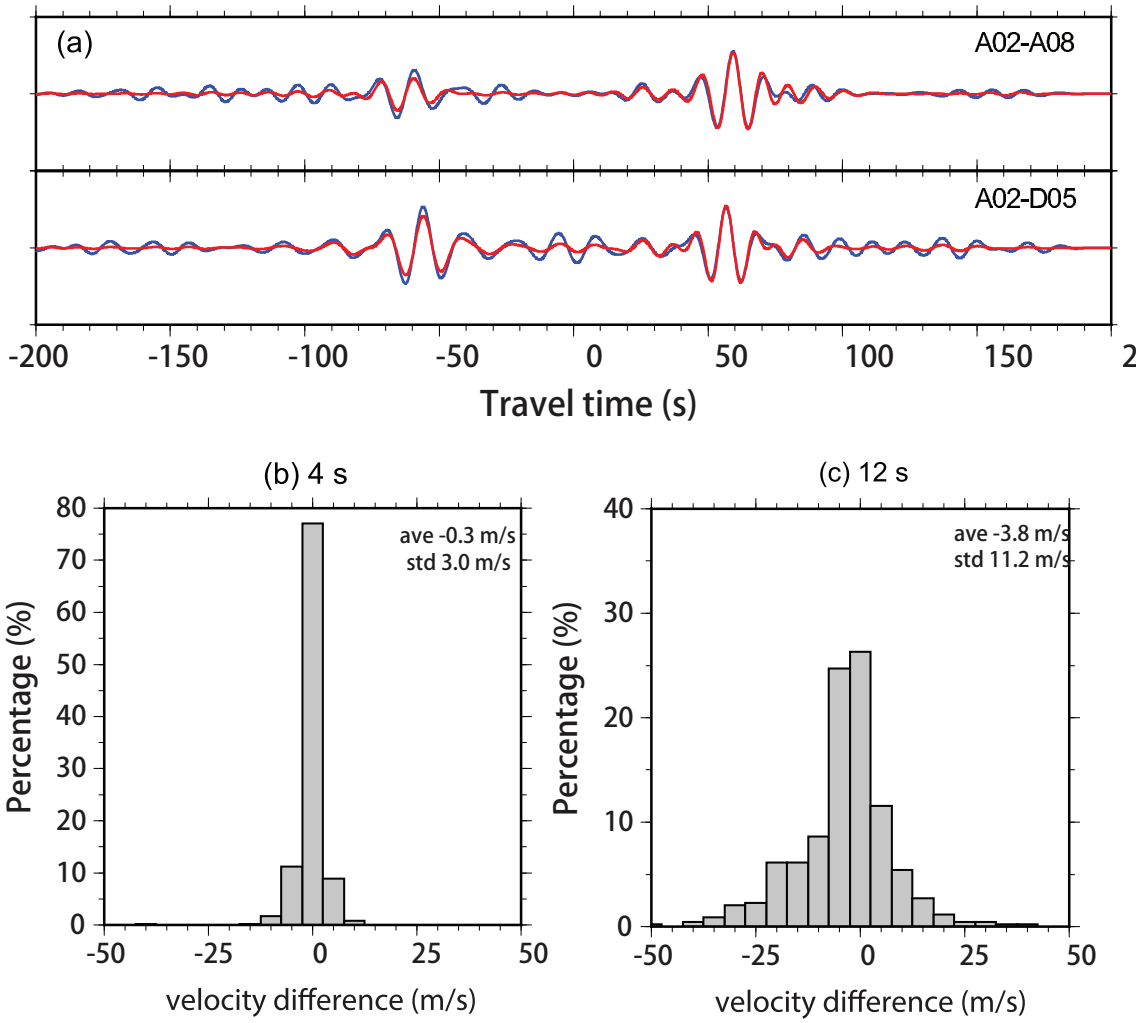

Figure 5.3: (a) Examples of better SNR of the cross-correlations using the new stacking procedures (red) than that from conventional linear stacking (black). (b) Histograms of the inter-station phase velocity differences from the cross-correlations based on new stacking procedures and those from conventional stacking at 4 and 12 s. The average and standard deviations are also denoted.

[Rawlinson & Sambridge (2003)]. The fast marching algorithm [Sethian & Popovici (1999)] uses a finite-difference method to solve the eikonal equation and compute (in this case) 2D travel time fields on a spherical shell, which enables the tracking of wave fronts in heterogeneous media [Rawlinson & Sambridge (2004)]. Thus, the off-great circle effects are also taken into account during the iterative non-linear inversion process. The inverse problem is solved using a subspace inversion technique, which employs singular value decomposition (SVD) to automatically control the dimension of the subspace onto which the inverse problem is projected (see Kennett *et al.* (1988) for more details). The eikonal solver and the subspace

scheme are applied iteratively to address the non-linear nature of the inverse problem. During the inversion, we used a range of damping and smoothing parameters to construct the trade-off curves between data fit and model roughness to determine the optimal values according to Rawlinson & Sambridge (2003).

5.4 Checkerboard models and phase velocity maps

5.4.1 Checkerboard tests

Before phase velocity maps are presented and interpreted, checkerboard tests are performed to assess the resolution of the tomography results. The input phase velocity model is constructed on the same geographic grid as used for the inversion of the LF98 data, and has alternating cells ($0.4^\circ \times 0.4^\circ$ in dimension and 3% in amplitude) of opposite sign. Noise with a Gaussian distribution of 0.4 s, which is close to the standard deviation of the final travel time misfit from the real data tomography is added to the synthetic dataset associated with the checkerboard model. Synthetic phase velocities are then calculated from the velocity model using the same station pairs as those in real data tomography. During the tomographic inversion of synthetic data, the same parameters used in tomography based on the observed data are employed. Fig. 5.4 displays the recovered velocity models at periods of 4, 8, 12 and 16 s. The anomalies with sizes of $0.4^\circ \times 0.4^\circ$ are well retrieved for most of the study region, indicating that the inversion can adequately recover structures as small as 35 km.

5.4.2 Tomography results

The resulting phase velocity maps display a series of interesting regional-scale velocity features. Compared to the recent studies of Pilia *et al.* (2015a), Pilia *et al.* (2015b) and Young *et al.* (2013a), which also utilize ambient noise data from LF98 but mainly focus on the large-scale architecture of the southern Tasmanides, this study displays more detailed structures beneath the NVP.

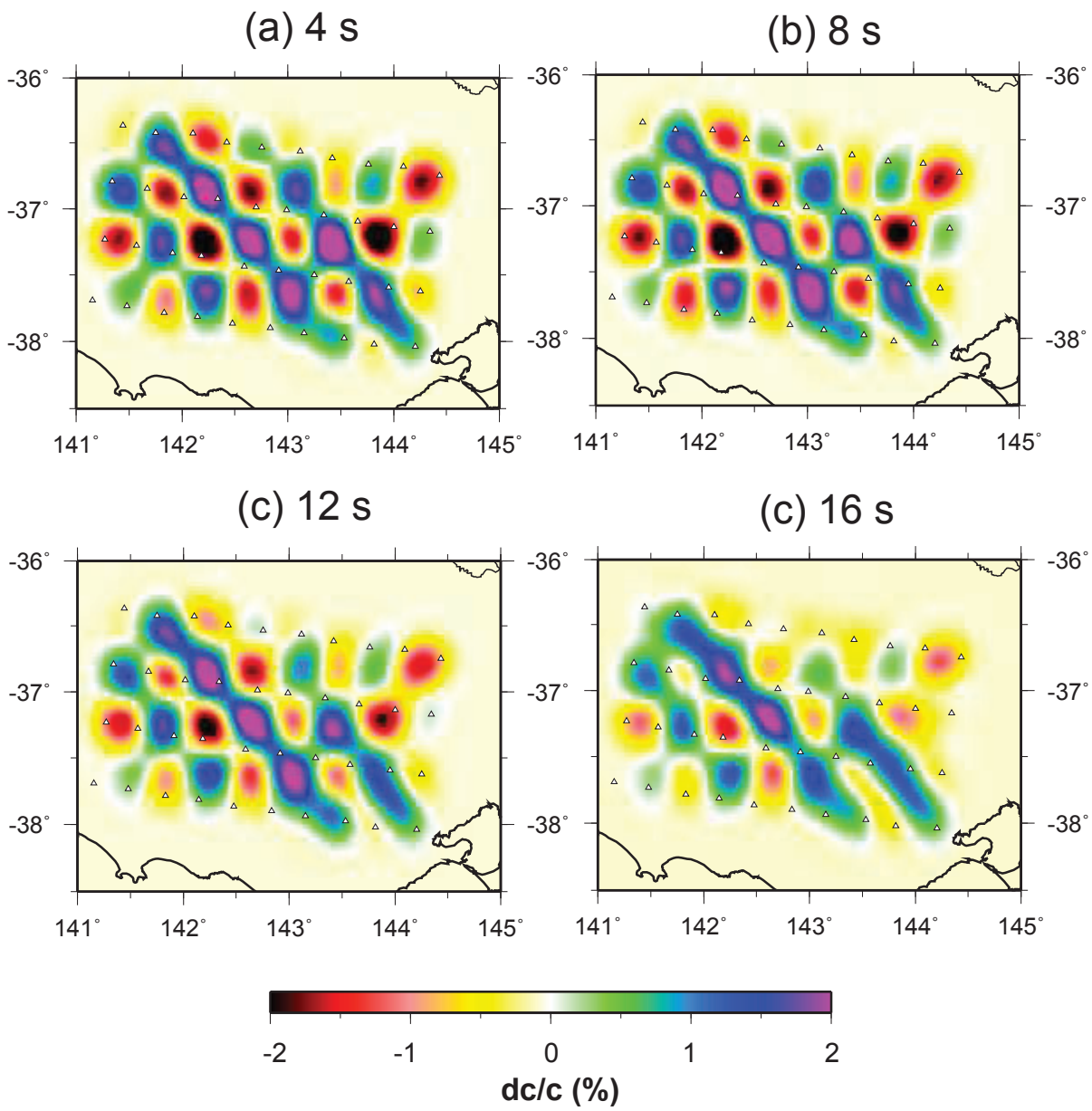

Figure 5.4: Recovered checkerboard models with anomalies of $0.4° \times 0.4°$ at 4 (a), 8 (b), 12 (c) and 16 (d) s periods.

At short periods, like 2 and 4 s (Fig. 5.5a-b), the velocities are mainly sensitive to uppermost crustal structure. The most prominent feature shown at these periods is the significant velocity differences across the MF; the velocity to the west of the MF is considerably lower than that east of the MF. At 2 s in particular, the velocity difference across the fault in some regions is as large as 6%, while it is more than 5% at 4 s. The high velocities east of the MF are elongated mainly along the MF and in the SE-NW direction. The velocity contrast

along the MF appears to be less prominent in the south as the MF reaches the southern boundary of the NVP.

Phase velocities at periods of 8-14 s reflect mid crustal structures in the region. As seen in Fig. 5.5c-e for phase velocity maps at 8, 12 and 14 s respectively, the pattern of velocity variations across the MF is completely reversed compared to that at 2-4 s periods, with the velocity in the DO is now much higher than that in the LO. Moreover, the velocity transition zone now occurs further to the east of the MF compared to that at 2-4 s. This probably indicates that the fault dips to the east from the surface to the middle crust. The AF appears to be associated with several areas of relatively low velocities at these periods. It is also worth noting that the average velocity beneath the NVP region is much lower compared to other regions, such as the Delamerian orogen to the west of the MF.

At periods of 16-18 s, the long period end of this study, the phase velocity mostly reflects mid/lower crustal structure. Fig. 5f displays the phase velocity distribution at 16 s. The velocity patterns at this period are similar to that at 14 s but slightly higher in amplitude. The checkerboard test conducted at this period demonstrates that velocity anomalies in the western and central regions are recovered well but those in the eastern edges suffer from some smearing effects. Therefore, it is hard to define the exact spatial extent of the more concentrated low velocity anomalies along the AF. However, these low velocities along the AF have also been observed at shorter periods (12-14 s), implying that they exist in a broad range of depth.

5.5 Shear wave inversion

Since Rayleigh wave phase velocities at individual periods are sensitive to a broad depth range, the phase velocity maps as shown in the last section provide us with a vertically integrated view of the shear-wave velocity structure of the crust. To better define the velocity structures at specific depths, particularly in the deep crust, inversion of phase dispersion is required to produce depth dependent shear velocities. To do so, we first extract local dispersion curves at 2-18 s period from the phase velocity maps on a $0.1^\circ \times 0.1^\circ$ grid. The extracted local dispersion curves are then inverted for 1D Vs profiles using a Bayesian

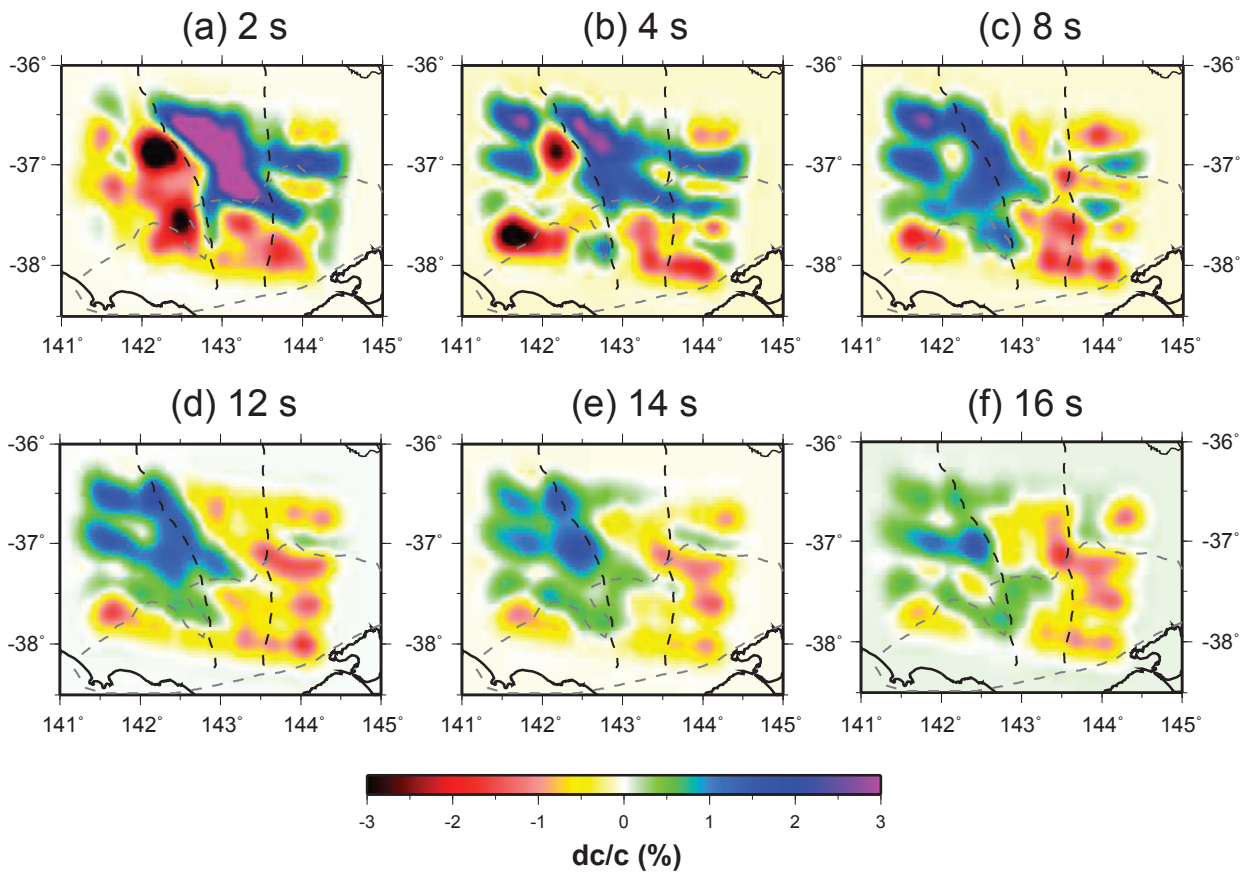

Figure 5.5: Rayleigh wave phase velocity maps at the periods of (a) 2 s, (b) 4 s, (c) 8 s, (d) 12 s, (e) 14 s and (f) 16 s, plotted as the percent perturbation relative to the average of each map. The dashed black lines outline the Moyston Fault, Avoca Fault and the geographic boundaries of the erupted magmas respectively.

Monte-Carlo method developed by Shen *et al.* (2013). In this study, although the inverted 1D profile is referred to as a Vs model, it is actually a Vsv model since we only use Rayleigh waves from ambient noise. Details of the method can be found in Shen *et al.* (2013) and are only briefly described below.

For each geographic location, a 1D Vs profile is constructed from the surface down to a depth of 100 km, consisting of two layers, a crystalline crustal layer and an upper mantle layer. The velocity variations in the crust and upper mantle are represented by four and five B-spline coefficients respectively. The initial values of these coefficients are calculated based on the crustal Vs model of Salmon *et al.* (2013a) and an upper mantle velocity model of Kennett *et al.* (2013). During the inversion, the crustal thickness is fixed according to the Australian Moho depth model [Aitken *et al.* (2013); Salmon *et al.* (2013b)], and

we only invert for Vs by scaling Vp and density to Vs, as Rayleigh wave phase velocities are primarily sensitive to Vs. The Vp/Vs ratio in the crust is set to 1.73, assuming it is a Poisson solid. Density is calculated based on the Vp following the linear relationship of $density = 0.541 + 0.3601 * Vp$ [Brocher (2005)] as suggested by Christensen & Mooney (1995). Vp is converted directly from the Vs model according to the Vp/Vs ratio. Attenuation effects on surface wave dispersion are corrected [Kanamori & Anderson (1977)] following Dziewonski & Anderson (1981), as was done by Yang *et al.* (2012) and Jiang *et al.* (2014).

During the inversion, we do not add any explicit prior constraints when choosing acceptable models, meaning that Vs in the crust and mantle is completely free to vary, by up to 20% in the crust and 10% in the mantle. After completing a comprehensive sampling of model space in the neighbourhood of the initial model, the posterior distribution of acceptable models at each geographic location on the $0.1^\circ \times 0.1^\circ$ grid is obtained. The mean of the distribution is taken as the final Vs profile and the standard deviation provides an estimate of Vs uncertainties. All of these 1D Vs profiles are then assembled together to obtain a 3D Vs model.

5.6 3D crustal Vs model

The resulting 3D crustal Vs model is presented as slices at different depths in Fig. 5.6 and as four cross sections in Fig. 5.7. The locations of the four cross sections are indicated in Fig. 5.6a.

At depths of 3 and 5 km (Fig. 5.6a-b), the distribution of shear velocity anomalies is very similar to the distribution of phase velocity anomalies at 2 and 4 s periods (Fig. 5.5a-b). The most distinct feature at such depths is the coincidence of the significant velocity boundary with the surface projection of the MF. West of the MF, the velocity is generally low with a pronounced circular zone of low velocity situated immediately west of the MF, juxtaposed against much higher velocities immediately to the east. The high-velocity anomalies in the east, which are 3% higher than the average, exhibit some degree of elongation, both along the strike of the MF and a E-W direction. Such regional high velocities mostly terminate at depths of 5-6 km as shown in the vertical profiles (Fig. 5.7b and d).

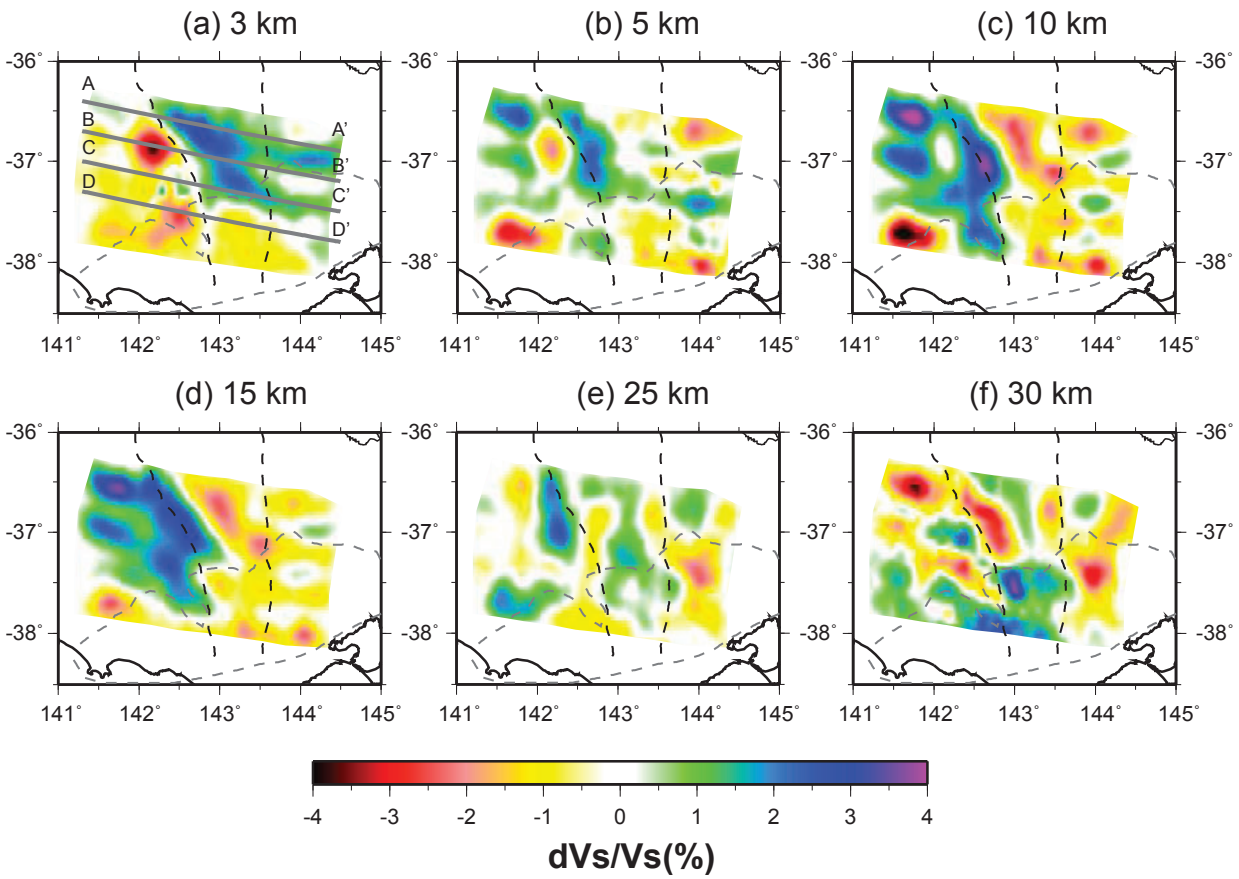

Figure 5.6: Vsv maps at the depths of (a) 3, (b) 5, (c) 10, (d) 15, (e) 25 and (f) 30 km respectively. All depths are relative to sea level. The solid grey lines in Fig. 5.6a outline the locations of the profiles of four transects shown in Fig. 5.7.

In the middle crust, like depths of 10, 15 km (Fig. 5.6c-d), the velocity pattern changes completely as compared to that in the shallow crust. The region located west of the MF becomes dominated by strong positive anomalies, which are 3-4% faster than the velocity in most of the regions east of the MF. At these depths, the separation of the velocity between the west and east outlines the geometry of the MF, which is generally east dipping. As displayed in the four vertical profiles, the >100 km wide anomaly in the mid-lower crust immediately west of the MF exhibits higher velocities compared to that in the east of the MF. Within the region located to the east of the MF, velocity variations in the mid crust is much smaller, only about 1-2% in amplitude. In general, the NVP still exhibits low velocities in the mid crust level, with velocities similar to much of the western Lachlan orogen.

In the lower crust, like depths of 25 and 30 km (Fig. 5.6e-f), the significant velocity

separation along the MF fades, and the velocity variations are more locally distributed. Relatively low velocities start to appear beneath both the DO and the LO. In particular, a region of 2-3% velocity reduction is revealed beneath the east of the surface projection of the AF. This velocity anomaly has been observed continuously from 25 to 30 km depths. Overall, the velocity pattern displayed at 30 km depth is similar to that at 25 km depth, but has higher amplitude.

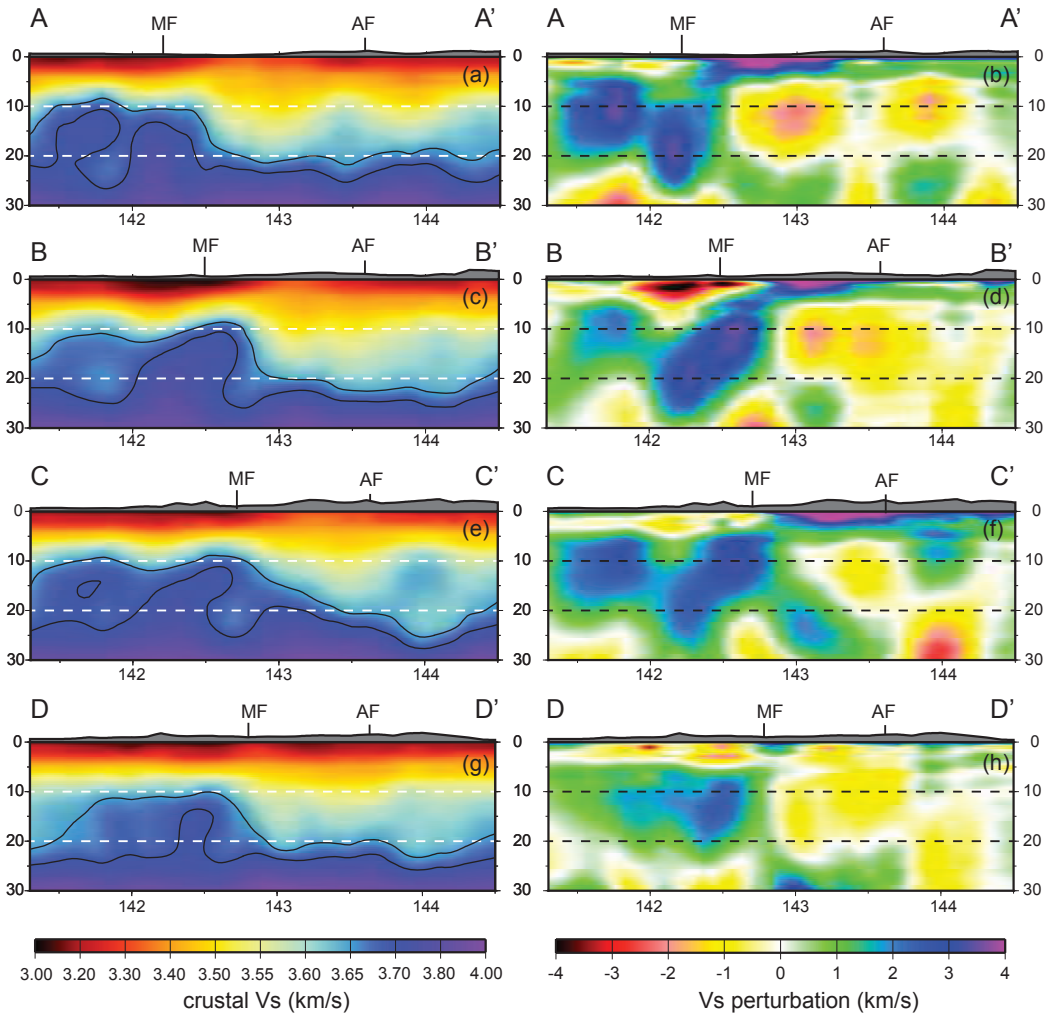

FIGURE 5.7: Transects of the Vs model plotted as both absolute velocities (a, c, e and g) and perturbations to regional average (b, d, f and h) along the four lines marked in Fig. 5.6a. Contours in a, c, e and g denote velocities of 3.65 and 3.7 km/s. All depths are relative to sea-level. The topography along the transects is also plotted on the top of the velocity distributions. MF: Moyston Fault; AF: Avoca Fault.

5.7 Discussion

5.7.1 Crustal tectonic settings of the NVP

Previous seismic tomography studies [Graeber *et al.* (2002); Rawlinson & Fishwick (2012); Rawlinson *et al.* (2014b)] image heterogeneous mantle lithosphere in the neighborhood of the NVP region, with relatively thicker Proterozoic continental lithosphere underlying the DO [Cayley *et al.* (2011)] and much thinner and probably transitional lithosphere beneath the westernmost of the LO [Cayley *et al.* (2011); Pilia *et al.* (2015a)] (Fig. 5.9a). These complex lithospheric structures may reflect the long-lived subduction-accretion processes that occurred along the former margin of East Gondwana from the Late Proterozoic to the Early Mesozoic, as modeled by a recent geodynamic study [Moresi *et al.* (2014)]. Such processes probably have played a significant role during the growth of the entire eastern third of the Australian continent [Foster & Gray (2000); Glen (2005)] (known as the Tasmanides), as demonstrated by the frozen-in deformation fabric in the crust [Rawlinson *et al.* (2014a)]. According to the geological study of Glen (2005), the DO and LO represent the first two phases of such accretionary process. The velocity model from this study confirms that significant variations in crustal structure coincide with the inferred location of the boundary between the DO and LO at the surface.

At shallow depths, prominent low velocities are mostly seen to the west of the MF, which can be attributed to the presence of sediments. In particular, the circular low-velocity anomaly just west of the MF corresponds to a relatively small Silurian basin [Miller *et al.* (2005)]. In the east, exceptionally high velocity anomalies, which are more than 3% in amplitude at 3 km depth but decrease to 1-2% at 5 km, are observed across most of the regions north of the NVP. Many of these high velocities coincident with the surface exposure of Devonian granites [Cayley *et al.* (2011); Chappell *et al.* (1988)], and thus probably representing large bodies of crystallized igneous rocks. In particular, the high velocity anomalies elongated along the MF are coincident with the geographic locations of the geological unit of Moornambool metamorphic complex (MMC) [Cayley & Taylor (2001)], which is an amphibolite metamorphic domain. The high-grade metamorphism of the complex is suggested

to document 15-20 km vertical offset along the MF [Phillips *et al.* (2002); Taylor & Cayley (2000)] in the early Cambrian [Miller *et al.* (2005)]. Thus, our velocity structure is consistent with the geological interpretation that the MF may act as an important boundary fault during the early accretion of the Tasmanides.

At 10 and 15 km depths (Fig. 5.6c-d), high velocities dominate the region west of the MF, and are separated from the low velocities in the east. The interpolated surface heat flow in Victoria state based on numerical modelling from the study of Mather *et al.* (2015) (Fig. 5.8a) displays an average surface heat flow of 50-60 mW/m^2 for the region located west of the MF, and they are 20-30 mW/m^2 lower than that in the east of the MF. If we assume rock compositions are similar on the two sides of the fault and the heat production only arises from the lithospheric conduction, the differences of the surface heat flow on the two sides of MF would imply a thermal gradient ratio around 1:1.6 based on the heat flux equation. This thermal gradient difference would result in temperature difference less than 250 °C at the depth of 15 km, if we assure a thermal gradient of 25 °C/km for the region east of the MF, which is close to the averaged thermal gradient in the western Victoria according to Purss & Cull (2001). The experimental study of Kern *et al.* (2001) demonstrates that a 100 °C temperature increase would lower the shear velocities of the typical crust rock of gneisses by ∼20 m/s, which is less than 1% if considering an averaged shear velocity of 3.5 km/s in the crust. The <250 °C temperature difference in the mid crust is unlikely to generate the 4-6% velocity differences across the MF as we observed in this study.

The large velocity differences, thus, may imply significant variations in composition, which is also consistent with the observation of strong positive Bouguer anomaly in the DO (Fig. 5.8b), suggesting denser rocks in the crust beneath the DO than that beneath LO. A series of geological studies have identified volcanic rocks of arc affinities in the DO [VandenBerg *et al.* (2000); Crawford *et al.* (2003)], as represented by the Mount Stavely andesite, whose geochemical signatures are indicative of subduction [Whelan *et al.* (2007)]. Meanwhile, high reflective package in the mid crust based on the seismic reflection data are interpreted to be the buried andesite rocks [Cayley *et al.* (2011); Robertson *et al.* (2015)]. Therefore, based on the above information, we propose the pronounced high velocities observed in the mid crust probably reflect the buried magmatic arcs as results of subduction. And our velocity

model supports the tectonic scenario that the Delamerian orogeny is associated with westward subduction during the early Paleozoic, as proposed by series of geological studies, such as John *et al.* (2006) and Turner *et al.* (1996). The region east of the MF, however, is mostly underlain by juvenile lithosphere covered by deep sea sediments, in contrast to the Palaeozoic substrate of the DO [Gray & Foster (1998); Kemp *et al.* (2009); Taylor & Cayley (2000)].

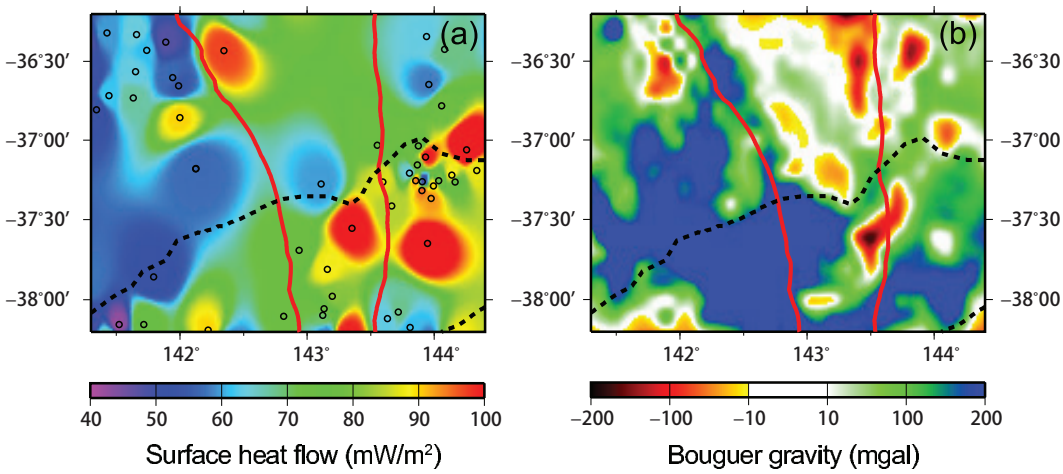

Figure 5.8: (a) Measured (black circles) and interpolated distributions of the surface heat flow in the region according to Mather *et al.* (2015), in which the local geology is incorporated in the interpolation of the measured surface heat flow. (b) The Bouguer gravity field in the region. The thick red lines denote the Moyston Fault (left) and Avoca Fault (right). The dashed thick black line denotes the geographic boundaries of the erupted magmas.

5.7.2 Crustal magmatic systems beneath the NVP

The velocity model from this study, covering the central region of the eruption sites, provides snapshots of the current and arguably still-active crustal magmatic systems beneath the NVP, the most recent intraplate volcanism on the Australian continent.

Based on our velocity model, the upper crust beneath the NVP does not exhibit any strong negative velocity anomalies that could be readily associated with a magmatic plumbing system. The most prominent feature observed beneath the NVP that could be associated with volcanism at the surface is the appearance of a relatively concentrated region of low velocities in the mid/lower crust (Fig. 5.6f), spatially close to the surface expression of large faults, such as the one along the middle segment of the MF and the one located in the east

of the AF. At 25 km depth, the amplitude of the velocity reduction is 1-2%, and it increases to ∼3% in the lower crust. The surface heat flow at these two regions of low velocities [Mather *et al.* (2015)] are not significantly different (Fig. 5.8a), implying temperature differences may be not the only contributor to the low velocities. The strong negative velocity anomalies are likely to be caused also by variations in composition and/or the presence of partial melt. We think the latter explanation is more consistent with interpretations based on recent images of the electrical structure, as described below.

A magnetotelluric (MT) survey [Aivazpourporgou *et al.* (2015)] identifies a low-resistivity zone of 10-30 Ωm, which extends from the bottom of the lower crust to depths of ∼90 km beneath the surface projection of the AF. The top of this low-resistivity zone is spatially coincident with the low velocity bodies seen in our velocity model. This low-resistivity zone is interpreted to contain 1.5-4% partial melt based on the absolute resistivity values and the P/T conditions as constrained by mantle xenoliths [O'Relly & Griffin (1985)], and it is further argued that the melts are most likely to originate from the decompression melting of the asthenosphere beneath a locally thin lithosphere [Davies & Rawlinson (2014)]. Translithospheric faults in the region [Cayley *et al.* (2011)] (Fig. 5.9a) may provide pathways for melt migration, allowing some of the inferred melts in the upper lithospheric mantle to reach and accumulate in the lower crust. The electronic structures from Aivazpourporgou *et al.* (2015) also display signatures of melt intrusion from the upper mantle into the lower crust in the regions close to our low velocity anomaly. The observed velocity reduction in the lower crust is very likely the result of small accumulation of partial melt. ∼1% melt is sufficient to cause the velocity reduction, even considering the smallest wetting angles between crystal boundaries [Takei (2000); Caldwell *et al.* (2009)]. The small volume of melt does not indicate a significant magma body in the lower crust. Instead, the melts may have intruded and accumulated in the lower crust to form sills and dykes (Fig. 5.9b), which have been widely observed beneath volcanic regions [e.g. Gudmundsson (2011); Jaxybulatov *et al.* (2014); Shervais *et al.* (2006)], and also suggested by numerical modelling [Annen *et al.* (2005)]. Seismic radial anisotropy can be a good indicator for the horizontal layering of the sills, as demonstrated in a recent study [Jaxybulatov *et al.* (2014)]. However, the availability of only vertical component data means that this is not currently possible.

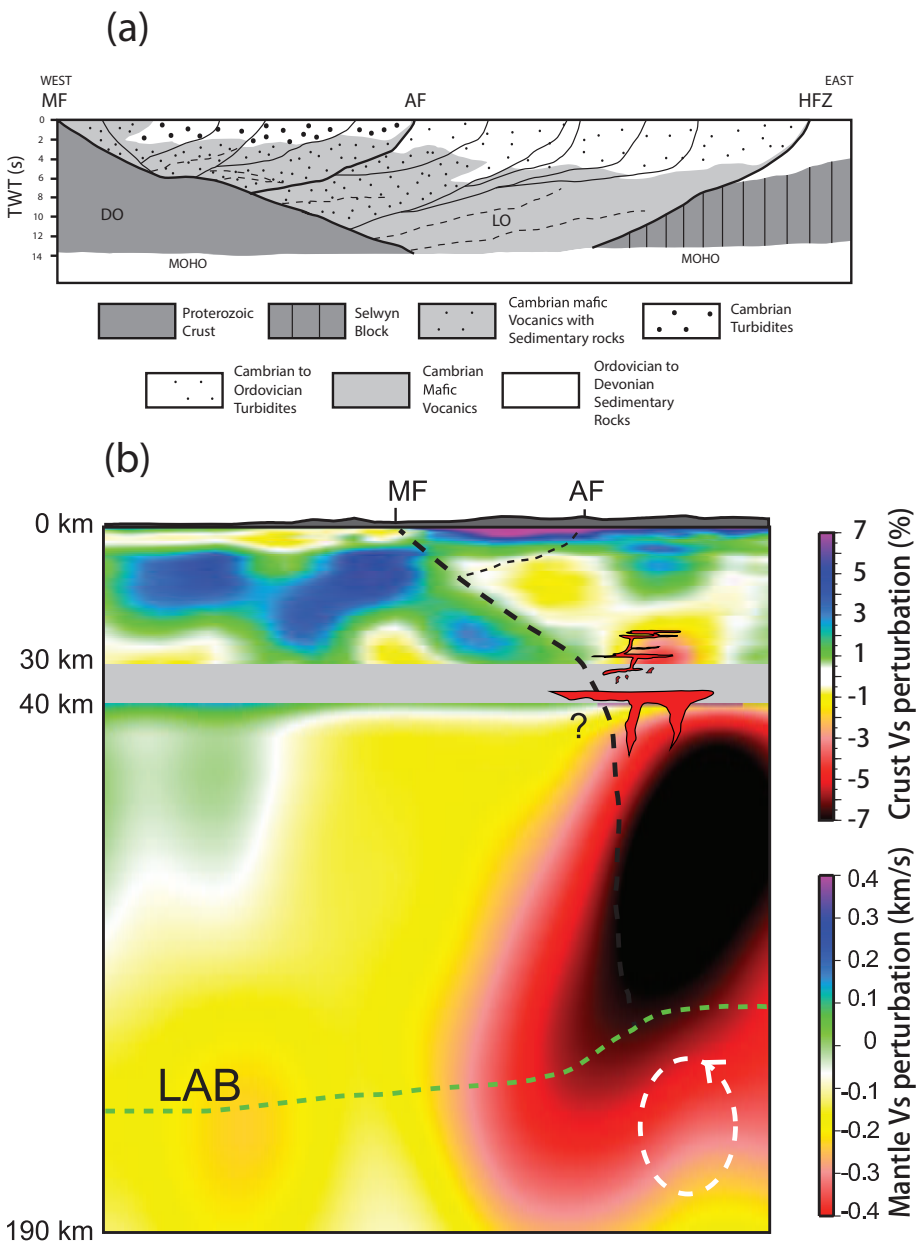

Figure 5.9: (a) The interpreted seismic reflection profile from Cayley *et al.* (2011) along the line shown in Fig. 5.1. (b) A cartoon to illustrate the accumulated magmatic intrusion in the lower crust beneath the NVP and its connection with the deep lithosphere. The crustal Vs perturbation is relative to the regional average from this study (0-30 km; vertical exaggeration twice that of the mantle part); while the mantle Vs perturbation is relative to the ak135 model [Kennett *et al.* (1995)] in km/s from Rawlinson *et al.* (2015) (40-190 km). The white circle illustrates the edge-driven convection from the geodynamic model of Davies & Rawlinson (2014). The shaded area on the top of the section represents the topography, the Moho depth is from the Australian Moho model of Salmon *et al.* (2013b), and the depth of the LAB (Lithosphere-Asthenosphere boundary) is an approximated illustration based on the study of Davies & Rawlinson (2014). MF: Moyston Fault; AF: Avoca Fault.

The inferred melts in the deep crust beneath the NVP could represent the remnants of magma from the main eruption periods. Alternatively, they could be caused by the accumulation of newly generated magma. However, the geochemical features of the erupted magmas in the region indicate that the latter interpretation is more plausible. The primitive geochemical signatures of the erupted basalts [McDonough *et al.* (1985)] and their cargo of mantle-derived xenoliths [Griffin *et al.* (1984); McBride *et al.* (1996)] suggest that the magmas experienced a rapid transit from the mantle to the surface. Based on the petrological constraints [O'Reilly & Griffin (2010)], the magma must ascend rapidly from the lithosphere to prevent the densely entrained xenoliths from sinking. The overall time for the migration of the magma is estimated to be on the order of a few days [O'Reilly & Griffin (2010)], which is consistent with the geochemical evidence suggesting that the magmas of the NVP have experienced little crustal assimilation [O'Reilly & Griffin (1984); Van Otterloo *et al.* (2014)]. Therefore, most of the magmas should have migrated to the surface during the main time of eruptions. However, if we assume that edge-driven convection combined with shear flow are the main driving mechanisms [Davies & Rawlinson (2014)], the conditions for generating intraplate volcanism in the NVP are still active, and the accumulated melts may represent another cycle of long-term incremental evolution toward large magma eruptions [Jaxybulatov *et al.* (2014)].

Though the surface exposure of the erupted NVP covers a region of >19000 km^2 [Boyce (2013)], the thickness of the basaltic plains is mostly <60 m, which implies a low total eruption volume [Johnson (1989)]. The low erupted volume and the relatively small magmatic intrusion imaged in the lower crust indicate that the melt production of the NVP is much smaller compared to other large basaltic volcanoes, such as Yellowstone, where a large crustal magmatic plumbing system has been imaged [Huang *et al.* (2015)].

5.8 Conclusion

In this study, we collect ambient noise data from 40 seismic stations in the NVP region to construct a 3D crustal Vs model with an average horizontal resolution of 35 km. In this model, large velocity differences are observed in the upper and mid crust of the DO and LO,

with the boundary between them correlated with the trans-lithospheric MF. Our velocity models together with the interpretations based on seismic reflection data, geochemical signatures and the gravity field, is consistent with the model that a buried magmatic arc is situated beneath the DO and the Delamerian orogeny is associated with subduction during the early Paleozoic. Beneath the NVP, no large concentrated low velocities are observed in the upper and middle crust, but narrow vertically-continuous regions of low velocity are present in the lower crust. These low velocity anomalies are spatially coincident with the top of a prominent low-resistivity zone (10-30 Ωm), which is interpreted to be a zone of magmatic intrusion with around 1% of melt. The small size of the magmatic intrusion and the minor eruption volume indicate a much smaller magmatic plumbing system beneath NVP compared to other intraplate basaltic provinces such as Yellowstone.

6

Conclusions

This thesis uses ambient noise tomography to image three orogenic belts covered by dense seismic arrays. These regions are the northeast Tibetan Plateau, the Qinling Orogen and its adjacent regions, and the Delamerian orogen and the associated Newer Volcanics Province. The ultimate aim of this thesis is to use the constructed velocity models to study regional tectonic evolution, i.e., the orogenic processes in these areas. This objective is achieved via the integration of the highly resolved crustal-velocity model for each region with evidence from geological, geochemical and other geophysical studies. And the major conclusion of this thesis is that this approach provides a better understanding of mountain-building processes in orogenic belts. Before summarising the conclusion for each chapter, we synthesise the main outcomes of this thesis, both on shear wave velocity interpretations and the technical advantages of ambient noise tomography.

6.1 Shear wave velocity interpretations

Shear wave velocities in the crust depend on a variety of parameters such as temperature, rock compositions and the presence of melts or fluids. Therefore, shear velocities cannot be straightforwardly linked to either one or a combination of these parameters. However, similar amplitude of seismic anomalies under the same tectonic setting, such as orogenic belts that are investigated in this thesis, may share some common origins. For example, the temperature differences within old inactive orogenic belts may be minor due to a prolonged time of cooling, and the intrusive melts associated with the orogeny probably have also crystalized. Under such conditions, the rock compositions will become the main contributor to the velocity variations. In general, sedimentary or low-grade metamorphic rocks will result in relatively low velocities compared to igneous or high-grade metamorphic rocks. This is shown in the crustal structures around the Dabashan Orocline (Chapter 3), where crustal-scale high-velocity bodies beneath the HNMC and SNHL Domes are interpreted to represent intrusive complexes and associated uplifted basement rocks; while the relatively low velocities observed beneath the Dabashan Orocline between the two domes probably represent meta-sedimentary sequences.

In young active orogenic belts that are associated with interactions with the lithosphere such as lithosphere upwelling, considerable amounts of heat from the mantle would significantly increase the temperature in the crust and are therefore likely to result in the generation of crustal melts, causing dramatic seismic low velocities [Takei (2000); Watanabe (1993)]. One particular example of seismic low velocities under this tectonic setting condition is the low velocity zones (LVZs) identified in the mid/lower crust of the NE Tibetan Plateau (Chapter 2). The wide-spread low velocities together with the feature of high conductivities imply the existence of partial melting in the mid/lower crust. As suggested by Beaumont *et al.* (2001), the presence of partial melts would decrease the strength and the effective viscosity of the crustal rocks by several orders of magnitude, thereby contributing to a partially molten layer that is weaker than the domains above and below. Driven by horizontal pressure gradients between the plateau and its adjacent foreland, the weak crustal layer may tend to flow, thus leading to the processes of mid/lower crustal channel flow [Clark

& Royden (2000); Klemperer (2006); Royden *et al.* (1997); Searle *et al.* (2011)].

Another example of crustal low velocities caused by the presence of melts from this thesis is around the Newer Volcanics Province in SE Australia (Chapter 5). The narrow vertically-continuous regions of low velocity in the lower crust, which are spatially coincident with the top of a prominent low-resistivity zone (10-30 Ωm), are interpreted to be magmatic intrusions from the lithospheric mantle with around 1% of melt. However, it should be noted that although the presence of partial melt would significantly lower shear velocities, the non-linear and complicated relations between seismic velocities and other physical parameters make it hard to infer the presence and the amount of partial melts based on seismic velocity alone. In order to do so, one needs to couple the velocity distribution with other geophysical and geochemical evidences such as magnetotelluric sounding, geochemical signatures from xenoliths and petrological modelling, as we have done in Chapter 2 and 5.

6.2 Advantages of ambient noise tomography

In this thesis, I employ the tomography method of Barmin *et al.* (2001) in Chapter 2 and 3, the eikonal tomography method of Rawlinson & Sambridge (2003) in Chapter 4 and the eikonal tomography of Lin *et al.* (2009) in Chapter 5. The adopted surface wave tomography methods are based on the ray theory, which may neglect wavefield complexities caused by surface waves propagation through inhomogeneous medium. Typical examples of such wavefiled complexities include ray bending [Lin *et al.* (2009); Yao *et al.* (2006)] and the finite frequency effect of wave front healing [Hung *et al.* (2001); Malcolm & Trampert (2011)]. However, it is found that the main dispersion interests of this thesis and the tomographic techniques adopted in the case studies are able to mitigate these issues, as addressed in details below.

At sharp velocity boundaries, seismic rays will deviate from the great-circle path; a phenomenon called off-great circle propagation [Cotte *et al.* (2000); Yang *et al.* (2007)]. Due to the longer distances of the ray path caused by ray bending compared to that along the great-circle propagation, ray bending will commonly result in underestimation of seismic velocities in the tomography [Yao *et al.* (2006)]. However, Ritzwoller & Levshin (1998) found

that ray bending effects can be largely ignored at periods above 30 s with ray path length less than 5000 km within the continental interiors. In respect of the ambient noise tomography, Lin *et al.* (2009) suggested that the off-great circle propagation have little effects on the tomography for periods longer than 20 s, which are the main dispersion interests for the case studies in Chapter 2, 3 and 4. Consequently, the tomography in these studies will suffer little from the off-great circle propagation effects. Probably the only case study that could be largely affected by such effect is the one in Chapter 5, where significant velocity variations are revealed at 2-18 s periods around the Newer Volcanics Province. However, the eikonal tomography adopted in this chapter [Rawlinson & Sambridge (2003)] uses a finite-difference method to solve the eikonal equation and computes 2D travel time fields on a spherical shell. It enables the tracking of wave fronts in heterogeneous media, and thereby modelling the off-great circle wave propagation [Lin & Ritzwoller (2011a); Ritzwoller *et al.* (2011)].

Different from the off-great circle propagation effects, the wavefront healing tends to "heal seismic low velocities, making it difficult to recover small scale low velocities along seismic rays [Wielandt (1987)]. It is also found that wavefront healing effect can place complexities on the amplitude recovery of velocity anomalies [Hung *et al.* (2001); Malcolm & Trampert (2011); Nolet & Dahlen (2000)]. The finite-frequency effect is suggested to be most prominent when the wavelength of a wave is comparable to or greater than the scale of heterogeneity [Hung *et al.* (2001)], and is particularly important for teleseismic tomography studies [Yang & Forsyth (2006); Yoshizawa & Kennett (2002); Zhou *et al.* (2004)] due to the relatively long periods, wavelengths and path lengths involved [Lin & Ritzwoller (2010)]. However, Ritzwoller *et al.* (2002) demonstrated that inversion using ray theory with Gaussian sensitivity functions can result in similar structures in continental regions to that based on diffraction tomography method at periods shorter than 50 s.

In this thesis, the tomography method of Barmin *et al.* (2001) employed in Chapter 2 and 3 is built on straight ray theory with Gaussian sensitivity functions. Therefore, this method is able to deal with the wavefront healing effects in the two case studies. Meanwhile, due to the fact that the wavefield dealt in the ambient noise tomography is free from effects external to the seismic array [Ritzwoller *et al.* (2011)], a series of studies indicated that the finite frequency effects can be negligible for ambient noise tomography at periods shorter than 50

s [Lin & Ritzwoller (2011b); Lin *et al.* (2009); Ritzwoller *et al.* (2011)]. These arguments together suggest that ray-theory can adequately model surface wave propagation at periods below 50 s [Bensen (2007)], thereby justifying the usage of ray theory based ambient noise tomography method in this thesis. It also insures the reliability of the crustal structures derived from these methods, based on which further geological interpretations are made.

6.3 Summary and future work

On the basis of the above two main outcomes, the crustal velocity model for each orogenic belt examined in this thesis should be robust, which reveals important features closely related to the geological history of the belt, as summarised here.

In Chapter 2, the 3-D Vsv model with a resolution of 30-50 km in the NE Tibetan Plateau and surrounding regions reveals strong LVZs in the middle crust across the region. In particular, the model shows significant variations of the lateral distribution of LVZs from west to east along the Kunlun Fault. West of 98 $^\circ E$, LVZs are confined to regions of the Kunlun Fault and the eastern Kunlun Range but are absent beneath the Qaidam Basin;. However, east of 98 $^\circ E$, the LVZs extend beyond the Kunlun Fault and penetrate over $\sim$100 km northward into the Qinling Orogen. Regions with strong LVZs coincide with the regions with strong mid-crustal radial anisotropy [Xie *et al.* (2013)], which can be explained by mid-crustal channel flow aided by a partially melted mica-bearing mid/lower crustal layer [Hacker *et al.* (2014)]. Our 3-D model clearly delineates the northward extent of the mid-crustal LVZs, probably reflecting the current status of channel flow in the NE Tibetan Plateau.

In Chapter 3, the 3-D Vs model with a lateral resolution of 60-70 km in the Qinling Orogen and its adjacent regions exhibits strong crustal heterogeneity. In particular, crustal scale high-velocity bodies are seen beneath the HNMC and SNHL Domes, probably representing intrusive complexes and associated uplifted basement rocks, reflecting initial intrusion and later strong crustal shortening. Extensive high-velocity volumes are also observed in the segment of 106 $^\circ E$-108 $^\circ E$ of the Qinling Orogen, which reflect the connected batholiths of the Triassic granites at shallow depths and possible mafic materials in the mid/deep crust, based on their geochemical signatures. The crustal-scale bodies with high velocity and high

Poisson's ratio beneath the two domes and the western Qinling Orogen may represent mechanically strong rocks, which not only assisted the formation of the major Dabashan Orocline during the late Mesozoic intra-continental orogeny, but also impeded the northeastward expansion of the Tibetan Plateau during the Cenozoic era.

In Chapter 4, we investigate the azimuthal anisotropy in the same region as that of Chapter 3 as a complementary study to the isotropic velocity models. The model displays depth-dependent anisotropic features in the region. In particular, two layered structures are observed beneath the Qinling Orogen, Longmenshan and the NE Tibetan Plateau. In the Qinling Orogen, an orogen-parallel (E-W) fast direction is observed in the upper/mid crust, while an orogen-perpendicular (N-S) fast direction is seen in the deep crust and uppermost mantle. The two-layered anisotropic feature suggests a mountain-building process similar to that of the Taiwan orogen [Huang et al., 2015], where a transitional ductile regime in the lower crust serves to compensate the brittle deformation in the upper/mid crust, and the subduction in the upper mantle. However, in the Longmenshan, the anisotropic pattern relative to the orogenic geometry is completely reversed. The upper crust beneath the orogen is dominated by orogen-perpendicular fast directions, whereas the mid/lower crust displays orogen-parallel fast directions. This suggests that the anisotropy in the upper crust may be related to the fractures of dominant faults and those in the mid/lower crust represent the combined effects of horizontal shortening and vertical ductile deformation. Strong NE-SW oriented anisotropy is also imaged in the mid/lower crust of the NE Tibetan Plateau, whose distribution is coincident with the presence of LVZs. This structure is interpreted to represent a separate channelized flow, developed as a response of the barrier of the Sichuan basin to the plateau's eastward extrusion.

Chapter 5 presents a 3D crustal Vs model of the Newer Volcanics Province of SE Australia with an average horizontal resolution of 35 km. This model reveals large velocity differences in the upper and middle crust of the Delamerian Orogen and Lachlan Orogen, with the boundary between them correlating well with the trans-lithospheric Moyston Fault. The velocity model, together with seismic reflection results, geochemical signatures and the gravity field, suggest the existence of a buried magmatic arc situated above Proterozoic continental lithosphere in the Delamerian Orogen, in contrast to the possible juvenile lithosphere

beneath the Lachlan Orogen. Beneath the NVP, vertically-continuous narrow regions of low velocity are present in the lower crust, which are spatially coincident with the top of a prominent low-resistivity zone (10-30 Ωm). We interpret this anomaly as a magmatic intrusion with around 1% of melt. The small size of the magmatic intrusion and the minor eruption volume indicate a much smaller magmatic plumbing system beneath NVP compared to other intraplate basaltic provinces such as Yellowstone.

The four case studies demonstrate the advantages of ambient noise tomography as a tool for the study of regional crustal structures, especially in orogenic belts. However, the crustal velocity models constructed in the thesis have three apparent limitations: 1) discontinuities such as the base of the sedimentary layer and the Moho cannot be resolved and thus are strongly dependent on the starting model; 2) the exact depth extent of the azimuthal anisotropy at each period (Chapter 4) is not resolved; 3) long-period surface wave information should be combined with short-intermediate ones in order to make more comprehensive understandings of the crust-upper mantle system in orogenic belts. The first limitation may lead to slightly biased velocities at depths right above/beneath the boundaries due to the trade-off between absolute velocities and the depth of discontinuities if the chosen starting model is not accurate enough. This problem can be reconciled in a framework of joint inversion combining surface wave dispersion curves with receiver functions. The second limitation points to the key fact that the anisotropic features at each period represent structures integrated over a certain depth range. This limitation can be overcome by inverting the anisotropic features at each period for depth-dependent anisotropic structures in a Monte-Carlo framework. The third limitation requires the dispersion information from long-period surface waves, which can be either extracted from earthquake data or continuous ambient noise data. All of these limitations will certainly be addressed in my future studies.

References

Afonso, J. C., Fullea, J., Yang, Y., Connolly, J. A. D., & Jones, A. G. 2013a. 3-D multi-observable probabilistic inversion for the compositional and thermal structure of the lithosphere and upper mantle. II: General methodology and resolution analysis. *Journal of Geophysical Research: Solid Earth*, **118**(4), 1650–1676.

Afonso, J. C., Fullea, J., Griffin, W. L., Yang, Y., Jones, A. G., D. Connolly, J. A., & O'Reilly, S. Y. 2013b. 3-D multiobservable probabilistic inversion for the compositional and thermal structure of the lithosphere and upper mantle. I: a priori petrological information and geophysical observables. *Journal of Geophysical Research: Solid Earth*, **118**(5), 2586–2617.

Agostinetti, N. Piana, & Malinverno, A. 2010. Receiver function inversion by trans-dimensional Monte Carlo sampling. *Geophysical Journal International*, **181**(2), 858–872.

Aitken, A. R. A., Salmon, M. L., & Kennett, B. L. N. 2013. Australia's Moho: A test of the usefulness of gravity modelling for the determination of Moho depth. *Tectonophysics*, **609**, 468–479.

Aivazpourporgou, Sahereh, Thiel, Stephan, Hayman, Patrick C., Moresi, Louis N., & Heinson, Graham. 2015. Decompression melting driving intraplate volcanism in Australia: Evidence from magnetotelluric sounding. *Geophysical Research Letters*, **42**(2), 346–354.

Aki, Keiiti. 1957. Space and Time Spectra of Stationary Stochastic Waves, with Special Reference to Microtremors. *Bull. Earthq. Res. Inst.*, **35**(3), 415–456.

Alsdorf, Doug, & Nelson, Doug. 1999. Tibetan satellite magnetic low: Evidence for widespread melt in the Tibetan crust? *Geology*, **27**(10), 943–946.

Ames, Leslie, Tilton, George R., & Zhou, Gaozhi. 1993. Timing of collision of the Sino-Korean and Yangtse cratons: U-Pb zircon dating of coesite-bearing eclogites. *Geology*, **21**(4), 339–342.

An, Meijian, & Assumpcao, Marcelo S. 2004. Multi-objective inversion of surface waves and receiver functions by competent genetic algorithm applied to the crustal structure of the Paran Basin, SE Brazil. *Geophysical Research Letters*, **31**(5).

Annen, C., Blundy, J. D., & Sparks, R. S. 2005. The Genesis of Intermediate and Silicic Magmas in Deep Crustal Hot Zones. *Journal of Petrology*, **47**(3), 505–539.

Arroucau, P., Rawlinson, N., & Sambridge, M. 2010. New insight into Cainozoic sedimentary basins and Palaeozoic suture zones in southeast Australia from ambient noise surface wave tomography. *Geophysical Research Letters*, **37**(L07303).

Avouac, J. P., & Tapponnier, P. 1993. Kinematic Model of Active Deformation in Central-Asia. *Geophysical Research Letters*, **20**(10), 895–898.

Bai, D. H., Unsworth, M. J., Meju, M. A., Ma, X. B., Teng, J. W., Kong, X. R., Sun, Y., Sun, J., Wang, L. F., Jiang, C. S., Zhao, C. P., Xiao, P. F., & Liu, M. 2010. Crustal deformation of the eastern Tibetan plateau revealed by magnetotelluric imaging. *Nature Geoscience*, **3**(5), 358–362.

Bannister, S., Yu, J., Leitner, B., & Kennett, B. L. N. 2003. Variations in crustal structure across the transition from West to East Antarctica, Southern Victoria Land. *Geophysical Journal International*, **155**(3), 870–880.

Bao, X. W., Song, X. D., Xu, M. J., Wang, L. S., Sun, X. X., Mi, N., Yu, D. Y., & Li, H. 2013. Crust and upper mantle structure of the North China Craton and the NE Tibetan Plateau and its tectonic implications. *Earth and Planetary Science Letters*, **369**, 129–137.

Bao, Xuewei, Song, Xiaodong, & Li, Jiangtao. 2015. High-resolution lithospheric structure beneath Mainland China from ambient noise and earthquake surface-wave tomography. *Earth and Planetary Science Letters*, **417**, 132–141.

Barmin, M. P., Ritzwoller, M. H., & Levshin, A. L. 2001. A fast and reliable method for surface wave tomography. *Pure and Applied Geophysics*, **158**(8), 1351–1375.

Bassin, C, Laske, G, & Masters, G. 2000. The current limits of resolution for surface wave tomography in North America. *Eos Trans AGU*, **81**(48), Abstract S12A–03.

Beaumont, C., Jamieson, R. A., Nguyen, M. H., & Lee, B. 2001. Himalayan tectonics explained by extrusion of a low-viscosity crustal channel coupled to focused surface denudation. *Nature*, **414**(6865), 738–742.

Beaumont, C., Nguyen, M. H., Jamieson, R. A., & Ellis, S. 2006. Crustal flow modes in large hot orogens. *Geological Society, London, Special Publications*, **268**(1), 91–145.

Bensen, G. D. 2007. *Broad-band ambient noise surface wave tomography: technique development and application across the United States*. Ph.D. thesis.

Bensen, G. D., Ritzwoller, M. H., Barmin, M. P., Levshin, A. L., Lin, F., Moschetti, M. P., Shapiro, N. M., & Yang, Y. 2007. Processing seismic ambient noise data to obtain reliable broad-band surface wave dispersion measurements. *Geophysical Journal International*, **169**(3), 1239–1260.

Bensen, G. D., Ritzwoller, M. H., & Shapiro, N. M. 2008. Broadband ambient noise surface wave tomography across the United States. *Journal of Geophysical Research: Solid Earth*, **113**(B5), B05306.

Bodin, Thomas, Sambridge, Malcolm, Rawlinson, Nick, & Arroucau, Pierre. 2012. Transdimensional tomography with unknown data noise. *Geophysical Journal International*, **189**(3), 1536–1556.

Boyce, J. 2013. The Newer Volcanics Province of southeastern Australia: a new classification

scheme and distribution map for eruption centres. *Australian Journal of Earth Sciences*, **60**(4), 449–462.

Brocher, T. M. 2005. Empirical Relations between Elastic Wavespeeds and Density in the Earth's Crust. *Bulletin of the Seismological Society of America*, **95**(6), 2081–2092.

Brocher, Thomas M., & Christensen, Nikolas I. 1990. Seismic anisotropy due to preferred mineral orientation observed in shallow crustal rocks in southern Alaska. *Geology*, **18**(8), 737–740.

Burchfiel, B. C., Zhiliang, Chen, Yupinc, Liu, & Royden, L. H. 1995. Tectonics of the Longmen Shan and Adjacent Regions, Central China. *International Geology Review*, **37**(8), 661–735.

Burchfiel, B. C., Royden, L. H., van der Hilst, R. D., Hager, B.H., Chen, Z., King, R. W., Li, C., Yao, H. J., & Kirby, E. 2008. A geological and geophysical context for the Wenchuan earthquake of 12 May 2008, Sichuan, Peoples Republic of China. *GSA Today*, **18**(7), 5.

Caldwell, Warren B., Klemperer, Simon L., Rai, Shyam S., & Lawrence, Jesse F. 2009. Partial melt in the upper-middle crust of the northwest Himalaya revealed by Rayleigh wave dispersion. *Tectonophysics*, **477**, 58–65.

Cayley, R. A., Korsch, R. J., Moore, D. H., Costelloe, R. D., Nakamura, A., Willman, C. E., Rawling, T. J., Morand, V. J., Skladzien, P. B., & O'Shea, P. J. 2011. Crustal architecture of central Victoria: results from the 2006 deep crustal reflection seismic survey. *Australian Journal of Earth Sciences*, **58**(2), 113–156.

Cayley, RA, & Taylor, DH. 2001. Geological survey report for the Ararat 1:100000 map sheet. *Geological Survey of Victoria Report*, **121**.

Chappell, B. W., White, A. J. R., & Hine, R. 1988. Granite provinces and basement terranes in the Lachlan Fold Belt, southeastern Australia. *Australian Journal of Earth Sciences*, **35**(4), 505–521.

Chen, Min, Huang, Hui, Yao, Huajian, van der Hilst, Rob, & Niu, Fenglin. 2014. Low wave speed zones in the crust beneath SE Tibet revealed by ambient noise adjoint tomography. *Geophysical Research Letters*, **41**(2), 334–340.

Chen, Min, Niu, Fenglin, Liu, Qinya, Tromp, Jeroen, & Zheng, Xiufen. 2015. Multiparameter adjoint tomography of the crust and upper mantle beneath East Asia: 1. Model construction and comparisons. *Journal of Geophysical Research: Solid Earth*, **120**(3), 1762–1786.

Christensen, N. I. 1996. Poisson's ratio and crustal seismology. *Journal of Geophysical Research: Solid Earth*, **101**(B2), 3139–3156.

Christensen, N. I., & Mooney, W. D. 1995. Seismic Velocity Structure and Composition of the Continental-Crust - a Global View. *Journal of Geophysical Research: Solid Earth*, **100**(B6), 9761–9788.

Christensen, Nikolas I. 1965. Compressional wave velocities in metamorphic rocks at pressures to 10 kilobars. *Journal of Geophysical Research*, **70**(24), 6147–6164.

Chung, S. L., Chu, M. F., Zhang, Y. Q., Xie, Y. W., Lo, C. H., Lee, T. Y., Lan, C. Y., Li, X. H., Zhang, Q., & Wang, Y. Z. 2005. Tibetan tectonic evolution inferred from spatial and temporal variations in post-collisional magmatism. *Earth-Science Reviews*, **68**(3-4), 173–196.

Clark, M. K., & Royden, L. H. 2000. Topographic ooze: Building the eastern margin of Tibet by lower crustal flow. *Geology*, **28**(8), 703–706.

Clitheroe, G., Gudmundsson, O., & Kennett, B. L. N. 2000. The crustal thickness of Australia. *Journal of Geophysical Research: Solid Earth*, **105**(B6), 13697–13713.

Conrad, Clinton P., Bianco, Todd A., Smith, Eugene I., & Wessel, Paul. 2011. Patterns of intraplate volcanism controlled by asthenospheric shear. *Nature Geoscience*, **4**(5), 317–321.

Cotte, N., Pedersen, H. A., Campillo, M., Farra, V., & Cansi, Y. 2000. Off-great-circle

propagation of intermediate-period surface waves observed on a dense array in the French Alps. *Geophysical Journal International*, **142**(3), 825–840.

Crampin, Stuart. 1984. Effective anisotropic elastic constants for wave propagation through cracked solids. *Geophysical Journal of the Royal Astronomical Society*, **76**(1), 135–145.

Crampin, Stuart. 1985. Evaluation of anisotropy by shear wave splitting. *Geophysics*, **50**(1), 142–152.

Crawford, AJ, Cayley, RA, Taylor, DH, Morand, VJ, Gray, CM, Kemp, AIS, Wohlt, KE, VandenBerg, AHM, Moore, DH, & Maher, S. 2003. *Neoproterozoic and Cambrian continental rifting, continent-arc collision and post-collisional magmatism.* Ph.D. thesis.

Davies, D. R., & Davies, J. H. 2009. Thermally-driven mantle plumes reconcile multiple hot-spot observations. *Earth and Planetary Science Letters*, **278**, 50–54.

Davies, D. R., Rawlinson, N., Iaffaldano, G., & Campbell, I. H. 2015. Lithospheric controls on magma composition along Earth's longest continental hotspot track. *Nature*, **525**(7570), 511–514.

Davies, D. Rhodri, & Rawlinson, Nicholas. 2014. On the origin of recent intraplate volcanism in Australia. *Geology*, **42**(12), 1031–1034.

Demidjuk, Zoe, Turner, Simon, Sandiford, Mike, George, Rhiannon, Foden, John, & Etheridge, Mike. 2007. U-series isotope and geodynamic constraints on mantle melting processes beneath the Newer Volcanic Province in South Australia. *Earth and Planetary Science Letters*, **261**, 517–533.

Deng, Yangfan, Shen, Weisen, Xu, Tao, & Ritzwoller, Michael H. 2015. Crustal layering in northeastern Tibet: a case study based on joint inversion of receiver functions and surface wave dispersion. *Geophysical Journal International*, **203**(1), 692–706.

Ding, L., Kapp, P., Yue, Y. H., & Lai, Q. Z. 2007. Postcollisional calc-alkaline lavas and xenoliths from the southern Qiangtang terrane, central Tibet. *Earth and Planetary Science Letters*, **254**(1-2), 28–38.

Dong, S., Gao, R., Yin, A., Guo, T., Zhang, Y., Hu, J., Li, J., Shi, W., & Li, Q. 2013. What drove continued continent-continent convergence after ocean closure? Insights from high-resolution seismic-reflection profiling across the Daba Shan in central China. *Geology*, **41**(6), 671–674.

Dong, Yunpeng, Zhang, Guowei, Neubauer, Franz, Liu, Xiaoming, Genser, Johann, & Hauzenberger, Christoph. 2011. Tectonic evolution of the Qinling orogen, China: Review and synthesis. *Journal of Asian Earth Sciences*, **41**(3), 213–237.

Dong, Yunpeng, Liu, Xiaoming, Zhang, Guowei, Chen, Qing, Zhang, Xiaoning, Li, Wei, & Yang, Chen. 2012. Triassic diorites and granitoids in the Foping area: Constraints on the conversion from subduction to collision in the Qinling orogen, China. *Journal of Asian Earth Sciences*, **47**, 123–142.

Dziewonski, A., Bloch, S., & Landisman, M. 1969. A technique for the analysis of transient seismic signals. *Bulletin of the Seismological Society of America*, **59**(1), 427–444.

Dziewonski, A. M., & Anderson, D. L. 1981. Preliminary Reference Earth Model. *Physics of the Earth and Planetary Interiors*, **25**(4), 297–356.

Einstein, A. 1905. The motion of elements suspended in static liquids as claimed in the molecular kinetic theory of heat. *Annalen der Physik*, **17**(8), 549–560.

Ekstrom, Goran, & Dziewonski, Adam M. 1998. The unique anisotropy of the Pacific upper mantle. *Nature*, **394**(6689), 168–172.

Ekstrom, Goran, Abers, Geoffrey A., & Webb, Spahr C. 2009. Determination of surface-wave phase velocities across USArray from noise and Aki's spectral formulation. *Geophysical Research Letters*, **36**(18).

England, P., & Houseman, G. 1986. Finite Strain Calculations of Continental Deformation .2. Comparison with the India-Asia Collision Zone. *Journal of Geophysical Research: Solid Earth and Planets*, **91**(B3), 3664–3676.

England, P., & Molnar, P. 1997. Active deformation of Asia: From kinematics to dynamics. *Science*, **278**(5338), 647–650.

Enkelmann, E., Ratschbacher, L., Jonckheere, R., Nestler, R., Fleischer, M., Gloaguen, R., Hacker, B. R., Zhang, Y. Q., & Ma, Y. S. 2006. Cenozoic exhumation and deformation of northeastern Tibet and the Qinling: Is Tibetan lower crustal flow diverging around the Sichuan Basin? *Geological Society of America Bulletin*, **118**(5-6), 651–671.

Fang, Hongjian, Yao, Huajian, Zhang, Haijiang, Huang, Yu-Chih, & van der Hilst, Robert D. 2015. Direct inversion of surface wave dispersion for three-dimensional shallow crustal structure based on ray tracing: methodology and application. *Geophysical Journal International*, **201**(3), 1251–1263.

Farrell, Jamie, Smith, Robert B, Husen, Stephan, & Diehl, Tobias. 2014. Tomography from 26 years of seismicity revealing that the spatial extent of the Yellowstone crustal magma reservoir extends well beyond the Yellowstone caldera. *Geophysical Research Letters*, **41**(9), 3068–3073.

Farrington, R. J., Stegman, D. R., Moresi, L. N., Sandiford, M., & May, D. A. 2010. Interactions of 3D mantle flow and continental lithosphere near passive margins. *Tectonophysics*, **483**, 20–28.

Forsyth, Donald W., Harmon, Nicholas, Scheirer, Daniel S., & Duncan, Robert A. 2006. Distribution of recent volcanism and the morphology of seamounts and ridges in the GLIMPSE study area: Implications for the lithospheric cracking hypothesis for the origin of intraplate, non-hot spot volcanic chains. *Journal of Geophysical Research: Solid Earth*, **111**(B11).

Foster, David A., & Gray, David R. 2000. Evolution and Structure of the Lachlan Fold Belt (Orogen) of Eastern Australia. *Annual Review of Earth and Planetary Sciences*, **28**(1), 47–80.

Fry, Bill, Deschamps, Frederic, Kissling, Edi, Stehly, Laurent, & Giardini, Domenico. 2010. Layered azimuthal anisotropy of Rayleigh wave phase velocities in the European Alpine

lithosphere inferred from ambient noise. *Earth and Planetary Science Letters*, **297**(1-2), 95–102.

Gao, Haiying, Humphreys, Eugene D., Yao, Huajian, & van der Hilst, Robert D. 2011. Crust and lithosphere structure of the northwestern U.S. with ambient noise tomography: Terrane accretion and Cascade arc development. *Earth and Planetary Science Letters*, **304**(1-2), 202–211.

Gao, S., Zhang, B.R., & Li, Z. J. 1990. Geochemical evidence for Proterozoic continental arc and continental-margin rift magmatism along the northern margin of the Yangtze Craton, South China. *Precambrian Research*, **47**(34), 205–221.

Gao, S., Zhang, B. R., Luo, T. C., Li, Z. J., Xie, Q. L., Gu, X. M., Zhang, H. F., Ouyang, J. P., Wang, D. P., & Gao, C. L. 1992. Chemical composition of the continental crust in Qinling orogenic belt and its adjacent North China and Yangtze cratons. *Geochimica et Cosmochimica Acta*, **56**.

Gao, Shan, Ling, Wenli, Qiu, Yumin, Lian, Zhou, Hartmann, Gerald, & Simon, Klaus. 1999. Contrasting geochemical and Sm-Nd isotopic compositions of Archean metasediments from the Kongling high-grade terrain of the Yangtze craton: evidence for cratonic evolution and redistribution of REE during crustal anatexis. *Geochimica et Cosmochimica Acta*, **63**, 2071–2088.

Gao, Stephen S., & Liu, Kelly H. 2009. Significant seismic anisotropy beneath the southern Lhasa Terrane, Tibetan Plateau. *Geochemistry, Geophysics, Geosystems*, **10**(2).

Glen, R. A. 2005. The Tasmanides of eastern Australia. *Geological Society, London, Special Publications*, **246**(1), 23–96.

Gouedard, Pierre, Yao, Huajian, Ernst, Fabian, & van der Hilst, Robert D. 2012. Surface wave eikonal tomography in heterogeneous media using exploration data. *Geophysical Journal International*, **191**(2), 781–788.

Graeber, Frank M., Houseman, Gregory A., & Greenhalgh, Stewart A. 2002. Regional teleseismic tomography of the western Lachlan Orogen and the Newer Volcanic Province, southeast Australia. *Geophysical Journal International*, **149**(2), 249–266.

Gray, David R., & Foster, David A. 1998. Character and kinematics of faults within the turbidite-dominated Lachlan Orogen: implications for tectonic evolution of eastern Australia. *Journal of Structural Geology*, **20**(12), 1691–1720.

Griffin, W. L., Wass, S. Y., & Hollis, J. D. 1984. Ultramafic Xenoliths from Bullenmerri and Gnotuk Maars, Victoria, Australia: Petrology of a Sub-Continental Crust-Mantle Transition. *Journal of Petrology*, **25**(1), 53–87.

Gudmundsson, Agust. 2011. Deflection of dykes into sills at discontinuities and magma-chamber formation. *Tectonophysics*, **500**, 50–64.

Gung, Y., Panning, M., & Romanowicz, B. 2003. Global anisotropy and the thickness of continents. *Nature*, **422**(6933), 707–711.

Guo, Zhen, Chen, Y. John, Ning, Jieyuan, Feng, Yongge, Grand, Stephen P., Niu, Fenglin, Kawakatsu, Hitoshi, Tanaka, Satoru, Obayashi, Masayuki, & Ni, James. 2015. High resolution 3-D crustal structure beneath NE China from joint inversion of ambient noise and receiver functions using NECESSArray data. *Earth and Planetary Science Letters*, **416**(0), 1–11.

Guo, Zhen, Chen, Y. John, Ning, Jieyuan, Yang, Yingjie, Afonso, Juan Carlos, & Tang, Youcai. 2016. Seismic evidence of on-going sublithosphere upper mantle convection for intra-plate volcanism in Northeast China. *Earth and Planetary Science Letters*, **433**, 31–43.

Guo, Zhi, Gao, Xing, Yao, Huajian, Li, Juan, & Wang, Weimin. 2009. Midcrustal low-velocity layer beneath the central Himalaya and southern Tibet revealed by ambient noise array tomography. *Geochemistry, Geophysics, Geosystems*, **10**(5), Q05007.

Hacker, B. R. 2000. Hot and Dry Deep Crustal Xenoliths from Tibet. *Science*, **287**(5462), 2463–2466.

Hacker, B. R., Ritzwoller, M. H., & Xie, J. 2014. Partially melted, mica-bearing crust in Central Tibet. *Tectonics*, **33**(7), 2014TC003545.

Handler, Monica R., Bennett, Victoria C., & Esat, Tezer M. 1997. The persistence of off-cratonic lithospheric mantle: Os isotopic systematics of variably metasomatised southeast Australian xenoliths. *Earth and Planetary Science Letters*, **151**, 61–75.

Harmon, Nicholas, Gerstoft, Peter, Rychert, Catherine A., Abers, Geoffrey A., Salas de la Cruz, Mariela, & Fischer, Karen M. 2008. Phase velocities from seismic noise using beamforming and cross correlation in Costa Rica and Nicaragua. *Geophysical Research Letters*, **35**(19).

Harmon, Nicholas, Rychert, Catherine, & Gerstoft, Peter. 2010. Distribution of noise sources for seismic interferometry. *Geophysical Journal International*, **183**(3), 1470–1484.

Hrouda, Frantisek, Pros, Zdenek, & Wohlgemuth, Jiri. 1993. Development of magnetic and elastic anisotropies in slates during progressive deformation. *Physics of the Earth and Planetary Interiors*, **77**(3), 251–265.

Hu, J. M., Chen, H., Qu, H. J., Wu, G. L., Yang, J. X., & Zhang, Z. Y. 2012. Mesozoic deformations of the Dabashan in the southern Qinling orogen, central China. *Journal of Asian Earth Sciences*, **47**, 171–184.

Huang, Hui, Yao, Huajian, & van der Hilst, Robert D. 2010. Radial anisotropy in the crust of SE Tibet and SW China from ambient noise interferometry. *Geophysical Research Letters*, **37**(21).

Huang, R., Zhu, L. P., & Xu, Y. X. 2014. Crustal structure of Hubei Province of China from teleseismic receiver functions: Evidence for lower crust delamination. *Tectonophysics*, **636**, 286–292.

Huang, T. Y., Gung, Y., Kuo, B. Y., Chiao, L. Y., & Chen, Y. N. 2015. Layered deformation in the Taiwan orogen. *Science*, **349**(6249), 720–723.

Huang, Wei-Chuang, Ni, James F., Tilmann, Frederik, Nelson, Doug, Guo, Jingru, Zhao, Wenjin, Mechie, James, Kind, Rainer, Saul, Joachim, Rapine, Richard, & Hearn, Thomas M. 2000. Seismic polarization anisotropy beneath the central Tibetan Plateau. *Journal of Geophysical Research: Solid Earth*, **105**(B12), 27979–27989.

Huang, Zhouchuan, Xu, Mingjie, Wang, Liangshu, Mi, Ning, Yu, Dayong, & Li, Hua. 2008. Shear wave splitting in the southern margin of the Ordos Block, north China. *Geophysical Research Letters*, **35**(19).

Huang, Zhouchuan, Wang, Liangshu, Zhao, Dapeng, Mi, Ning, & Xu, Mingjie. 2011. Seismic anisotropy and mantle dynamics beneath China. *Earth and Planetary Science Letters*, **306**(1), 105–117.

Hubbard, Judith, & Shaw, John H. 2009. Uplift of the Longmen Shan and Tibetan plateau, and the 2008 Wenchuan (M = 7.9) earthquake. *Nature*, **458**(7235), 194–197.

Hung, S.-H., Dahlen, F. A., & Nolet, Guust. 2001. Wavefront healing: a bananaCdoughnut perspective. *Geophysical Journal International*, **146**(2), 289–312.

Hurwitz, Shaul, & Lowenstern, Jacob B. 2014. Dynamics of the Yellowstone hydrothermal system. *Reviews of Geophysics*, **52**(3), 375–411.

Jamieson, R. A., Beaumont, C., Fullsack, P., & Lee, B. 1998. Barrovian regional metamorphism: where's the heat? *Geological Society, London, Special Publications*, **138**(1), 23–51.

Jamieson, Rebecca A, Unsworth, Martyn J, Harris, Nigel BW, Rosenberg, Claudio L, & Schulmann, Karel. 2011. Crustal melting and the flow of mountains. *Elements*, **7**(4), 253–260.

Jaxybulatov, K., Shapiro, N. M., Koulakov, I., Mordret, A., Lands, M., & Sens-Schnfelder, C. 2014. A large magmatic sill complex beneath the Toba caldera. *Science*, **346**(6209), 617–619.

Jiang, C. X., Yang, Y. J., & Zheng, Y. 2014. Penetration of mid-crustal low velocity zone across the Kunlun Fault in the NE Tibetan Plateau revealed by ambient noise tomography. *Earth and Planetary Science Letters*, **406**, 81–92.

Jiang, C. X., Yang, Y. J., & Zheng, Y. 2016. Crustal structure in the junction of Qinling Orogen, Yangtze Craton and Tibetan Plateau: implications for the formation of Dabashan Orocline and the growth of Tibetan Plateau. *Geophysical Journal International*, **205**, 1670–1681.

Jimenez-Munt, Ivone, Fernandez, Manel, Verges, Jaume, & Platt, John P. 2008. Lithosphere structure underneath the Tibetan Plateau inferred from elevation, gravity and geoid anomalies. *Earth and Planetary Science Letters*, **267**(1-2), 276–289.

John, Foden, Marlina, Elburg, Jon, Dougherty-Page, & Andrew, Burtt. 2006. The Timing and Duration of the Delamerian Orogeny: Correlation with the Ross Orogen and Implications for Gondwana Assembly. *The Journal of Geology*, **114**(2), 189–210.

Johnson, R Wally. 1989. *Intraplate volcanism in eastern Australia and New Zealand*. Cambridge University Press.

Kanamori, H., & Anderson, D.L. 1977. Importance of physical dispersion in surface-wave and free-oscillation problems - Review. *Rev. Geophys. Space Phys*, **15**(105-112).

Kao, Honn, Behr, Yannik, Currie, Claire A., Hyndman, Roy, Townend, John, Lin, Fan-Chi, Ritzwoller, Michael H., Shan, Shao-Ju, & He, Jiangheng. 2013. Ambient seismic noise tomography of Canada and adjacent regions: Part I. Crustal structures. *Journal of Geophysical Research: Solid Earth*, **118**(11), 5865–5887.

Karato, Shun-ichiro, Jung, Haemyeong, Katayama, Ikuo, & Skemer, Philip. 2008. Geodynamic Significance of Seismic Anisotropy of the Upper Mantle: New Insights from Laboratory Studies. *Annual Review of Earth and Planetary Sciences*, **36**(1), 59–95.

Karplus, M. S., Klemperer, S. L., Lawrence, J. F., Zhao, W., Mechie, J., Tilmann, F., Sandvol, E., & Ni, J. 2013. Ambient-noise tomography of north Tibet limits geological terrane signature to upper-middle crust. *Geophysical Research Letters*, **40**(5), 808–813.

Kemp, A. I. S., Hawkesworth, C. J., Collins, W. J., Gray, C. M., & Blevin, P. L. 2009. Isotopic evidence for rapid continental growth in an extensional accretionary orogen: The Tasmanides, eastern Australia. *Earth and Planetary Science Letters*, **284**, 455–466.

Kennett, B. L. N., Sambridge, M. S., & Williamson, P. R. 1988. Subspace methods for large inverse problems with multiple parameter classes. *Geophysical Journal International*, **94**(2), 237–247.

Kennett, B. L. N., Engdahl, E. R., & Buland, R. 1995. Constraints on seismic velocities in the Earth from traveltimes. *Geophysical Journal International*, **122**(1), 108–124.

Kennett, B. L. N., Fichtner, A., Fishwick, S., & Yoshizawa, K. 2013. Australian Seismological Reference Model (AuSREM): mantle component. *Geophysical Journal International*, **192**(2), 871–887.

Kennett, B. L. N., Saygin, E., & Salmon, M. 2015. Stacking autocorrelograms to map Moho depth with high spatial resolution in southeastern Australia. *Geophysical Research Letters*, **42**(18), 7490–7497.

Kern, H., & Wenk, H. R. 1990. Fabric-related velocity anisotropy and shear wave splitting in rocks from the Santa Rosa Mylonite Zone, California. *Journal of Geophysical Research: Solid Earth*, **95**(B7), 11213–11223.

Kern, H., Popp, T., Gorbatsevich, F., Zharikov, A., Lobanov, K. V., & Smirnov, Yu P. 2001. Pressure and temperature dependence of VP and VS in rocks from the superdeep well and from surface analogues at Kola and the nature of velocity anisotropy. *Tectonophysics*, **338**(2), 113–134.

Khan, A., Zunino, A., & Deschamps, F. 2011. The thermo-chemical and physical structure beneath the North American continent from Bayesian inversion of surface-wave phase velocities. *Journal of Geophysical Research: Solid Earth*, **116**(B9).

King, Scott D., & Anderson, Don L. 1998. Edge-driven convection. *Earth and Planetary Science Letters*, **160**, 289–296.

Kirby, E., Harkins, N., Wang, E. Q., Shi, X. H., Fan, C., & Burbank, D. 2007. Slip rate gradients along the eastern Kunlun fault. *Tectonics*, **26**(2).

Klemperer, S. L. 2006. Crustal flow in Tibet: geophysical evidence for the physical state of Tibetan lithosphere, and inferred patterns of active flow. *Geological Society, London, Special Publications*, **268**(1), 39–70.

Le Pape, F., Jones, A. G., Vozar, J., & Wei, W. B. 2012. Penetration of crustal melt beyond the Kunlun Fault into northern Tibet. *Nature Geoscience*, **5**(5), 330–335.

Le Pourhiet, Laetitia, Gurnis, Michael, & Saleeby, Jason. 2006. Mantle instability beneath the Sierra Nevada Mountains in California and Death Valley extension. *Earth and Planetary Science Letters*, **251**(1-2), 104–119.

Lei, Jianshe, & Zhao, Dapeng. 2005. P-wave tomography and origin of the Changbai intraplate volcano in Northeast Asia. *Tectonophysics*, **397**, 281–295.

Leon Soto, Gerardo, Sandvol, Eric, Ni, James F., Flesch, Lucy, Hearn, Thomas M., Tilmann, Frederik, Chen, John, & Brown, Larry D. 2012. Significant and vertically coherent seismic anisotropy beneath eastern Tibet. *Journal of Geophysical Research: Solid Earth*, **117**(B5).

Lev, Einat, Long, Maureen D., & van der Hilst, Rob D. 2006. Seismic anisotropy in Eastern Tibet from shear wave splitting reveals changes in lithospheric deformation. *Earth and Planetary Science Letters*, **251**(3-4), 293–304.

Levander, A., Schmandt, B., Miller, M. S., Liu, K., Karlstrom, K. E., Crow, R. S., Lee, C. T. A., & Humphreys, E. D. 2011. Continuing Colorado plateau uplift by delamination-style convective lithospheric downwelling. *Nature*, **472**(7344), 461–465.

Levin, V., & Park, J. 1997. P-SH conversions in a flat-layered medium with anisotropy of arbitrary orientation. *Geophysical Journal International*, **131**(2), 253–266.

Levshin, A. L., & Ritzwoller, M. H. 2001. Automated detection, extraction, and measurement of regional surface waves. *Pure and Applied Geophysics*, **158**(8), 1531–1545.

Levshin, A. L., Barmin, M. P., Ritzwoller, M. H., & Trampert, J. 2005. Minor-arc and major-arc global surface wave diffraction tomography. *Physics of the Earth and Planetary Interiors*, **149**, 205–223.

Li, H. Y., Su, W., Wang, C. Y., & Huang, Z. X. 2009. Ambient noise Rayleigh wave tomography in western Sichuan and eastern Tibet. *Earth and Planetary Science Letters*, **282**(1-4), 201–211.

Li, H. Y., Shen, Y., Huang, Z. X., Li, X. F., Gong, M., Shi, D. A., Sandvol, E., & Li, A. B. 2014. The distribution of the mid-to-lower crustal low-velocity zone beneath the northeastern Tibetan Plateau revealed from ambient noise tomography. *Journal of Geophysical Research: Solid Earth*, **119**(3), 1954–1970.

Li, J. H., Zhang, Y. Q., Dong, S. W., & Shi, W. 2013. Structural and geochronological constraints on the Mesozoic tectonic evolution of the North Dabashan zone, South Qinling, central China. *Journal of Asian Earth Sciences*, **64**, 99–114.

Li, Shuguang, & Sun, Weidong. 1996. A Middle Silurian-Early Devonian Magmatic Arc in the Qinling Mountains of Central China: A Discussion. *The Journal of Geology*, **104**(4), 501–503.

Li, Shuguang, Xiao, Yilin, Liou, Deliang, Chen, Yizhi, Ge, Ningjie, Zhang, Zongqing, Sun, Shen-su, Cong, Bolin, Zhang, Ruyuang, Hart, Stanley R., & Wang, Songshan. 1993. Collision of the North China and Yangtse Blocks and formation of coesite-bearing eclogites: Timing and processes. *Chemical Geology*, **109**, 89–111.

Li, X. H., Li, Z. X., Ge, W. C., Zhou, H. W., Li, W. X., Liu, Y., & Wingate, M. T. D. 2003. Neoproterozoic granitoids in South China: crustal melting above a mantle plume at ca. 825 Ma? *Precambrian Research*, **122**(1-4), 45–83.

Li, Yonghua, Wu, Qingju, Zhang, Fengxue, Feng, Qiangqiang, & Zhang, Ruiqing. 2011. Seismic anisotropy of the Northeastern Tibetan Plateau from shear wave splitting analysis. *Earth and Planetary Science Letters*, **304**(1-2), 147–157.

Li, Z. W., Ni, S., Hao, T. Y., Xu, Y., & Roecker, S. 2012. Uppermost mantle structure of the eastern margin of the Tibetan plateau from interstation Pn traveltime difference tomography. *Earth and Planetary Science Letters*, **335**, 195–205.

Li, Z. X., Li, X. H., Kinny, P. D., & Wang, J. 1999. The breakup of Rodinia: did it start with a mantle plume beneath South China? *Earth and Planetary Science Letters*, **173**.

Liang, Chuntao, & Langston, Charles A. 2008. Ambient seismic noise tomography and structure of eastern North America. *Journal of Geophysical Research: Solid Earth*, **113**(B3), B03309.

Lin, F. C., & Ritzwoller, M. H. 2010. Empirically determined finite frequency sensitivity kernels for surface waves. *Geophysical Journal International*, **182**(2), 923–932.

Lin, F. C., Ritzwoller, M. H., Townend, J., Bannister, S., & Savage, M. K. 2007. Ambient noise Rayleigh wave tomography of New Zealand. *Geophysical Journal International*, **170**(2), 649–666.

Lin, Fan-Chi, & Ritzwoller, Michael H. 2011a. Apparent anisotropy in inhomogeneous isotropic media. *Geophysical Journal International*, **186**(3), 1205–1219.

Lin, Fan-Chi, & Ritzwoller, Michael H. 2011b. Helmholtz surface wave tomography for isotropic and azimuthally anisotropic structure. *Geophysical Journal International*, **186**(3), 1104–1120.

Lin, Fan-Chi, Moschetti, Morgan P., & Ritzwoller, Michael H. 2008. Surface wave tomography of the western United States from ambient seismic noise: Rayleigh and Love wave phase velocity maps. *Geophysical Journal International*, **173**(1), 281–298.

Lin, Fan-Chi, Ritzwoller, Michael H., & Snieder, Roel. 2009. Eikonal tomography: surface wave tomography by phase front tracking across a regional broad-band seismic array. *Geophysical Journal International*, **177**(3), 1091–1110.

Lin, Fan-Chi, Ritzwoller, Michael H., Yang, Yingjie, Moschetti, Morgan P., & Fouch,

Matthew J. 2010. Complex and variable crustal and uppermost mantle seismic anisotropy in the western United States. *Nature Geoscience*, **4**, 55–61.

Lin, Fan-Chi, Li, Dunzhu, Clayton, Robert W., & Hollis, Dan. 2013. High-resolution 3D shallow crustal structure in Long Beach, California: Application of ambient noise tomography on a dense seismic array. *Geophysics*, **78**(4), Q45–Q56.

Lister, Gordon S., & Davis, Gregory A. 1989. The origion of metamorphic core complexs and detachments faults formed during Tertiary continental extension in the northern Colorado River region, U.S.A. *Journal of Structural Geology*, **11**, 65–94.

Liu, M. J., Mooney, W. D., Li, S. L., Okaya, N., & Detweiler, S. 2006. Crustal structure of the northeastern margin of the Tibetan plateau from the Songpan-Ganzi terrane to the Ordos basin. *Tectonophysics*, **420**(1-2), 253–266.

Liu, Qi Yuan, van der Hilst, Robert D, Li, Yu, Yao, Hua Jian, Chen, Jiu Hui, Guo, Biao, Qi, Shao Hua, Wang, Jun, Huang, Hui, & Li, Shun Cheng. 2014. Eastward expansion of the Tibetan plateau by crustal flow and strain partitioning across faults. *Nature Geoscience*, **7**(5), 361–365.

Liu, S. F., Li, W. P., Wang, K., Qian, T., & Jiang, C. X. 2015a. Late Mesozoic development of the southern Qinling-Dabieshan foreland fold-thrust belt, Central China, and its role in continent-continent collision. *Tectonophysics*, **644-645**, 220–234.

Liu, S.F., Qian, T., Li, W. P., Dou, G. X., & Wu, P. 2015b. Oblique closure of the northeastern Paleo-Tethys in central China. *Tectonics*, **34**, 413–434.

Liu, Shaofeng, Steel, Ronald, & Zhang, Guowei. 2005. Mesozoic sedimentary basin development and tectonic implication, northern Yangtze Block, eastern China: record of continentcontinent collision. *Journal of Asian Earth Sciences*, **25**(1), 9–27.

Liu, Zhen, Park, Jeffrey, & Rye, Danny M. 2015c. Crustal anisotropy in northeastern Tibetan Plateau inferred from receiver functions: Rock textures caused by metamorphic fluids and lower crust flow? *Tectonophysics*, **661**, 66–80.

Lobkis, Oleg I., & Weaver, Richard L. 2001. On the emergence of the Green's function in the correlations of a diffuse field. *The Journal of the Acoustical Society of America*, **110**(6), 3011–3017.

Lowenstern, Jacob B., & Hurwitz, Shaul. 2008. Monitoring a Supervolcano in Repose: Heat and Volatile Flux at the Yellowstone Caldera. *Elements*, **4**(1), 35–40.

Lucente, Francesco Pio, Piana Agostinetti, Nicola, Moro, Marco, Selvaggi, Giulio, & Di Bona, Massimo. 2005. Possible fault plane in a seismic gap area of the southern Apennines (Italy) revealed by receiver function analysis. *Journal of Geophysical Research: Solid Earth*, **110**(B4).

Luo, Y. H., Xu, Y. X., & Yang, Y. J. 2012. Crustal structure beneath the Dabie orogenic belt from ambient noise tomography. *Earth and Planetary Science Letters*, **313**, 12–22.

Luo, Yinhe, Yang, Yingjie, Xu, Yixian, Xu, Hongrui, Zhao, Kaifeng, & Wang, Kai. 2015. On the limitations of interstation distances in ambient noise tomography. *Geophysical Journal International*, **201**(2), 652–661.

Ma, X. Y. 1989. Lithospheric Dynamics Map of China and Adjacent Seas (1:4,000,000) and Explanatory Notes. *Geological Publishing House, Beijing, China*.

Ma, Yiran, & Clayton, Robert W. 2015. Flat slab deformation caused by interplate suction force. *Geophysical Research Letters*, **42**(17), 7064–7072.

Mahan, K. 2006. Retrograde mica in deep crustal granulites: Implications for crustal seismic anisotropy. *Geophysical Research Letters*, **33**(24).

Mainprice, Dave. 2007. Seismic anisotropy of the deep Earth from a mineral and rock physics perspective. *Treatise in Geophysics*, **2**, 437–492.

Malcolm, Alison E., & Trampert, Jeannot. 2011. Tomographic errors from wave front healing: more than just a fast bias. *Geophysical Journal International*, **185**(1), 385–402.

Maraschini, Margherita, & Foti, Sebastiano. 2010. A Monte Carlo multimodal inversion of surface waves. *Geophysical Journal International*, **182**(3), 1557–1566.

Marone, Federica, & Romanowicz, Barbara. 2007. The depth distribution of azimuthal anisotropy in the continental upper mantle. *Nature*, **447**(7141), 198–201.

Mather, Ben R., Moresi, L., Cruden, Sandy, & Taylor, David. 2015. 3D numerial modelling of heat flow across heterogeneous geology in South-East Australia. *Proceedings World Geothermal Congress*.

McBride, Jannene S., Lambert, David D., Greig, Alan, & Nicholls, Ian A. 1996. Multistage evolution of Australian subcontinental mantle: Re-Os isotopic constraints from Victorian mantle xenoliths. *Geology*, **24**(7), 631–634.

McDonough, W. F., McCulloch, M. T., & Sun, S. S. 1985. Isotopic and geochemical systematics in Tertiary-Recent basalts from southeastern Australia and implications for the evolution of the sub-continental lithosphere. *Geochimica et Cosmochimica Acta*, **49**(10), 2051–2067.

McDougall, Ian, Allsopp, H. L., & Chamalaun, F. H. 1966. Isotopic dating of the newer volcanics of Victoria, Australia, and geomagnetic polarity epochs. *Journal of Geophysical Research*, **71**(24), 6107–6118.

McNamara, Daniel E., Owens, Thomas J., Silver, Paul G., & Wu, Frances T. 1994. Shear wave anisotropy beneath the Tibetan Plateau. *Journal of Geophysical Research: Solid Earth*, **99**(B7), 13655–13665.

Mechie, J., Sobolev, S. V., Ratschbacher, L., Babeyko, A. Y., Bock, G., Jones, A. G., Nelson, K. D., Solon, K. D., Brown, L. D., & Zhao, W. 2004. Precise temperature estimation in the Tibetan crust from seismic detection of the α-β quartz transition. *Geology*, **32**(7), 601–604.

Meltzer, Anne, & Christensen, Nikolas. 2001. Nanga Parbat crustal anisotropy: Implications for interpretation of crustal velocity structure and shear-wave splitting. *Geophysical Research Letters*, **28**(10), 2129–2132.

Meng, Q. R., & Zhang, G. W. 1999. Timing of collision of the North and South China blocks: Controversy and reconciliation. *Geology*, **27**(2), 123–126.

Meng, Q. R., & Zhang, G. W. 2000. Geologic framework and tectonic evolution of the Qinling orogen, central China. *Tectonophysics*, **323**(3-4), 183–196.

Meng, Qing-Ren, Wang, Erchie, & Hu, Jian-Min. 2005. Mesozoic sedimentary evolution of the northwest Sichuan basin: Implication for continued clockwise rotation of the South China block. *Geological Society of America Bulletin*, **117**(3), 396–410.

Miller, J. McL, Phillips, D., Wilson, C. J. L., & Dugdale, L. J. 2005. Evolution of a reworked orogenic zone: The boundary between the delamerian and lachlan fold belts, southeastern Australia. *Australian Journal of Earth Sciences*, **52**(6), 921–940.

Miller, John McL, Norvick, Martin S., & Wilson, Christopher J. L. 2002. Basement controls on rifting and the associated formation of ocean transform faults-Cretaceous continental extension of the southern margin of Australia. *Tectonophysics*, **359**(1-2), 131–155.

Moorkamp, M., Jones, A. G., & Fishwick, S. 2010. Joint inversion of receiver functions, surface wave dispersion, and magnetotelluric data. *Journal of Geophysical Research: Solid Earth*, **115**(B4).

Moresi, L., Betts, P. G., Miller, M. S., & Cayley, R. A. 2014. Dynamics of continental accretion. *Nature*, **508**(7495), 245–248.

Moschetti, M. P., Ritzwoller, M. H., Lin, F., & Yang, Y. 2010. Seismic evidence for widespread western-US deep-crustal deformation caused by extension. *Nature*, **464**(7290), 885–889.

Mosegaard, K., & Sambridge, M. 2002. Monte Carlo analysis of inverse problems. *Inverse Problems*, **18**(3), R29.

Mosegaard, K., & Tarantola, A. 1995. Monte Carlo sampling of solutions to inverse problems. *Journal of Geophysical Research*, **100**(B7), 12431–12447.

Nicholson, T., Bostock, M., & Cassidy, J. F. 2005. New constraints on subduction zone structure in northern Cascadia. *Geophysical Journal International*, **161**(3), 849–859.

Nicolas, Adolphe, & Christensen, Nikolas I. 1987. Formation of Anisotropy in Upper Mantle Peridotites - A Review. *Composition, Structure and Dynamics of the Lithosphere-Asthenosphere System. American Geophysical Union*, 111–123.

Nie, Shangyou, Yin, An, Rowley, David B., & Jin, Yugan. 1994. Exhumation of the Dabie Shan ultra-high-pressure rocks and accumulation of the Songpan-Ganzi flysch sequence, central China. *Geology*, **22**(11), 999–1002.

Nishida, K., Kawakatsu, H., & Obara, K. 2008. Three-dimensional crustal S wave velocity structure in Japan using microseismic data recorded by Hi-net tiltmeters. *Journal of Geophysical Research: Solid Earth*, **113**(B10), B10302.

Nolet, Guust, & Dahlen, F. A. 2000. Wave front healing and the evolution of seismic delay times. *Journal of Geophysical Research: Solid Earth*, **105**(B8), 19043–19054.

Okaya, David A., & Christensen, Nikolas I. 2002. Anisotropic effects of non-axial seismic wave propagation in foliated crustal rocks. *Geophysical Research Letters*, **29**(11), 2–1–2–4.

O'Reilly, Suzanne Y., & Griffin, W. L. 1984. Sr isotopic heterogeneity in primitive basaltic rocks, southeastern Australia: correlation with mantle metasomatism. *Contributions to Mineralogy and Petrology*, **87**(3), 220–230.

O'Reilly, Suzanne Y., & Griffin, W. L. 2010. Rates of Magma Ascent: Constraints from Mantle-Derived Xenoliths. *Timescales of Magmatic Processes. John Wiley and Sons, Ltd*, 116–124.

O'Relly, Suzanne, & Griffin, W. L. 1985. A xenolith-derived geotherm for southeastern australia and its geophysical implications. *Tectonophysics*, **111**(1-2), 41–63.

Owens, Thomas J, & Zandt, George. 1997. Implications of crustal property variations for models of Tibetan plateau evolution. *Nature*, **387**(6628), 37–43.

Ozacar, A. Arda, & Zandt, George. 2004. Crustal seismic anisotropy in central Tibet: Implications for deformational style and flow in the crust. *Geophysical Research Letters*, **31**(23).

Pan, S. Z., & Niu, F. L. 2011. Large contrasts in crustal structure and composition between the Ordos plateau and the NE Tibetan plateau from receiver function analysis. *Earth and Planetary Science Letters*, **303**(3-4), 291–298.

Pandey, Shantanu, Yuan, Xiaohui, Debayle, Eric, Tilmann, Frederik, Priestley, Keith, & Li, Xueqing. 2015. Depth-variant azimuthal anisotropy in Tibet revealed by surface wave tomography. *Geophysical Research Letters*, **42**(11), 4326–4334.

Pawlak, Agnieszka, Eaton, David W., Darbyshire, Fiona, Lebedev, Sergei, & Bastow, Ian D. 2012. Crustal anisotropy beneath Hudson Bay from ambient noise tomography: Evidence for post-orogenic lower-crustal flow? *Journal of Geophysical Research*, **117**(B8).

Phillips, G., Miller, J. McL, & Wilson, C. J. L. 2002. Structural and metamorphic evolution of the Moornambool Metamorphic Complex, western Lachlan Fold Belt, southeastern Australia. *Australian Journal of Earth Sciences*, **49**(5), 891–913.

Pilia, S., Rawlinson, N., Cayley, R. A., Bodin, T., Musgrave, R., Reading, A. M., Direen, N. G., & Young, M. K. 2015a. Evidence of micro-continent entrainment during crustal accretion. *Scitific Report*, **5**.

Pilia, S, Rawlinson, N, Direen, NG, Reading, AM, Cayley, R, Pryer, L, Arroucau, P, & Duffett, M. 2015b. Linking mainland Australia and Tasmania using ambient seismic noise tomography: Implications for the tectonic evolution of the east Gondwana margin. *Gondwana Research*, **28**(3), 1212–1227.

Ping, X. Q., Zheng, J. P., Zhao, J. H., Tang, H. Y., & Griffin, W. L. 2013. Heterogeneous sources of the Triassic granitoid plutons in the southern Qinling orogen: An E-W tectonic division in central China. *Tectonics*, **32**(3), 396–416.

Price, R. C., Gray, C. M., & Frey, F. A. 1997. Strontium isotopic and trace element heterogeneity in the plains basalts of the Newer Volcanic Province, Victoria, Australia. *Geochimica et Cosmochimica Acta*, **61**(1), 171–192.

Purss, M. B. J., & Cull, J. 2001. Heat-flow data in western Victoria. *Australian Journal of Earth Sciences*, **48**(1), 1–4.

Qin, Jiangfeng, Lai, Shaocong, Grapes, Rodney, Diwu, Chunrong, Ju, Yinjuan, & Li, Yongfei. 2009. Geochemical evidence for origin of magma mixing for the Triassic monzonitic granite and its enclaves at Mishuling in the Qinling orogen (central China). *Lithos*, **112**(3-4), 259–276.

Qiu, Yumin M., Gao, Shan, McNaughton, Neal J., Groves, David I., & Ling, Wenli. 2000. First evidence of > 3.2 Ga continental crust in the Yangtze craton of south China and its implications for Archean crustal evolution and Phanerozoic tectonics. *Geology*, **28**(1), 11–14.

Ramsay, J. G. 1980. Shear zone geometry: A review. *Journal of Structural Geology*, **2**(1-2), 83–99.

Rawlinson, N., & Fishwick, S. 2012. Seismic structure of the southeast Australian lithosphere from surface and body wave tomography. *Tectonophysics*, **572-573**, 111–122.

Rawlinson, N., & Kennett, B. L. N. 2008. Teleseismic tomography of the upper mantle beneath the southern Lachlan Orogen, Australia. *Physics of the Earth and Planetary Interiors*, **167**, 84–97.

Rawlinson, N., & Sambridge, M. 2003. Seismic travel time tomography of the crust and lithosphere. *Advances in Geophysics*, **46**, 81–198.

Rawlinson, N., & Sambridge, M. 2004. Wave front evolution in strongly heterogeneous layered media using the fast marching method. *Geophysical Journal International*, **156**(3), 631–647.

Rawlinson, N., Kennett, B. L. N., & Heintz, M. 2006a. Insights into the structure of the upper mantle beneath the Murray basin from 3D teleseismic tomography. *Australian Journal of Earth Sciences*, **53**(4), 595–604.

Rawlinson, N., Reading, A. M., & Kennett, B. L. N. 2006b. Lithospheric structure of Tasmania from a novel form of teleseismic tomography. *Journal of Geophysical Research: Solid Earth*, **111**(B2), B02301.

Rawlinson, N., Arroucau, P., Musgrave, R., Cayley, R., Young, M., & Salmon, M. 2014a. Complex continental growth along the proto-Pacific margin of East Gondwana. *Geology*, **42**(9), 783–786.

Rawlinson, N., Salmon, M., & Kennett, B. L. N. 2014b. Transportable seismic array tomography in southeast Australia: Illuminating the transition from Proterozoic to Phanerozoic lithosphere. *Lithos*, **189**, 65–76.

Rawlinson, N., Pilia, S., Young, M., Salmon, M., & Yang, Y. 2015. Crust and upper mantle structure beneath southeast Australia from ambient noise and teleseismic tomography. *Tectonophysics*, **in press**.

Ren, Yong, Grecu, Bogdan, Stuart, Graham, Houseman, Gregory, Hegedus, Endre, & Group, South Carpathian Project Working. 2013. Crustal structure of the Carpathian-Pannonian region from ambient noise tomography. *Geophysical Journal International*.

Richardson, N. J., Densmore, A. L., Seward, D., Fowler, A., Wipf, M., Ellis, M. A., Yong, Li, & Zhang, Y. 2008. Extraordinary denudation in the Sichuan Basin: Insights from low-temperature thermochronology adjacent to the eastern margin of the Tibetan Plateau. *Journal of Geophysical Research: Solid Earth*, **113**(B4), B04409.

Ritzwoller, M. H., & Levshin, A. L. 1998. Eurasian surface wave tomography: Group velocities. *Journal of geophysical research*, **103**.

Ritzwoller, M. H., Lin, F. C., & Shen, W. S. 2011. Ambient noise tomography with a large seismic array. *Comptes Rendus Geoscience*, **343**, 558–570.

Ritzwoller, Michael H. 2008. Ambient noise seismic imaging. *McGraw Hill 2008 Yearbook of Science and Technology*.

Ritzwoller, Michael H., Shapiro, Nikolai M., Barmin, Mikhail P., & Levshin, Anatoli L. 2002. Global surface wave diffraction tomography. *Journal of Geophysical Research: Solid Earth*, **107**(B12), ESE 4–1–ESE 4–13.

Robertson, Kate, Taylor, David, Thiel, Stephan, & Heinson, Graham. 2015. Magnetotelluric evidence for serpentinisation in a Cambrian subduction zone beneath the Delamerian Orogen, southeast Australia. *Gondwana Research*, **28**(2), 601–611.

Roux, Philippe, Sabra, Karim G., Kuperman, W. A., & Roux, Andre. 2005. Ambient noise cross correlation in free space: Theoretical approach. *The Journal of the Acoustical Society of America*, **117**(1), 79–84.

Royden, L. H., Burchfiel, B. C., King, R. W., Wang, E., Chen, Z., Shen, F., & Liu, Y. 1997. Surface Deformation and Lower Crustal Flow in Eastern Tibet. *Science*, **276**(5313), 788–790.

Royden, L. H., Burchfiel, B. C., & van der Hilst, R. D. 2008. The geological evolution of the Tibetan Plateau. *Science*, **321**(5892), 1054–1058.

Sabra, Karim G., Roux, Philippe, & Kuperman, W. A. 2005a. Emergence rate of the time-domain Green's function from the ambient noise cross-correlation function. *The Journal of the Acoustical Society of America*, **118**(6), 3524–3531.

Sabra, Karim G., Gerstoft, Peter, Roux, Philippe, Kuperman, W. A., & Fehler, Michael C. 2005b. Surface wave tomography from microseisms in Southern California. *Geophysical Research Letters*, **32**(14), L14311.

Salmon, M., Kennett, B. L. N., & Saygin, E. 2013a. Australian Seismological Reference Model (AuSREM): crustal component. *Geophysical Journal International*, **192**(1), 190–206.

Salmon, M., Kennett, B. L. N., Stern, T., & Aitken, A. R. A. 2013b. The Moho in Australia and New Zealand. *Tectonophysics*, **609**, 288–298.

Sambridge, Malcolm. 1999. Geophysical inversion with a neighbourhood algorithm I. Searching a parameter space. *Geophysical Journal International*, **138**(2), 479–494.

Sandiford, Mike, Wallace, Malcolm, & Coblentz, David. 2004. Origin of the in situ stress field in south-eastern Australia. *Basin Research*, **16**(3), 325–338.

Sandvol, Eric, Ni, James, Kind, Rainer, & Zhao, Wenjin. 1997. Seismic anisotropy beneath the southern Himalayas-Tibet collision zone. *Journal of Geophysical Research: Solid Earth*, **102**(B8), 17813–17823.

Savage, M. K. 1999. Seismic anisotropy and mantle deformation: What have we learned from shear wave splitting? *Reviews of Geophysics*, **37**(1), 65–106.

Saygin, Erdinc, & Kennett, B. L. N. 2012. Crustal structure of Australia from ambient seismic noise tomography. *Journal of Geophysical Research*, **117**(B1).

Saygin, Erdinc, & Kennett, Brian L. N. 2010. Ambient seismic noise tomography of Australian continent. *Tectophysics*, **481**, 116–125.

Schimmel, M., Stutzmann, E., & Gallart, J. 2011. Using instantaneous phase coherence for signal extraction from ambient noise data at a local to a global scale. *Geophysical Journal International*, **184**(1), 494–506.

Schulte-Pelkum, V., Monsalve, G., Sheehan, A., Pandey, M. R., Sapkota, S., Bilham, R., & Wu, F. 2005. Imaging the Indian subcontinent beneath the Himalaya. *Nature*, **435**(7046), 1222–1225.

Searle, M. P., Elliott, J. R., Phillips, R. J., & Chung, S. L. 2011. Crustal-lithospheric structure and continental extrusion of Tibet. *Journal of the Geological Society*, **168**(3), 633–672.

Sethian, James A., & Popovici, A. Mihai. 1999. 3-D traveltime computation using the fast marching method. *Geophysics*, **64**(2), 516–523.

Shapiro, N. M., & Campillo, M. 2004. Emergence of broadband Rayleigh waves from correlations of the ambient seismic noise. *Geophysical Research Letters*, **31**(7).

Shapiro, N. M., & Ritzwoller, M. H. 2002. Monte-Carlo inversion for a global shear-velocity model of the crust and upper mantle. *Geophysical Journal International*, **151**(1), 88–105.

Shapiro, N. M., Ritzwoller, M. H., Molnar, P., & Levin, V. 2004. Thinning and flow of Tibetan crust constrained by seismic anisotropy. *Science*, **305**(5681), 233–236.

Shapiro, N. M., Campillo, M., Stehly, L., & Ritzwoller, M. H. 2005. High-Resolution Surface-Wave Tomography from Ambient Seismic Noise. *Science*, **307**(5715), 1615–1618.

Shen, Chuanbo, Mei, Lianfu, Peng, Lei, Chen, Youzhi, Yang, Zhao, & Hong, Guangfu. 2012. LA-ICPMS UPb zircon age constraints on the provenance of Cretaceous sediments in the Yichang area of the Jianghan Basin, central China. *Cretaceous Research*, **34**, 172–183.

Shen, W. S. 2014. *Baysian Monte Carlo inversion of multiple data sets to image the crust and uppermost mantle structure beneath the continental United States*. Ph.D. thesis.

Shen, W. S., Ritzwoller, M. H., Schulte-Pelkum, V., & Lin, F. C. 2013. Joint inversion of surface wave dispersion and receiver functions: a Bayesian Monte-Carlo approach. *Geophysical Journal International*, **192**(2), 807–836.

Shervais, John W., Vetter, Scott K., & Hanan, Barry B. 2006. Layered mafic sill complex beneath the eastern Snake River Plain: Evidence from cyclic geochemical variations in basalt. *Geology*, **34**(5), 365–368.

Shi, D. N., Shen, Y., Zhao, W. J., & Li, A. B. 2009. Seismic evidence for a Moho offset and south-directed thrust at the easternmost Qaidam-Kunlun boundary in the Northeast Tibetan plateau. *Earth and Planetary Science Letters*, **288**, 329–334.

Shi, W., Zhang, Y. Q., Dong, S. W., Hu, J. M., Wiesinger, M., Ratschbacher, L., Jonckheere, R., Li, J. H., Tian, M., Chen, H., Wu, G. L., Ma, L. C., & Li, H. L. 2012. Intra-continental Dabashan orocline, southwestern Qinling, Central China. *Journal of Asian Earth Sciences*, **46**, 20–38.

Silver, Paul G. 1996. Seismic anisotropy beneath the continents: probing the depths of geology. *Annual Review of Earth and Planetary Sciences*, **24**(1), 385–432.

Sivia, Devinder S. 1996. *Data analysis: a Bayesian tutorial*. Oxford university press.

Smith, Martin L., & Dahlen, F. A. 1973. The azimuthal dependence of Love and Rayleigh wave propagation in a slightly anisotropic medium. *Journal of Geophysical Research*, **78**(17), 3321–3333.

Snieder, Roel. 2004. Extracting the Green's function from the correlation of coda waves: A derivation based on stationary phase. *Physical Review*, **69**(4), 046610.

Socco, Laura Valentina, & Boiero, Daniele. 2008. Improved Monte Carlo inversion of surface wave data. *Geophysical Prospecting*, **56**(3), 357–371.

Sol, S., Meltzer, A., Burgmann, R., van der Hilst, R.D., King, R., Chen, Z., Koons, P.O., Lev, E., Liu, Y.P., Zeitler, P.K., Zhang, X., Zhang, J., & Zurek, B. 2007. Geodynamics of the southeastern Tibetan Plateau from seismic anisotropy and geodesy. *Geology*, **35**(6), 563–566.

Stehly, L., Fry, B., Campillo, M., Shapiro, N. M., Guilbert, J., Boschi, L., & Giardini, D. 2009. Tomography of the Alpine region from observations of seismic ambient noise. *Geophysical Journal International*, **178**(1), 338–350.

Stockwell, R. G., Mansinha, L., & Lowe, R. P. 1996. Localization of the complex spectrum: the S transform. *Signal Processing, IEEE Transactions on*, **44**(4), 998–1001.

Sun, Weidong, Li, Shuguang, Chen, Yadong, & Li, Yujing. 2002. Timing of Synorogenic Granitoids in the South Qinling, Central China: Constraints on the Evolution of the Qinling-Dabie Orogenic Belt. *The Journal of Geology*, **110**(4), 457–468.

Takei, Yasuko. 2000. Acoustic properties of partially molten media studied on a simple binary system with a controllable dihedral angle. *Journal of Geophysical Research: Solid Earth*, **105**(B7), 16665–16682.

Tang, Y. C., Chen, Y. J., Zhou, S. Y., Ning, J. Y., & Ding, Z. F. 2013. Lithosphere structure and thickness beneath the North China Craton from joint inversion of ambient noise and surface wave tomography. *Journal of Geophysical Research-Solid Earth*, **118**(5), 2333–2346.

Tang, Y. C., Obayashi, M., Niu, F. L., Grand, S. P., Chen, Y. J., Kawakatsu, H., Tanaka, S., Ning, J. Y., & Ni, J. F. 2014. Changbaishan volcanism in northeast China linked to subduction-induced mantle upwelling. *Nature Geoscience*, **7**(6), 470–475.

Tapponnier, P., Xu, Z. Q., Roger, F., Meyer, B., Arnaud, N., Wittlinger, G., & Yang, J. S. 2001. Oblique stepwise rise and growth of the Tibet plateau. *Science*, **294**(5547), 1671–1677.

Tarantola, Albert. 2004. *Inverse Problem Theory and Methods for Model Parameter Estimation*. Society for Industrial and Applied Mathematics.

Tarkov, A. P., & Vavakin, V. V. 1982. Poisson's ratio behaviour in various crystalline rocks: application to the study of the Earth's interior. *Physics of the Earth and Planetary Interiors*, **29**(1), 24–29.

Tatham, D.J., Lloyd, G. E., Butler, R.W.H., & M., Casey. 2008. Amphibole and lower crustal seismic properties. *Earth and Planetary Science Letters*, **267**, 118–128.

Taylor, David H., & Cayley, Ross A. 2000. Character and kinematics of faults within the turbidite-dominated Lachlan Orogen: implications for tectonic evolution of eastern Australia: Discussion. *Journal of Structural Geology*, **22**(4), 523–528.

Tian, Y. T., Kohn, B. P., Zhu, C. Q., Xu, M., Hu, S. B., & Gleadow, A. J. W. 2012. Post-orogenic evolution of the Mesozoic Micang Shan Foreland Basin system, central China. *Basin Research*, **24**(1), 70–90.

Tokam, Alain-Pierre K., Tabod, Charles T., Nyblade, Andrew A., Julia, Jordi, Wiens, Douglas A., & Pasyanos, Michael E. 2010. Structure of the crust beneath Cameroon, West Africa, from the joint inversion of Rayleigh wave group velocities and receiver functions. *Geophysical Journal International*, **183**(2), 1061–1076.

Traer, James, & Gerstoft, Peter. 2014. A unified theory of microseisms and hum. *Journal of Geophysical Research: Solid Earth*, **119**(4), 3317–3339.

Traer, James, Gerstoft, Peter, Bromirski, Peter D., & Shearer, Peter M. 2012. Microseisms and hum from ocean surface gravity waves. *Journal of Geophysical Research: Solid Earth*, **117**(B11).

Turner, S. P., Kelley, S. P., VandenBerg, A. H. M., Foden, J. D., Sandiford, M., & Flottmann, T. 1996. Source of the Lachlan fold belt flysch linked to convective removal of the lithospheric mantle and rapid exhumation of the Delamerian-Ross fold belt. *Geology*, **24**(10), 941–944.

Turner, Simon, Hawkesworth, Chris, Liu, Jiaqi, Rogers, Nick, Kelley, Simon, & van Calsteren, Peter. 1993. Timing of Tibetan uplift constrained by analysis of volcanic rocks. *Nature*, **364**(6432), 50–54.

Uenzelmann-Neben, Gabriele, Schmidt, Daniela N., Niessen, Frank, & Stein, Rudiger. 2012. Intraplate volcanism off South Greenland: caused by glacial rebound? *Geophysical Journal International*, **190**(1), 1–7.

Unsworth, M., Wei, W. B., Jones, A. G., Li, S. H., Bedrosian, P., Booker, J., Sheng, J., Deng, M., & Tan, H. D. 2004. Crustal and upper mantle structure of northern Tibet imaged with magnetotelluric data. *Journal of Geophysical Research-Solid Earth*, **109**(B2).

Van Otterloo, J., Raveggi, M., Cas, R. A. F., & Maas, R. 2014. Polymagmatic Activity at the Monogenetic Mt Gambier Volcanic Complex in the Newer Volcanics Province, SE Australia: New Insights into the Occurrence of Intraplate Volcanic Activity in Australia. *Journal of Petrology*, **55**(7), 1317–1351.

VandenBerg, A.H.M., Willman, C.E., Maher, S., Simons, B.A., Cayley, R.A., Taylor, D.H., Morand, V.J., Moore, D.H., & Radojkovic, A. 2000. *The Tasman Fold Belt system in Victoria: geology and mineralisation of Proterozoic to Carboniferous rocks.* Geological Survey of Victoria Special Publication.

Vergne, J., Wittlinger, G., Hui, Q. A., Tapponnier, P., Poupinet, G., Mei, J., Herquel, G., & Paul, A. 2002. Seismic evidence for stepwise thickening of the crust across the NE Tibetan plateau. *Earth and Planetary Science Letters*, **203**(1), 25–33.

Vergne, J., Wittlinger, G., Farra, V., & Su, H. P. 2003. Evidence for upper crustal anisotropy in the Songpan-Ganze (northeastern Tibet) terrane. *Geophysical Research Letters*, **30**.

Villasenor, Antonio, Yang, Yingjie, Ritzwoller, Michael H., & Gallart, Josep. 2007. Ambient noise surface wave tomography of the Iberian Peninsula: Implications for shallow seismic structure. *Geophysical Research Letters*, **34**(11).

Vinnik, Lev P., Reigber, Christoph, Aleshin, Igor M., Kosarev, Grigoriy L., Kaban, Mikhail K., Oreshin, Sergey I., & Roecker, Steven W. 2004. Receiver function tomography of the central Tien Shan. *Earth and Planetary Science Letters*, **225**(1), 131–146.

Vogel, Derek C., & Keays, Reid R. 1997. The petrogenesis and platinum-group element geochemistry of the Newer Volcanic Province, Victoria, Australia. *Chemical Geology*, **136**(34), 181–204.

Wang, C. S., Gao, R., Yin, A., Wang, H. Y., Zhang, Y. X., Guo, T. L., Li, Q. S., & Li, Y. L. 2011. A mid-crustal strain-transfer model for continental deformation: A new perspective from high-resolution deep seismic-reflection profiling across NE Tibet. *Earth and Planetary Science Letters*, **306**(3-4), 279–288.

Wang, Chun-Yong, Flesch, Lucy M., Silver, Paul G., Chang, Li-Jun, & Chan, Winston W. 2008. Evidence for mechanically coupled lithosphere in central Asia and resulting implications. *Geology*, **36**(5), 363–366.

Wang, Chun-Yong, Zhu, Lupei, Lou, Hai, Huang, Bor-Shouh, Yao, Zhixiang, & Luo, Xinghua. 2010. Crustal thicknesses and Poisson's ratios in the eastern Tibetan Plateau and their tectonic implications. *Journal of Geophysical Research: Solid Earth*, **115**(B11), B11301.

Wang, Erchie, Meng, Qingren, Clark Burchfiel, B., & Zhang, Guowei. 2003. Mesozoic large-scale lateral extrusion, rotation, and uplift of the TongbaiDabie Shan belt in east China. *Geology*, **31**(4), 307.

Wang, Q., Chung, S. L., Li, X. H., Wyman, D., Li, Z. X., Sun, W. D., Qiu, H. N., Liu, Y. S., & Zhu, Y. T. 2012. Crustal Melting and Flow beneath Northern Tibet: Evidence from Mid-Miocene to Quaternary Strongly Peraluminous Rhyolites in the Southern Kunlun Range. *Journal of Petrology*, **53**(12), 2523–2566.

Wang, Qiong, Niu, Fenglin, Gao, Yuan, & Chen, Yuntai. 2016. Crustal structure and deformation beneath the NE margin of the Tibetan plateau constrained by teleseismic receiver function data. *Geophysical Journal International*, **204**(1), 167–179.

Ward, Kevin M. 2015. Ambient noise tomography across the southern Alaskan Cordillera. *Geophysical Research Letters*, **42**(9), 3218–3227.

Ward, Kevin M., Porter, Ryan C., Zandt, George, Beck, Susan L., Wagner, Lara S., Minaya, Estela, & Tavera, Hernando. 2013. Ambient noise tomography across the Central Andes. *Geophysical Journal International*, ggt166.

Watanabe, Tohru. 1993. Effects of water and melt on seismic velocities and their application to characterization of seismic reflectors. *Geophysical Research Letters*, **20**(24), 2933–2936.

Weaver, Richard L., & Lobkis, Oleg I. 2001. Ultrasonics without a Source: Thermal Fluctuation Correlations at MHz Frequencies. *Physical Review Letters*, **87**(13), 134301.

Wei, Wenbo, Unsworth, Martyn, Jones, Alan, Booker, John, Tan, Handong, Nelson, Doug, Chen, Leshou, Li, Shenghui, Solon, Kurt, Bedrosian, Paul, Jin, Sheng, Deng, Ming, Ledo, Juanjo, Kay, David, & Roberts, Brian. 2001. Detection of Widespread Fluids in the Tibetan Crust by Magnetotelluric Studies. *Science*, **292**, 716–719.

Wellman, P., & McDougall, Ian. 1974. Cainozoic igneous activity in eastern Austalia. *Tectonophysics*, **23**(1-2), 49–65.

Whelan, J., Hergt, J., & Woodhead, J. 2007. Granite-greenstone connection in western Victoria: an example from the Bushy Creek Igneous Complex. *Australian Journal of Earth Sciences*, **54**(7), 975–990.

Wielandt, E. 1987. On the validity of the ray approximation for interpreting delay times. *Seismic Tomography: With Applications in Global Seismology and Exploration Geophysics. Springer Netherlands*, 85–98.

Wilks, Kenneth R., & Carter, Neville L. 1990. Rheology of some continental lower crustal rocks. *Tectonophysics*, **182**, 57–77.

Wollenberg, H. A., & Smith, A. R. 1987. Radiogenic heat production of crustal rocks: An assessment based on geochemical data. *Geophysical Research Letters*, **14**(3), 295–298.

Wu, Chenglong, Xu, Tao, Badal, Jos, Wu, Zhenbo, & Teng, Jiwen. 2015. Seismic anisotropy across the Kunlun fault and their implications for northward transforming lithospheric deformation in northeastern Tibet. *Tectonophysics*, **659**, 91–101.

Wu, Yuan-Bao, & Zheng, Yong-Fei. 2013. Tectonic evolution of a composite collision orogen: An overview on the Qinling-Tongbai-Hong'an-Dabie-Sulu orogenic belt in central China. *Gondwana Research*, **23**(4), 1402–1428.

Xie, J. Y., Ritzwoller, M. H., Shen, W. S., Yang, Y. J., Zheng, Y., & Zhou, L. Q. 2013. Crustal radial anisotropy across Eastern Tibet and the Western Yangtze Craton. *Journal of Geophysical Research: Solid Earth*, **118**(8), 4226–4252.

Xu, C. H., Zhou, Z. Y., Chang, Y., & Guillot, F. 2010. Genesis of Daba arcuate structural belt related to adjacent basement upheavals: Constraints from Fission-track and (U-Th)/He thermochronology. *Science China-Earth Sciences*, **53**(11), 1634–1646.

Xu, L. L., Rondenay, S., & van der Hilst, R. D. 2007. Structure of the crust beneath the southeastern Tibetan Plateau from teleseismic receiver functions. *Physics of the Earth and Planetary Interiors*, **165**(3-4), 176–193.

Xu, Tao, Wu, Zhenbo, Zhang, Zhongjie, Tian, Xiaobo, Deng, Yangfan, Wu, Chenglong, & Teng, Jiwen. 2014. Crustal structure across the Kunlun fault from passive source seismic profiling in East Tibet. *Tectonophysics*, **627**, 98–107.

Yan, D. P., Zhou, M. F., Li, S. B., & Wei, G. Q. 2011. Structural and geochronological constraints on the Mesozoic-Cenozoic tectonic evolution of the Longmen Shan thrust belt, eastern Tibetan Plateau. *Tectonics*, **30**(6).

Yang, Y. 2014. Application of teleseismic long-period surface waves from ambient noise in regional surface wave tomography: a case study in western USA. *Geophysical Journal International*, **198**(3), 1644–1652.

Yang, Y. J., & Forsyth, D. W. 2006. Regional tomographic inversion of the amplitude and phase of Rayleigh waves with 2-D sensitivity kernels. *Geophysical Journal International*, **166**(3), 1148–1160.

Yang, Y. J., Ritzwoller, M. H., Levshin, A. L., & Shapiro, N. M. 2007. Ambient noise rayleigh wave tomography across Europe. *Geophysical Journal International*, **168**(1), 259–274.

Yang, Y. J., Ritzwoller, M. H., Lin, F. C., Moschetti, M. P., & Shapiro, N. M. 2008. Structure of the crust and uppermost mantle beneath the western United States revealed by ambient noise and earthquake tomography. *Journal of Geophysical Research: Solid Earth*, **113**(B12).

Yang, Y. J., Zheng, Y., Chen, J., Zhou, S. Y., Celyan, S., Sandvol, E., Tilmann, F., Priestley, K., Hearn, T. M., Ni, J. F., Brown, L. D., & Ritzwoller, M. H. 2010. Rayleigh wave phase velocity maps of Tibet and the surrounding regions from ambient seismic noise tomography. *Geochemistry Geophysics Geosystems*, **11**(8).

Yang, Y. J., Ritzwoller, M. H., & Jones, C. H. 2011. Crustal structure determined from ambient noise tomography near the magmatic centers of the Coso region, southeastern California. *Geochemistry, Geophysics, Geosystems*, **12**(2).

Yang, Y. J., Ritzwoller, M. H., Zheng, Y., Shen, W. S., Levshin, A. L., & Xie, Z. J. 2012. A synoptic view of the distribution and connectivity of the mid-crustal low velocity zone beneath Tibet. *Journal of Geophysical Research: Solid Earth*, **117**(B04303).

Yang, Yingjie, & Ritzwoller, Michael H. 2008. Teleseismic surface wave tomography in the western U.S. using the Transportable Array component of USArray. *Geophysical Research Letters*, **35**(4).

Yao, H. J., Beghein, C., & van der Hilst, R. D. 2008. Surface wave array tomography in SE Tibet from ambient seismic noise and two-station analysis II. Crustal and upper-mantle structure. *Geophysical Journal International*, **173**, 205–219.

Yao, H. J., van der Hilst, R. D., & Montagner, J. P. 2010. Heterogeneity and anisotropy of the lithosphere of SE Tibet from surface wave array tomography. *Journal of Geophysical Research: Solid Earth*, **115**(B12307).

Yao, Huajian, Van Der Hilst, Robert D., & De Hoop, Maarten V. 2006. Surface-wave array tomography in SE Tibet from ambient seismic noise and two-station analysis I. Phase velocity maps. *Geophysical Journal International*, **166**(2), 732–744.

Yin, A., & Harrison, T. M. 2000. Geologic evolution of the Himalayan-Tibetan orogen. *Annual Review of Earth and Planetary Sciences*, **28**, 211–280.

Yin, A., Dang, Y. Q., Zhang, M., Chen, X. H., & McRivette, M. W. 2008. Cenozoic tectonic evolution of the Qaidam basin and its surrounding regions (Part 3): Structural geology, sedimentation, and regional tectonic reconstruction. *Geological Society of America Bulletin*, **120**(7-8), 847–876.

Yoshizawa, K., & Kennett, B. L. N. 2002. Non-linear waveform inversion for surface waves with a neighbourhood algorithm application to multimode dispersion measurements. *Geophysical Journal International*, **149**(1), 118–133.

Young, M. K., Rawlinson, N., Arroucau, P., Reading, A. M., & Tkalcic, H. 2011. High-frequency ambient noise tomography of southeast Australia: New constraints on Tasmania's tectonic past. *Geophysical Research Letters*, **38**(13).

Young, M. K., Cayley, R. A., McLean, M. A., Rawlinson, N., Arroucau, P., & Salmon, M. 2013a. Crustal structure of the east Gondwana margin in southeast Australia revealed by transdimensional ambient seismic noise tomography. *Geophysical Research Letters*, **40**(16), 4266–4271.

Young, M. K., Rawlinson, N., & Bodin, T. 2013b. Transdimensional inversion of ambient seismic noise for 3D shear velocity structure of the Tasmanian crust. *Geophysics*, **78**(3), WB49–WB62.

Yu, Yang, Park, Jeffrey, & Wu, Francis. 1995. Mantle anisotropy beneath the Tibetan Plateau: evidence from long-period surface waves. *Physics of the Earth and Planetary Interiors*, **87**(3-4), 231–246.

Yuan, Huaiyu, & Dueker, Ken. 2005. Teleseismic P-wave tomogram of the Yellowstone plume. *Geophysical Research Letters*, **32**(7).

Yuan, Xuecheng. 1996. Velocity structure of the Qinling lithosphere and mushroom cloud model. *Science China Earth Sciences*, **39**(3), 235–244.

Yue, H., Chen, Y. J., Sandvol, E., Ni, J., Hearn, T., Zhou, S. Y., Feng, Y. G., Ge, Z. X., Trujillo, A., Wang, Y. B., Jin, G., Jiang, M. M., Tang, Y. C., Liang, X. F., Wei, S. Q., Wang, H. Y., Fan, W. Y., & Liu, Z. 2012. Lithospheric and upper mantle structure of the northeastern Tibetan Plateau. *Journal of Geophysical Research: Solid Earth*, **117**(B05307).

Zandt, George, & Ammon, Charles J. 1995. Continental crust composition constrained by measurements of crustal Poisson's ratio. *Nature*, **374**(6518), 152–154.

Zhang, B. R., Gao, S., Zhang, H. F., & Han, M. W. 2002. The Geochemistry of the Qinling Orogenic Belt. *Science Press, Beijing*.

Zhang, G.W., Zhang, B.R., Yuan, X.C., & Xiao, Q. 2001. Qinling Orogenic Belt and Continental Dynamics. *Science Press, Beijing*, 1–855.

Zhang, Hongshuang, Teng, Jiwen, Tian, Xiaobo, Zhang, Zhongjie, Gao, Rui, & Liu, Jiaqi. 2012. Lithospheric thickness and upper-mantle deformation beneath the NE Tibetan Plateau inferred from S receiver functions and SKS splitting measurements. *Geophysical Journal International*, **191**(3), 1285–1294.

Zhang, Shuqing, & Karato, Shun-ichiro. 1995. Lattice preferred orientation of olivine aggregates deformed in simple shear. *Nature*, **375**(6534), 774–777.

Zhang, Z. J., Bai, Z. M., Mooney, W., Wang, C. Y., Chen, X. B., Wang, E., Teng, J. W., & Okaya, N. 2009. Crustal structure across the Three Gorges area of the Yangtze platform,

central China, from seismic refraction/wide-angle reflection data. *Tectonophysics*, **475**(3-4), 423–437.

Zhang, Z. J., Yuan, X. H., Chen, Y., Tian, X. B., Kind, R., Li, X. Q., & Teng, J. W. 2010. Seismic signature of the collision between the east Tibetan escape flow and the Sichuan Basin. *Earth and Planetary Science Letters*, **292**(3-4), 254–264.

Zhao, Dapeng, Tian, You, Lei, Jianshe, Liu, Lucy, & Zheng, Sihua. 2009. Seismic image and origin of the Changbai intraplate volcano in East Asia: Role of big mantle wedge above the stagnant Pacific slab. *Physics of the Earth and Planetary Interiors*, **173**(3-4), 197–206.

Zheng, S., Sun, X. L., Song, X. D., Yang, Y. J., & Ritzwoller, M. H. 2008. Surface wave tomography of China from ambient seismic noise correlation. *Geochemistry, Geophysics, Geosystems*, **9**(5), Q05020.

Zheng, Xiu-Fen, Ouyang, Biao, Zhang, Dong-Ning, Yao, Zhi-Xiang, Liang, Jian-Hong, & Zheng, Jie. 2009. Construction of the Technical System of Data Backup Centre for China Seismograph Network and Its Support to Wenchuan Earthquake Researches. *Chinese Journal of Geophysics*, **52**(3), 657–662.

Zheng, Y., Shen, W. S., Zhou, L. Q., Yang, Y. J., Xie, Z. J., & Ritzwoller, M. H. 2011. Crust and uppermost mantle beneath the North China Craton, northeastern China, and the Sea of Japan from ambient noise tomography. *Journal of Geophysical Research: Solid Earth*, **116**(B12).

Zhou, D, & Graham, SA. 1996. The Songpan-Ganzi complex of the West Qinling Shan as a Triassic remnant ocean basin. *World and Regional Geology*, **1**(8), 281–299.

Zhou, L. Q., Xie, J. Y., Shen, W. S., Zheng, Y., Yang, Y. J., Shi, H. X., & Ritzwoller, M. H. 2012. The structure of the crust and uppermost mantle beneath South China from ambient noise and earthquake tomography. *Geophysical Journal International*, **189**(3), 1565–1583.

Zhou, Mei-Fu, Kennedy, Allen K., Sun, Min, Malpas, John, & Lesher, C. Michael. 2002. Neoproterozoic Arc-Related Mafic Intrusions along the Northern Margin of South China: Implications for the Accretion of Rodinia. *The Journal of Geology*, **110**(5), 611–618.

Zhou, Ying, Dahlen, F. A., & Nolet, Guust. 2004. Three-dimensional sensitivity kernels for surface wave observables. *Geophysical Journal International*, **158**(1), 142–168.